Universität Rostock

Traditio et Innovatio

Phase Transitions in Hydrogen-Helium Mixtures

Dissertation zur Erlangung des akademischen Grades
doctor rerum naturalium (Dr. rer. nat.)
der Mathematisch-Naturwissenschaftlichen Fakultät
der Universität Rostock

vorgelegt von
Winfried Lorenzen

Rostock, 13. Dezember 2012

urn:nbn:de:gbv:28-diss2012-0121-8

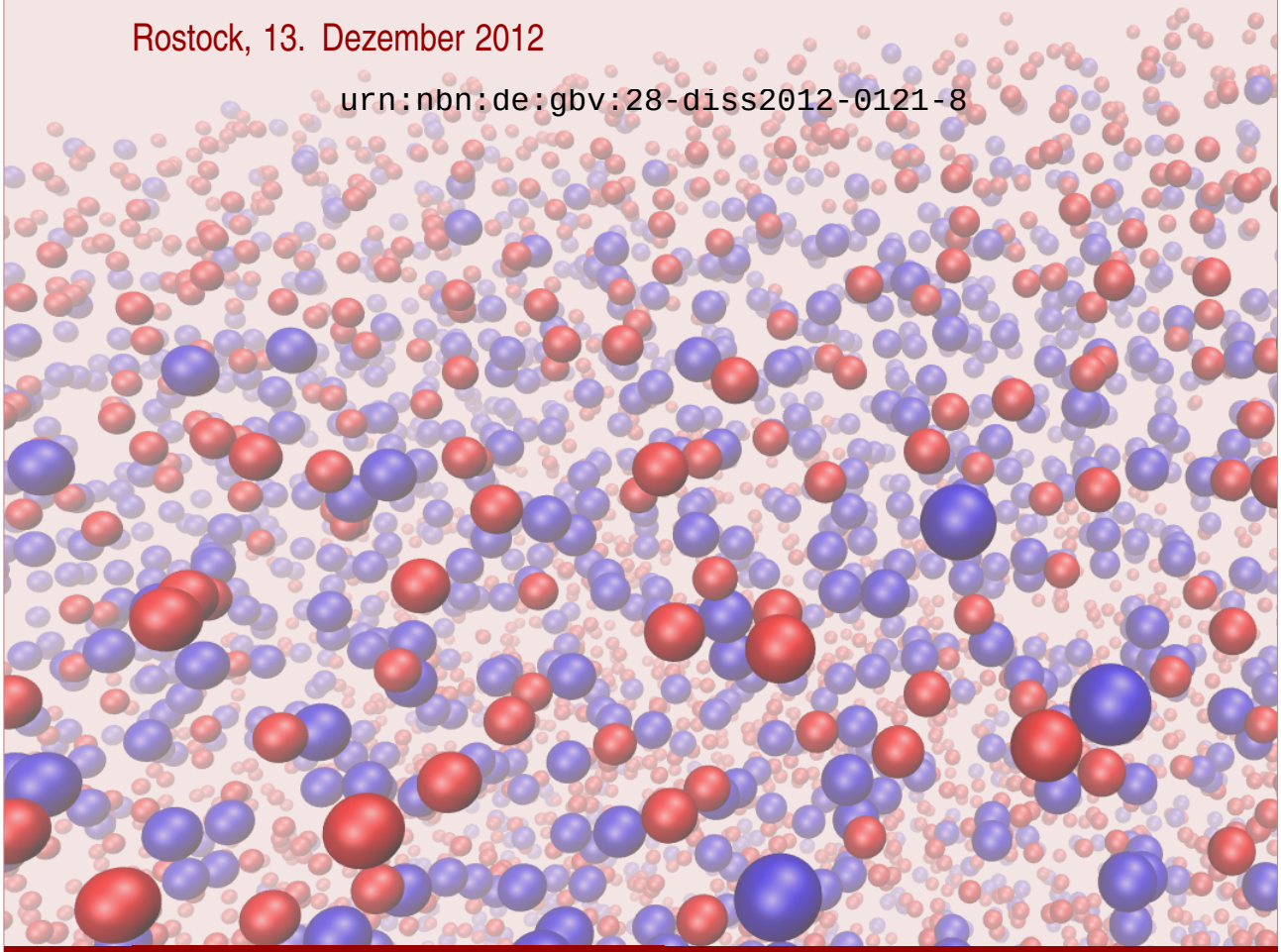

Mathematisch-Naturwissenschaftliche Fakultät

Gutachter:
Prof. Dr. Dr. h.c./RAS Ronald Redmer
Institut für Physik, Universität Rostock
Dr. Michael P. Desjarlais
Sandia National Laboratories, USA

Datum der Einreichung:
28.02.2012
Datum der Verteidigung:
20.06.2012

Adresse:
Universität Rostock
Institut für Physik
18051 Rostock
http://www.physik.uni-rostock.de

Abstract

The properties of hydrogen, helium and their mixtures at high pressures are of great importance for a variety of applications. Although hydrogen and helium are the simplest elements, their study at high pressures poses great difficulties for experiment and theory alike. In this work, results from extensive *ab initio* calculations for these elements are reported. For hydrogen, special attention has been paid to the nonmetal-to-metal-transition and its possible accompanying first-order liquid-liquid phase transition. Conclusive evidence for the occurrence of this transition, which has already been debated for several decades, is shown. Furthermore, an accurate wide range equation of state is calculated for helium, which is of paramount interest for interior structure models of giant planets and brown dwarfs. A high pressure phase diagram of helium is derived from these equation of state calculations. Finally, the miscibility gap of hydrogen and helium is calculated and its implication for the structure and evolution of giant planets like Jupiter and Saturn is discussed.

Zusammenfassung

Die Eigenschaften von Wasserstoff, Helium und ihren Mischungen sind von großem Interesse für eine Vielzahl von Anwendungen. Obwohl Wasserstoff und Helium die einfachsten Elemente sind, ist ihre theoretische und experimentelle Untersuchung unter hohen Drücken sehr schwierig. In dieser Arbeit werden Ergebnisse von aufwendigen *ab initio* Berechnungen gezeigt. Bei reinem Wasserstoff steht speziell der Nichtmetall-Metall-Übergang und der damit verbundene Phasenübergang erster Ordnung im Fokus. Die Ergebnisse zeigen überzeugend die Existenz dieses Phasenüberganges, welcher bereits seit einigen Jahrzehnten diskutiert wurde. Für Helium wird eine präzise Zustandsgleichung berechnet, die in einen großen Dichte- und Temperaturbereich gültig ist, und die für die Modellierung der inneren Struktur von planetaren Gasriesen und Braunen Zwergen von enormer Bedeutung ist. Es wird ein Hochdruckphasendiagramm von Helium konstruiert, welches in Einklang mit experimentellen Daten ist. Schließlich wird als zentrales Thema die Mischungslücke von Wassertoff und Helium unter hohen Drücken berechnet und ihre Auswirkung auf die Struktur und Evolution großer Planeten wie Jupiter und Saturn diskutiert.

Contents

Part I.

Introduction

1. Motivation

The study of materials at high pressures of several megabar and temperatures in the order of 10^4 K is of fundamental interest for a broad range of applications. On the one hand, it is interesting from a basic research point of view, because matter at these extreme conditions exhibits strong correlations, and quantum effects play an important role. On the other hand, the properties of these materials are of huge importance for e.g. planetary physics (see section 1.5), inertial confinement fusion (ICF),[1] and the study of ultra-fast dynamics in matter as induced by energetic laser and particle beams. At the same time, they are difficult to study experimentally and theoretically. While experiments (section 1.3) face the problem to generate these extreme states of matter and at the same time to measure their properties accurately (which is especially true for hydrogen and helium), theories have to deal with states far away from known limits such as ideal laws.

In this work the properties of hydrogen, helium, and their mixture will be examined. They both are of special interest, because they are the most abundant elements in the universe and the solar system[2] and giant objects like gas planets, stars, and brown dwarfs consist mostly of hydrogen and helium. Although they are the simplest elements, they still exhibit various interesting effects, for example a nonmetal-to-metal transition which has huge consequences for their properties (see section 1.4).

1.1. Characterizing plasma states

Although most of the visible matter in the universe is in the plasma state (according to Gurnett and Bhattacharjee[3] more than 99%), the properties of plasmas can be very diverse, due to the wide range of possible densities and temperatures. To characterize a plasma, two parameters have been introduced which differentiate between strongly and weakly coupled plasmas (coupling parameter Γ) and the importance of quantum effects (degeneracy parameter Θ). The Γ parameter is defined as the ratio between the Coulomb energy at the mean particle distance and the thermal energy

$$\Gamma = \frac{E_{\text{coulomb}}}{E_{\text{thermal}}} = \frac{e^2}{4\pi\varepsilon_0 d\, k_{\text{B}} T}, \tag{1.1}$$

where e is the elementary charge, ε_0 the electric constant, d the mean particle distance, k_{B} the Boltzmann constant, and T the temperature. The mean electron distance d can be calculated from the electron density n_e by

$$d = \left(\frac{3}{4\pi n_e}\right)^{1/3}. \tag{1.2}$$

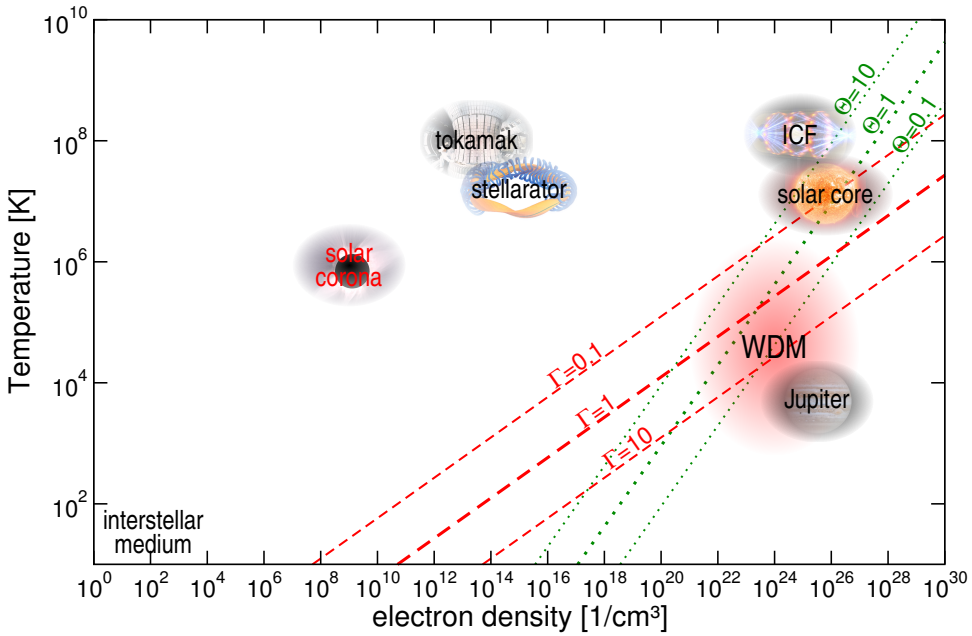

Figure 1.1.: Density-temperature plane of plasmas. Shown are lines of constant Γ (red dashed line) and Θ (green dotted lines) parameters. Images taken from Ref. 4

The degeneracy parameter is defined by the ratio between the thermal energy and the Fermi energy

$$\Theta = \frac{E_{\text{thermal}}}{E_{\text{F}}} = \frac{2 m_e k_{\text{B}} T}{\hbar^2 \left(3\pi^2 n_e\right)^{2/3}}, \tag{1.3}$$

where m_e is the electron mass. To illustrate the occurrence of these states, lines of constant Γ and Θ are shown in the density-temperature plane in figure 1.1, along with typical plasma states.

The region where correlations and quantum effects begin to dominate, i.e. for $\Gamma > 1$ and $\Theta < 1$, is often called warm dense matter (WDM). WDM consists typically of solid state like densities and temperatures in the order of 10^4 K. As can be seen from figure 1.1, this is exactly the region, where the interiors of giant planets are located. Therefore, the correct understanding of the properties of matter under these conditions is of great importance for modeling giant planets.

1.2. Theories

Several theoretical methods have been applied for hydrogen, helium, and their mixture in the past. They can be divided into two different groups, based on the underlying picture of the constituents. In the so-called “chemical picture”, all chemical constituents are treated as individual species, e.g. for a hydrogen plasma H_2 and H_2^+ molecules and molecular ions, H atoms, H^- ions, and electrons are all treated as species on their own, whereas ions and electrons are the only constituents in the “physical picture”.[5] In principle, both pictures should yield the same results if the models derived in these pictures are accurate enough. One main goal of models in the chemical picture is to

determine the composition of the plasma for a given thermodynamic state. However, an accurate description of all interactions between all the different species is needed, together with their density and temperature dependence. Several of these models have been used to study hydrogen, helium, and their mixtures and to construct a equations of state (EOS),[6;7] for example the very often used SCvH (Saumon, Chabrier, and van Horn) model[8] or the fluid variational theory (FVT)[9–13] and FVT$^+$.[14;15]

While these models give in general quite good results in well defined thermodynamic phases like e.g. the molecular fluid of hydrogen or the fully ionized plasma, and are usually exact in limiting cases, they seem to break down at the interesting WDM region,[16] see also section 1.4.2. This is caused by the near impossibility to derive all interactions between the different species and to obtain the plasma composition accurately enough.

In contrast, only electrons and ions are treated as individual species in the "physical picture". This avoids most of the difficulties of chemical pictures, since all interactions are well defined (the Coulomb potential), and the composition of the system stays the same for all calculations. Because it is often difficult to define a bound state in the physical picture, it is not always possible to extract quantities like the degree of ionization or dissociation, but often they are not needed either. In the past decade models in this physical picture have been applied with great success, especially methods based on density functional theory (DFT). While early results relied on static calculations, an important breakthrough was reached by combining DFT for the electrons with a molecular dynamics (MD) simulation for the ions, either in the Car-Parrinello (CP)-MD[17] or the Born-Oppenheimer (BO)-MD. Together with finite temperature (FT)-DFT[18] this method evolved to a versatile and *predicitve* tool for *ab initio*[a] simulations of WDM.[20] With today's computer power MD simulations with reasonable particle numbers and long enough simulation runs are possible. Such FT-DFT-MD-simulations are used throughout this work and are described in more detail in chapter 2.

A further approach are wave packet molecular dynamics simulations (WPMD), which treat the electrons as wave packets, thus accomodating for the quantum nature of the electrons.[21–24] However, since the wave packets will spread over time, their width has to be controlled in the simulations. This introduces an element of uncertainty to the method.

Even more accurate *ab initio* results can be reached by quantum Monte Carlo (QMC) methods like path integral Monte Carlo (PIMC)[25–27] or coupled electron ion Monte Carlo (CEIMC).[28–30] These methods are in general more computationally demanding and are thus not as widely used as FT-DFT-MD at present. This will probably change in the future, and some of the results in this work will be compared to QMC calculations (chapter 4).

1.3. Experiments

Although high pressure experiments in the megabar regime are very difficult to perform, some techniques have been developed to generate these extreme states of matter. The conceptually easiest method are diamond anvil cell (DAC)[31–34] experiments, where high pressures are reached at small diamond surfaces. Since the pressure is inversely proportional to the surface, high pressures can

[a] Note that the definition of *ab initio*, and if DFT is such a method, depends a little bit on the scientific community, mostly due to the (unknown) XC functional, see e.g. Perdew *et al.*[19] for a discussion.

be reached with relatively small forces, if the surface is small enough. These kind of experiments have the advantage that they are static experiments, and, therefore, reliable measurements of thermodynamic data are possible. However, the disadvantage of these experiments is the difficulty to obtain high temperatures. By laser heating it is possible to reach several 1000 K, but due to the high diffusivity of hydrogen and helium at these extreme conditions only about 1000 K were reached for hydrogen[35–37] and helium,[38] which is still "cold" in WDM terms. Still, they are a very good tool to study e.g. high pressure melting lines and crystal structures.

A way to reach high pressures and high temperatures are dynamic shock wave experiments,[39] for example the measurement of the Hugoniot relation for a material. This Hugoniot relation connects all possible thermodynamic states of a shock wave experiment from a given starting point. The advantage is, that this Hugoniot relation is thermodynamically well defined and can be easily calculated from an EOS. This makes comparison between experimental data and theoretical EOS straightforward. Today, many experimental studies for hydrogen have been performed,[40–47] and a plethora of theoretical calulations have been reported.[10;16;25;48–57] One problem of these experiments is, that they have in general rather big errorbars in the compression ratio, which often prevents a discrimination of theoretical models. Another disadvantage is, that, after an initial compression, all energy deposition in the system adds to the temperature of the material. While the highest compression ratio which can be reached is itself an interesting quantity, these Hugoniot experiments cannot reach arbitrary densities. Especially high densities at moderate temperatures are not accessible.

One possible remedy for this problem is the combination of both methods, i.e. starting a Hugoniot experiment from a precompressed initial state.[46;58] Another possiblity is to perform double[59–61] or multi-shock experiments, which can be implemented by using reverberating shock waves.[44;62] In these experiments, a series of Hugoniot compressions is launched, each compression starting from the endpoint of the previous shock. While this makes the evaluation and comparison to theories more involved, it can be shown that the resulting thermodynamic states are located near an isentrope of the system.[63] Therefore, they are called quasi-isentropic compression experiments. With this technique it is possible to reach very high compression, without heating the system too much, thereby reaching the WDM region.

1.4. Phase transitions

There are several possible phase transitions in these fascinating high pressure phases, which are, however, not all necessarily of first order. In the following the possible transitions for hydrogen, helium, and their mixture will be discussed in detail.

1.4.1. Solid structure and melting line

Both hydrogen and helium are expected to be solid at low temperatures in the WDM region, and various structural phase transitions have been proposed for both elements. There is different progress in the accurate determination of their melting lines and their solid phases. Although a very interesting field, the crystal structures are not topic of this work since they are usually not relevant for

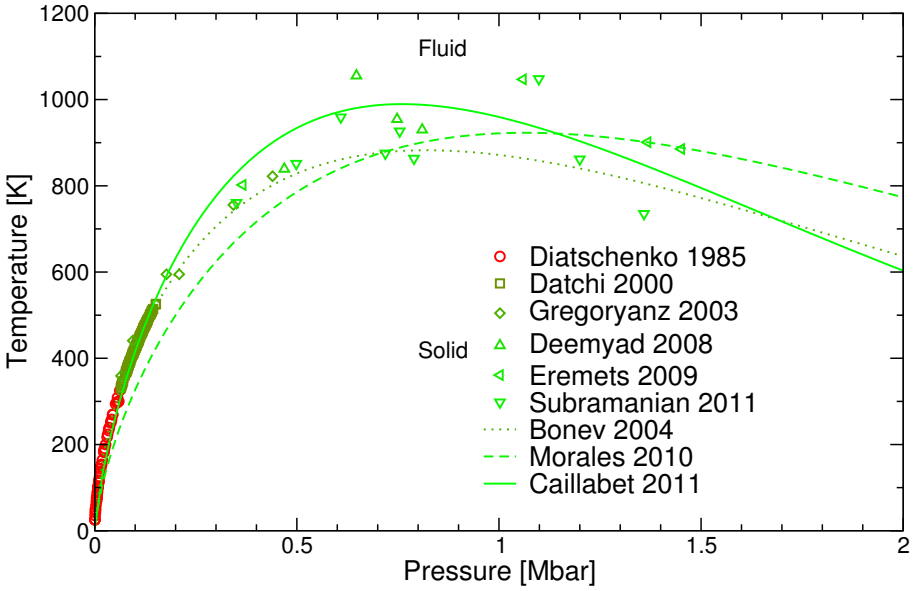

Figure 1.2.: Melting line of hydrogen. Shown are different experimental results[35–37;64–66] (symbols) and theoretical predictions[67–69] (lines), color-coded from red (early) to green (new). The melting line from Bonev *et al.*[67] is a fit to theoretical and experimental data.

astrophysical objects.

Hydrogen

There is a steady progress in the determination of the hydrogen melting line from both experimental[35–37;64–66] and theoretical[67–69] studies, see figure 1.2. Due to the various possible crystal structures of hydrogen at high pressures,[70;71] the calculation of the melting line has to be performed very carefully. Still, the agreement between theories and experiments is very good for pressures below 2 Mbar. The slope of the melting line for higher pressures as predicted by theory has yet to be confirmed by experiments, especially because it is partially based on the extrapolation of Kechin[72] type fits to the data points. This melting line is, however, not topic of this work, because the level of its calculation so far is very good, and it is not relevant for the interior structure of giant planets due to its overall low temperatures of below 1000 K. For an overview of the high pressure structures of hydrogen, see e.g. Refs. 70;71.

Helium

Even though good progress has been made in the experimental determination of the helium melting line,[38;65;73–76] the most recent experiment by Santamaría-Pérez *et al.*[38] achieves “only” 0.8 Mbar. Different structural phase transitions have been determined experimentally,[82;83] for more details see section 7.4. However, the theoretical treatment[77–81] of the high pressure melting line so far ends at

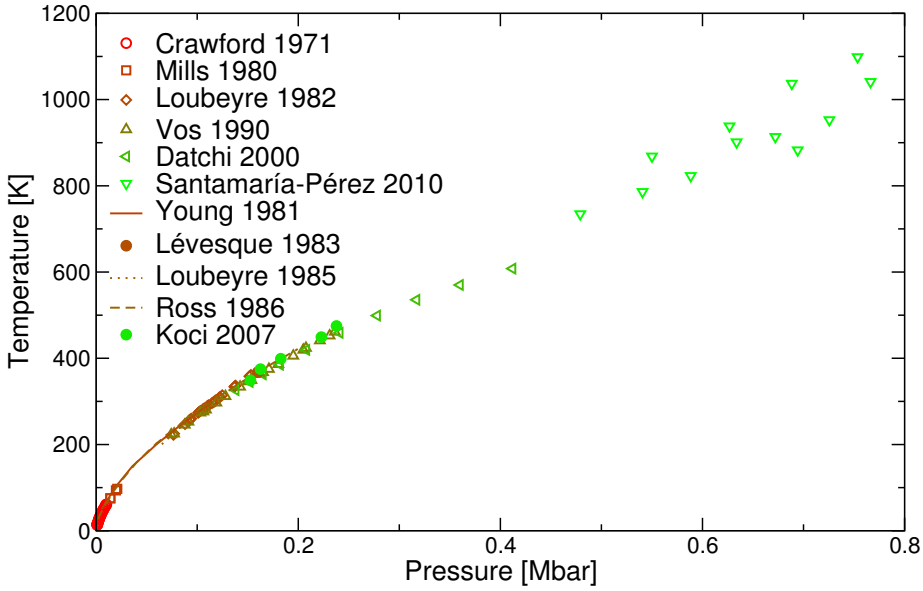

Figure 1.3.: Melting line of helium. Several experimental results[38;65;73–76] are show (open symbols), as well as theoretical predictions[77–81] (lines and filled symbols).

about 0.25 Mbar.[81] All these theoretical results were obtained by classical calculations, employing empirical potentials. While some potentials had been checked against *ab initio* methods,[81] no real *ab initio* study was performed so far. Therefore, one topic of this work is the calculation of the melting line of helium, especially for pressures above 1 Mbar, where no other reliable data is available, see chapter 3.

Hydrogen-helium alloys

The phase diagrams of alloys are often very complicated, even for simple binary systems. A schematic phase diagram for hydrogen-helium alloys is shown in figure 1.4, as proposed by Streett[84] and van den Bergh *et al.*[85]

Very little work has been done on the stability of solid hydrogen-helium alloys. The experimental results are limited to pressures of about 0.1 Mbar at room temperature.[85–89] These results could be reproduced by theoretical works.[90;91] However, the main topic of all these works is the phase separation of hydrogen and helium, mainly in the fluid. Also, all further theoretical work is concentrated on the phase separation either in the solid or the liquid, but not on their melting.

1.4.2. Plasma phase transition

One of the most discussed transitions at high pressures is the nonmetal-to-metal transition in dense hydrogen and helium.[92–94] Both elements have a large band gap at ambient conditions, with the band gap of helium of more than 20 eV being the biggest band gap of all elements. Thus, both el-

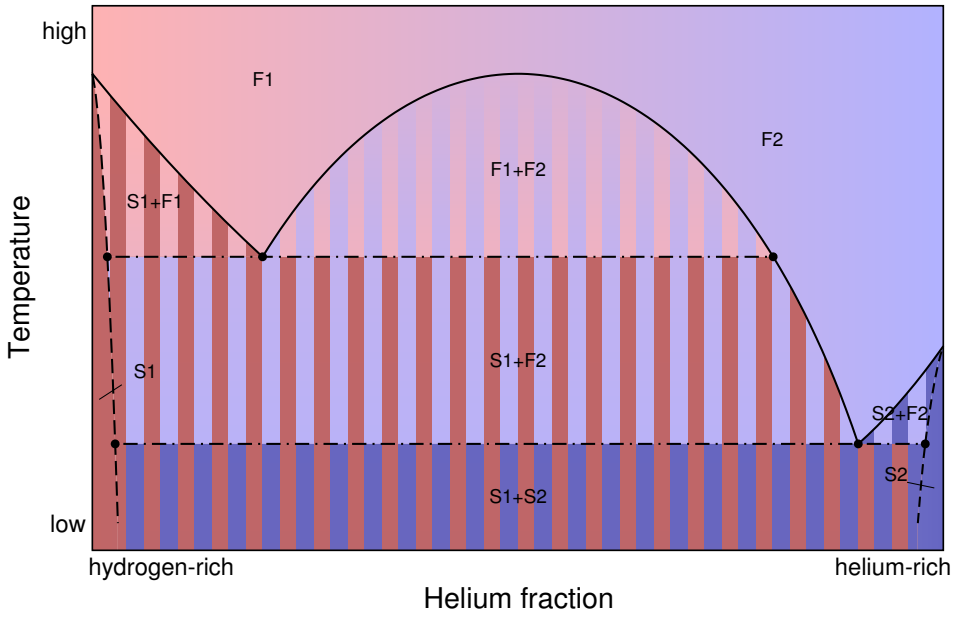

Figure 1.4.: Schematic phase diagram of hydrogen and helium, as proposed by Streett[84] and van den Bergh *et al.*[85] The occuring phases are color-coded from light red (fluid hydrogen) to light blue (fluid helium and from dark red (solid hydrogen) to dark blue (solid helium). F1 and F2 denote hydrogen-rich and helium-rich fluids, respectivly, S1 and S2 are defined analogous for the solids. Hatched areas indicate two-phase equilibria.

ements are insulating at these conditions. But the possibility of a metallic modification of hydrogen was already discussed by Wigner and Huntington[95] in 1935, and in 1949 Mott discussed the transition from a nonmetallic to a metallic state due to the band gap closure at high densities.[96;97] While the principal occurrence of this transition was uncontroversial, a lively discussion arose whether this transition is accompanied by a first-order phase transition or not, if it extends to finite temperatures, and where the critical point of this plasma phase transition (PPT) is located.[98]

Hydrogen

Many EOS models based on the chemical picture predict a pronounced first-order transition with critical points up to 19000 K (see figure 1.5),[8;15;99–105] but there are huge differences in their predicted coexistence lines and their critical points. While the transition to liquid metallic hydrogen was observed experimentally[42;106;107] by measuring a drastic increase in electrical conductivity, the first-order transition could not be confirmed at these conditions. New experiments showed first signs of such a first-order transition,[108] however, with inconclusive results. Additionally, no *ab initio* theories based on the physical picture could confirm a first-order phase transition at these high temperatures, while they could reproduce the experimental results for the nonmetal-to-metal transition.[16;109;110] Recently, clear signs of a first-order transition were found by theories,[68;111–114] however, at much lower temperatures. The latest results by Morales *et al.*[68] and Lorenzen *et al.*[113]

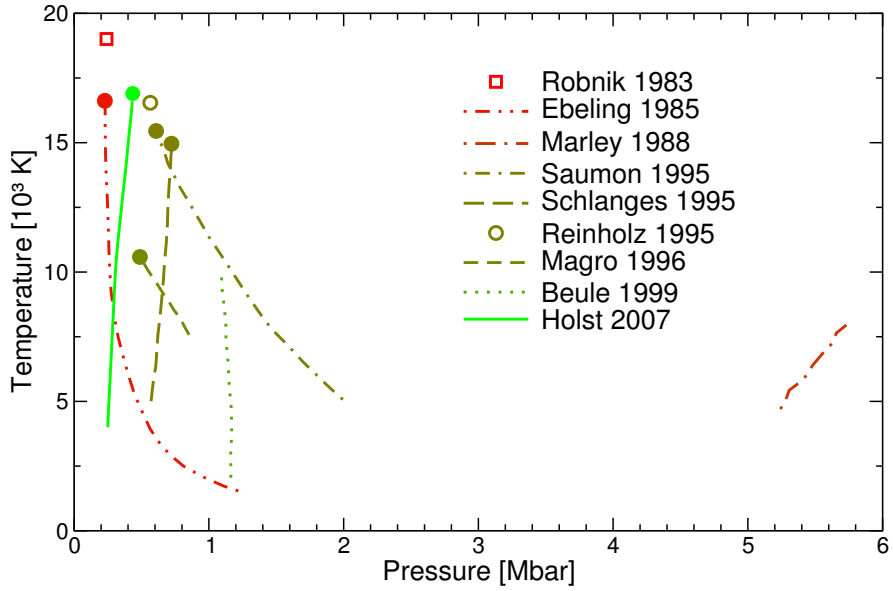

Figure 1.5.: Coexistence lines of the PPT proposed by various chemical models.[8;15;99–105] The publication dates are color-coded from red (old) to green (new).

(which is part of this work, see chapter 4) show conclusive evidence for a first-order transition in the liquid at temperatures below 2000 K. The search for solid metallic hydrogen in DAC experiments is still ongoing,[115] and the latest results by Eremets and Troyan[34] have already been questioned.[116]

Helium

The nonmetal-to-metal transition is expected to occur in helium as well, but due to the larger band gap at much higher pressures and temperatures compared to hydrogen.[61;117–120] Also for helium first-order transitions were proposed by chemical models,[121;122] one first-order transition for each ionization state. Although the nonmetal-to-metal transition has yet to be shown in experiments, at least the transition to a semiconducting state was demonstrated by reflecitvity measurements.[120] Again neither experiments nor *ab initio* theories found evidence for a first-order phase transition.[27;61] However, this might change in the future due to the new developments for hydrogen and a renewed interest in helium. One key difference which might be important for this question is the abscence of molecules, which play an important role in the first-order phase transition in hydrogen.[68;113]

Hydrogen-helium mixtures

Very little work was done on the nonmetal-to-metal transition in hydrogen-helium mixtures. Few shock wave experiments have been performed[123;124], and several first-order transitions in H-He mixtures were proposed by a chemical model.[102] The only *ab initio* calculations so far were performed by Chacham *et al.*[125], who calculated the band gap closure of solid hydrogen-helium mixtures with

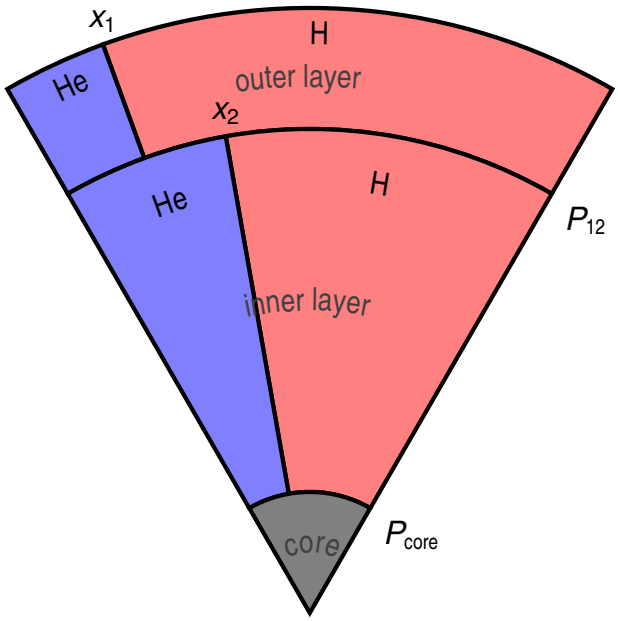

Figure 1.6.: Schematic interior structure of giant planets in the three layer model. Not shown are the heavier elements.

different helium fractions. Vorberger *et al.*[112] studied the effect of helium on the dissociation of hydrogen and found a stabilization of the hydrogen molecules due to the helium atoms. Part of this work will be a more detailed analysis of the metallization in hydrogen-helium mixtures, see chapter 5 and section 8.5.

1.4.3. Phase separation

As already mentioned in section 1.4.1, another important effect is the phase separation, or demixing, of hydrogen and helium, which has long been proposed to occur at high pressures.[126–131] This effect was experimentally confirmed for mixtures of molecular hydrogen and helium at moderate pressures[31;84;88;89] and could be reproduced by theoretical works.[90;91;132] However, the predictions at higher pressures, especially in the metallic phase of hydrogen, vary by large amounts, making reliable assumptions, for e.g. planetary modeling, very difficult. Chapters 3, 5, and 8 deal with this phase separation and its consequences in more detail. Especially the deep connection between the nonmetal-to-metal transition and the phase separation will be discussed in chapter 5.

1.5. Planetary modeling

A very important application for the properties of hydrogen and helium are interior structure models of giant planets like Jupiter and Saturn.[133–137] On the one hand, they need an accurate EOS as input, on the other hand, many of the previously described effects might occur inside these objects.

One widely used interior structure model is the so-called three-layer model, which is schematically shown in figure 1.6. It consists of a solid core of ices or rocks and two fluid layers, consisting of hydrogen, helium, and heavier elements, often summarized as metals (which are not shown in the figure for simplicity). Further assumptions in these models are a homogeneous composition inside the layers and an isentropic pressure-temperature profile inside these fluid layers. Both assumptions are reasonable if the layers are convective.[138] It is known from observation that the helium content in the atmosphere[139] is lower than the mean helium content,[140] which implies a higher helium fraction in the inner layer, i.e. $x_1 < x_{\text{mean}} < x_2$. Both the PPT of hydrogen and the demixing of hydrogen and helium have long been proposed as a cause for this discontinuity.[141;142] Additionally, the release of gravitational energy due to the heavier helium might explain the excess luminosity of Saturn.[141]

A typical interior structure calculation of a planet uses the observed helium content in the atmosphere and the mean helium content, the surface-temperature (1 bar level), the rotational speed, the total mass, the gravitational moments, and the radius as input parameters. The transition pressure is used as a free parameter and typically amounts to few megabars. The distribution of heavy elements in both layers is then optimized to reproduce the measured gravitational moments. A valid model is obtained, when all observational constraints are fulfilled. From this valid model the core mass, the distribution of heavy elements, and the helium fraction in the inner layer can be extracted. The core mass can be compared to planet formation models and therefore might give an insight into the planetary formation mechanism (core accreation or disk instability).[143;144] The amount of heavy elements in the outer layer is an additional quantity, which can be compared to observations.

A further important check of the interior structure model is the comparison to calculations of the phase separation. Assuming that the demixing and the following rain-out of helium is fast compared to the evolutionary timescale, the helium distribution in the planet should not enter the miscibility gap.[128] This condition, which will be called “thermodynamic stability” in the following, is usually fulfilled for Jupiter, but more problematic for Saturn. Apart from this check, an accurate knowlegde of the miscibility gap is of paramount interest for evolution models. For the planetary evolution, many interior structure models from the planet’s hotter past have to be calculated, where no observation for its helium contents (and the gravitational moments) is available. However, since the planet cools down it is evident that the overlap with a possible miscibility gap and, consequently, the helium contents in the two layers will change over time. So far, evolution calculations for Jupiter yield the correct age of about 4.5 Gyr without considering demixing effects, while those for Saturn yield only half that age.[141] Calculations with estimated miscibility gaps show the potential to reach the correct age when an inhomogenous helium distribution due to phase separation is taken into account.[141;142] Therefore, the implications of the miscibility gap for the helium distribution and a scheme to extract the relevant input quantities (outer helium fraction x_1 and transition pressure P_{12}) are outlined in section 8.3.

1.6. Outline of this thesis

This work is subdivided into three parts. Part I (this part) gives a general introduction into the topic of hydrogen and helium at high pressures (chapter 1) and a more detailed introduction into the applied FT-DFT-MD method (chapter 2). Since this is a cumulative thesis, the main part are

the three publications (Lorenzen *et al.* (2009),[145] Lorenzen *et al.* (2010),[113] and Lorenzen *et al.* (2011),[146] in the following abbreviated as Paper I, Paper II, and Paper III, respectively) in part II. Each publication is introduced in an individual chapter. The third part consists of further important results, which have not been published yet, e.g. for the nonmetal-to-metal transition in hydrogen (chapter 6), the equation of state and phase diagram of helium (chapter 7) and results for the EOS, electrical and thermal conductivity, and the nonmetal-to-metal transition in hydrogen-helium mixtures (chapter 8). This work is concluded by a summary and outlook in part IV. Extensive convergence tests for all obtained quantities are reported in the appendix in part V.

2. Method

As it was outlined in chapter 1, different methods exist to study matter under extreme conditions. In this chapter, FT-DFT-MD simulations, which are used for all results of this work, will be discussed in more detail. However, it is not meant as a full derivation of (FT-)DFT but it should lay out the basic principles and concepts. For a more detailed review of DFT, see e.g. Jones and Gunnarsson[147] or Engel and Dreizler.[148]

FT-DFT-MD simulations combine classical molecular dynamics simulations for the ions with DFT-calculations for the electrons. This is based on the Born-Oppenheimer approximation which is possible due to the large ratio between the ion and electron masses. The basic ideas of both treatments (DFT and MD) are outlined in sections 2.1 and 2.2, while its combination and implementation is described in section 2.3.

2.1. Molecular dynamics simulations

In molecular dynamics (MD) simulations, the equations of motion of a many particle system are solved numerically.[149–151] Since it is not possible to treat arbitrary large numbers of particles inside the simulation, very often periodic boundary conditions are used. Of course, this can influence the accuracy of the results, and the convergence with respect to the particle number has to be checked very carefully. Usually this is not so much an issue for classical MD simulations, since the particle numbers can be very high with modern computer equipment (e.g. $N \geq 10^7$ particles).[152] However, for the FT-DFT-MD simulations this might be very different, since the particle numbers are usually much smaller (in the order of 10^2).

Of course, the integration of the equations of motion is only possible if the forces acting on the particles are known. A model pair potential (like e.g. Lennard-Jones)[153] is used in many MD simulations, which can be implemented very easily. However, this has various limitations, because the exact potential is not known and even then it is only valid for a small parameter range. In this sense MD simulations with pair potentials have limited predictive power. But especially for helium classical MD simulations are still applied regularly, however, always with the uncertainty of the used potential.[81] To circumvent this problem, the forces on the ions have to be calculated *ab initio*, for example with DFT, which is described in section 2.2.

In its simplest form, MD simulations are performed in the microcanonical ensemble, i.e. the density of the system and the total energy are fixed for the simulation. For many practical simulations one wants to fix the density and the temperature instead, i.e. to simulate in the canonical ensemble. To achieve this, a thermostat has to be applied to the system, which basically removes heat when the temperature is too high and adds heat when the system is too cold. While this principle is straightforward, the real implementation is more involved, since the dynamics of the particles should be changed as little as possible. Therefore various different thermostats have been proposed in the

past, with different level of accuracy and complexity.[154–159] In this work the Nosé-Hoover thermostat is used, which couples the ions to an external heat bath, and gives accurate results when the frequency of the thermostat is adjusted to be similar to typical oscillations in the system, like the molecular vibration of hydrogen.

2.2. Density functional theory

2.2.1. Theorems of Hohenberg and Kohn

The solution of the many-particle Schrödinger equation requires an enormous amount of dimensions which is not feasible for more than a few (< 10) electrons. This problem can be cirumvented by the density functional theory, which deals with the quantum mechanical description of electrons in an external potential. It is based on the the theorems of Hohenberg and Kohn,[160] which state:

1. If two (electron) systems with an external potential $v_1(\mathbf{r})$ and $v_2(\mathbf{r})$ have the same ground-state density $n(\mathbf{r})$, then the potentials can only differ by a constant.

2. The density functional $E[n(\mathbf{r})]$ has its minimum at the ground-state density.

This was generalized to finite temperatures by Mermin,[18] where a functional $\Omega[n(\mathbf{r})]$, corresponding to the grand potential, or, more relevant for this work, a free energy functional $F[n(\mathbf{r})]$ is used instead of $E[n(\mathbf{r})]$. These theorems have a huge advantage over the usual formulation of quantum mechanics, because they basically say that we do not need to solve the many particle Schrödinger equation, we ”only“ need to find the electron density which yields the minimum energy. The difficult part is, how to find the ”correct“ energy functional $E[n(\mathbf{r})]$ and how to calculate from this the groundstate energy and density.

2.2.2. Exchange-correlation functionals

The basis of DFT is the energy functional $E[n(\mathbf{r})]$. While Hohenberg and Kohn and Kohn and Sham proposed functionals for constant and slowly varying density, the search for accurate functionals is still ongoing and the results of the calculations can depend heavily on the used functional.[162] Formally, the energy functional can be written in the form

$$E[n(\mathbf{r})] = V_{\text{ext}}[n(\mathbf{r})] + U_{\text{H}}[n(\mathbf{r})] + T_{\text{s}}[n(\mathbf{r})] + E_{\text{XC}}, \tag{2.1}$$

where

$$V_{\text{ext}} = \int v_{\text{ext}}(\mathbf{r}) n(\mathbf{r}) d^3 r \tag{2.2}$$

is the energy due to the external potential $v_{\text{ext}}(\mathbf{r})$,

$$U_{\text{H}}[n(\mathbf{r})] = \frac{1}{2} \int \int \frac{n(\mathbf{r}) n(\mathbf{r}')}{|\mathbf{r} - \mathbf{r}'|} d^3 r d^3 r' \tag{2.3}$$

	Heaven of chemical accuracy	
+ explicit dependence on unoccupied orbitals	rung 5	fully nonlocal
+ explicit dependence on occupied orbitals	rung 4	example: hybrid functionals
+ explicit dependence on kinetic energy density	rung 3	meta-GGAs
+ explicit dependence on gradients of the density	rung 2	GGAs
local density only	rung 1	LDA
	Hartree world	

Table 2.1.: Jacob's ladder of XC functional approximations, after Perdew *et al.*[19] Each rung yields more accuracy, but is also computationally more demanding. In this work mainly the PBE-GGA (red) is used, and some preliminary results with the HSE hydrid functional (green) are presented.

is the Hartree energy,

$$T_s[n(\mathbf{r})] = \sum_i^N \int \phi_i^*(\mathbf{r}) \left(-\frac{1}{2}\nabla^2\right) \phi_i(\mathbf{r}) d^3r \tag{2.4}$$

is the Kohn-Sham kinetic energy, and E_{XC} is the so-called Exchange-Correlation (XC) functional. Note that Hartree atomic units are used throughout this chapter. In this XC functional all unknown properties of the interacting system are gathered, and this functional is the central ingredient for DFT calculations. A schematic table of possible XC functionals is presented in table 2.1.

The simplest approximation is the local density approximation (LDA),[161;163;164] where the XC contribution is calculated for a homogeneous electron gas at the local density $n(\mathbf{r})$. This treatment is correct for slowly varying electron densities and yields the correct limiting case for very high densities. Generalized gradient approximations (GGA) are a better approach, where the XC functional depends not only on the electron density, but also on its gradient. The GGA by Perdew, Burke, and Ernzerhof (PBE)[165] is used throughout this work, except for few calculations with the hybrid functional by Heyd, Scuseria, and Ernzerhof (HSE).[166;167] Even better XC functionals are computationally much more demanding, and up to now not feasible for large-scale simulations, see also chapter 4 and section 6.2.

Since the beginning of DFT in 1965 up till now more than 50 XC functionals have been developed, partly based on empirical data and partly based on *ab initio* theory. A nice overview can be found in Ref. 168. Several works are dedicated to benchmarking different functionals for e.g. lattice constants,[162;169–173] bulk moduli,[169;170] bond length,[174–176] and band gaps.[170;171] In general, there is no XC functional which performs equally well for all properties and all elements. The PBE functional, which is used in this work, yields often not the most accurate results, but for many applications it performs quite good compared to its computational demands. Additionally, it is an *ab initio* functional in the sense that it is nonempirical. One of the main problems of the PBE functional (and other LDA and GGA functionals as well) is the self-interaction error, i.e. they are not self-interaction free, leading to too small band gaps.[177;178] In principle, this can be improved by better functionals like HSE,[170;178] however, with much higher computational costs, see also section 6.2.

2.2.3. Kohn-Sham equations

The Hohenberg-Kohn theorems were used by Kohn and Sham [161] to derive a set of equations

$$\left(-\frac{1}{2}\nabla^2 + v_{\text{eff}}(\mathbf{r})\right)\phi_i(\mathbf{r}) = \varepsilon_i\phi_i(\mathbf{r}) \tag{2.5}$$

$$n(\mathbf{r}) = \sum_i^N |\phi_i(\mathbf{r})|^2 \tag{2.6}$$

$$v_{\text{eff}} = v_{\text{ext}}(\mathbf{r}) + \int \frac{n(\mathbf{r}')}{|\mathbf{r}-\mathbf{r}'|} d^3r' + \frac{\delta E_{xc}}{\delta n(\mathbf{r})}, \tag{2.7}$$

which have to be solved self-consistently, thus reformulating the many-body Schrödinger equation into a set of effective one-particle Schrödinger equations. Hereby, an iterative recipe to solve the problem is available, by starting from a guessed groundstate density $n(\mathbf{r})$, constructing the effective potential v_{eff} (equation 2.7), solving equation 2.5, and calculating the new density $n(\mathbf{r})$ (equation 2.6). This iteration has to be performed until the energy is converged, see also figure 2.2 in section 2.3.

2.2.4. Plane waves, pseudopotentials, and the PAW method

For the evaluation of the Kohn-Sham equations, one has to represent the wavefunctions in a convenient way. Many available codes (and also the one used in this work) use an expansion into plane waves, which have usefull features for calculations, e.g. the implementation of periodic boundary conditions is straightforward and fourier transformations can easily be done. One problem of plane waves is the representation of the wavefunctions near the ions, since the Coulomb potential leads to strong oscillations. To represent these oscillations many plane waves are needed, which make calculations very demanding, see also section A.1.1. To circumvent this problem, pseudopotentials were introduced. The general idea is to replace the wavefunctions inside a sphere around the ions with smooth functions, without changing the physical outcome of the calculations. The first pseudopotentials introduced where the so-called norm-conserving pseudopotentials, [179;180] which conserved the norm of the wavefunctions at the sphere boundary. But still, for some elements, e.g. transition-metal elements or elements with *d* or *f* electrons, very "hard" pseudopotentials, i.e. small sphere cutoff radii, are needed, which still leads to high plane wave cutoffs. This could be solved by ultrasoft pseudopotentials, [181] which relaxed the norm-conserving condition at the cost of a more involved pseudopotential generation. However, these generated pseudopotentials have to be tested extensively. [182] A better approach is the projector augmented wave (PAW) method, [182;183] which is based on a linear transformation between the all-electron and pseudo-wavefunctions. In principle, all these techniques are only of a technical nature, i.e. they should only reduce the computational costs without changing the physical outcome. This has to be checked carefully in convergence tests with respect to plane wave cutoff (number of plane waves), and the radial augmentation cutoff, see section A.1.1.

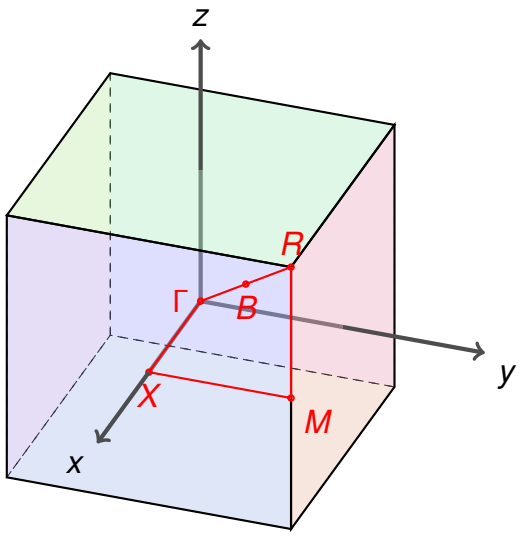

Figure 2.1.: Special points of the simple cubic Brillouin zone. Common choices for FT-DFT-MD simulations are the Γ point at $(0, 0, 0)$ and the Baldereschi mean value point (B) at $(\frac{1}{4}, \frac{1}{4}, \frac{1}{4})$.[184]

2.2.5. Periodic boundary conditions and **k**-point sampling

Due to the periodic boundary conditions it is necessary to perfom some of the calculations in reciprocal space by integrating over the Brillouin zone. However, for FT-DFT-MD simulations it is not possible (and usually not needed) to sample the Brillouin zone with a very fine grid, so that the integration is replaced by a summation over some special **k** points. In fact, often only one special **k** point is needed, but obviously this calls for convergence tests with respect to the **k**-point sampling, see section A.1.2. There are several possibilities to sample the Brillouin zone (see figure 2.1). One very common way for FT-DFT-MD simulations is to use only the Γ point. Choosing this point has (apart from being only one point) the advantage that the wavefunctions have real values and the code does not need to deal with complex numbers, which can speed up the calculations. The disadvantage is, that it has to be very carefully checked if the results are converged, which is sometimes only the case for higher particle numbers compared to other choices.

A common method for choosing more **k** points is the method of Monkhorst and Pack,[185] where a discrete grid of **k** points is generated.

One other special point which can be used is the so called "Baldereschi mean-value point" (BMVP),[184] which has the advantage that many quantities converge very fast with respect to higher k-point sets. Therefore this point is used for all calculations in this work, except where noted otherwise.

2.3. FT-DFT-MD

By using the Born-Oppenheimer approximation, one can perform classical MD simulations for the ions, and use DFT for the electrons. The basic principle is illustrated in figure 2.2. Like the classical

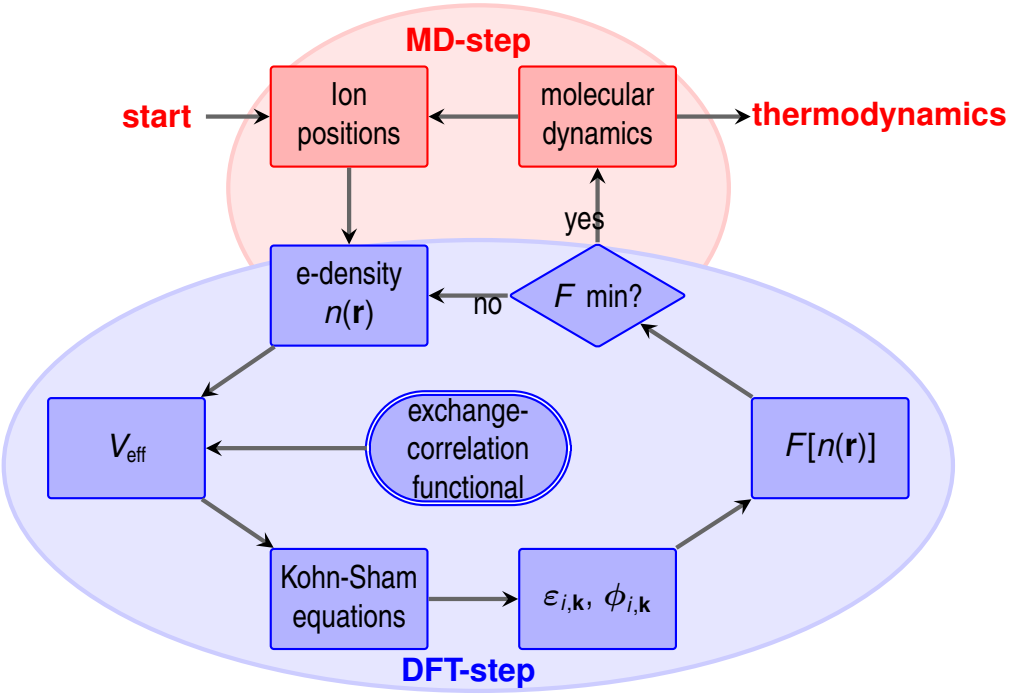

Figure 2.2.: FT-DFT-MD workflow as implemented in VASP. The foundation of the method is the DFT calculation (blue), which is performed for each MD step (red). Central ingredient for the DFT calculation is the chosen XC functional.

MD simulations it starts with an ion configuration inside a simulation box. These ions provide the external potential for the DFT calculations for the electron system. With a (guessed) initial electron density $n(r)$ the Kohn-Sham equations are solved, and from the Kohn-Sham eigenvalues and wavefunctions a new electron density and the resulting energy functional can be calculated. This procedure can be repeated with the new electron density, until the energy functional reaches its minimum. Afterwards the forces on the ions are calculated from the Hellman-Feynman theorem,[186] and as in the classical MD simulations the ions are moved in a finite timestep. In this way the forces are calulated *ab initio* for each time step and the fundamental problem of classical MD simulations (knowing the potential) can be solved. This workflow is implemented in several codes; in this work the code VASP[187–190] is used.

2.4. Electrical and thermal conductivity

Within DFT the dynamic electrical conductivity can be calculated with the Kubo-Greenwood formula[191–196]

$$\sigma(\omega) = \frac{2\pi}{3V\omega} \sum_{\mathbf{k}} w_{\mathbf{k}} \sum_{j=1}^{N_b} \sum_{i=1}^{N_b} \left[f_{j,\mathbf{k}} - f_{i,\mathbf{k}} \right] \times \left| \langle \phi_{j,\mathbf{k}} | \hat{\mathbf{p}} | \phi_{i,\mathbf{k}} \rangle \right|^2 \delta\left(\varepsilon_{i,\mathbf{k}} - \varepsilon_{j,\mathbf{k}} - \omega \right), \tag{2.8}$$

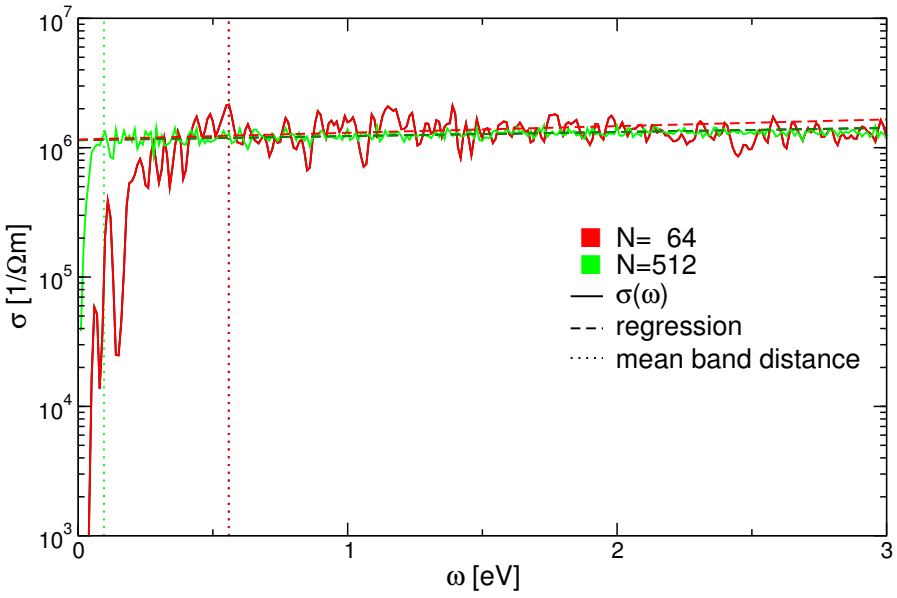

Figure 2.3.: Electrical conductivity $\sigma(\omega)$ (solid lines) at 1 g/cm^3 and 1000 K for two snapshots with 64 (red) and 512 (green) electrons. The mean band distances are marked with dotted lines, the fits (dashed lines) are applied between each mean band distance and 2 eV.

where V is the volume of the simulation box and ω the frequency. The summation over the matrix elements of the Kohn-Sham orbitals with the momentum operator $\hat{\mathbf{p}}$, weighted with the difference of the fermi occupation numbers $f_{i,\mathbf{k}}$, is performed over all N_b bands. This is, however, very time consuming and needs much disk space. Therefore, it cannot be calculated for each time step of the simulation, but only for snapshots of the simulation. Convergence tests have to be done with respect to the **k**-point summation,[197] see section A.3. Additionally, it is possible within the Kubo theory to derive the thermal conductivity and the thermopower,[196] however, only few results for the thermal conductivity are shown in section 8.4. While it is possible to calculate optical properties like the reflectivity from the dynamic conductivity,[198] only results for the static limit ($\omega \to 0$) are obtained in this work.

Since the Kubo-Greenwood formula evaluates transitions between discrete energy eigenvalues ($\delta\left(E_{i,\mathbf{k}} - E_{j,\mathbf{k}} - \omega\right)$), the electrical conductivity is zero most of the time and has only finite values when the frequency ω is equal to an exact energy difference between two bands. To circumvent this (unphysical) problem, the δ-function is replaced by a Gaussian with a finite width. Depending on this width the dynamical conductivity will be more or less smooth.

But still, the conductivity would drop down for small ω, approximately when ω is smaller than the mean band distance. In general this effect can be reduced with higher particle numbers, since then the mean band distance gets smaller. Nevertheless, the direct limit of $\omega = 0$ cannot be reached, see figure 2.3. Two approaches are possible for obtaining this limit. In the first approach, the width of the Gaussian can be increased, until smooth functions up to $\omega = 0$ are obtained. But especially for small particle numbers the obtained static conductivity would depend very much on the chosen

width and the results would be to some extend arbitrary. A better approch is to perform a regression (either a linear or an exponential function) in the area of small frequencies which are still higher than the mean band distance. By this approach the unphysical drop in the conductivity due to the finite system size is ignored, but a reasonable limit can be obtained. This is demonstrated in figure 2.3 for two different particle numbers. Both functions drop down over several orders of magnitude for frequencies smaller than the mean band distance. Although this occurs much earlier for the lower particle number, both static limits coincide.

Note that this Kubo-Greenwood formalism applies only to the electronic contribution to the conductivity. In principle it is possible to calculate the ionic conductivity from DFT-MD simulations,[199] but the effective charges carried by each ion have to be known, which is very involved for complex mixtures.[200]

2.5. Outline of the results

The main results obtained with this method are the publications in part II, where each publication has a separate chapter together with a short introduction. In chapter 3, results for the miscibility gap of hydrogen and helium at high pressures are shown, together with a discussion of its impact on Jupiter and Saturn. Chapter 4 deals with the first-order liquid-liquid phase transition in pure hydrogen from a nonmetallic molecular to a metallic ionic phase. Finally, in chapter 5, the deep connection between both effects is studied in more detail, and again the impact on giant planets is shown.

Further yet unpublished results for the nonmetal-to-metal transition in hydrogen (chapter 6) and hydrogen-helium mixtures (section 8.5), as well as results for the EOS of helium (sections 7.1 to 7.4) and hydrogen-helium mixtures (section 8.1) are topic of part III. In addition, a high pressure phase diagram of helium is shown in 7.4 in comparison to available experimental melting line data. In section 8.4, the electrical and thermal conductivity along the isentrope of Jupiter is shown, which is also part of Ref. 201.

Part II.

Publications

3. Demixing of Hydrogen and Helium at Megabar Pressures

As it was outlined in sections 1.4.3 and 1.5, one important effect for planetary modeling is the possible phase separation or demixing of hydrogen and helium. The aim of this first publication (Paper I) was to calculate the miscibility gap of hydrogen and helium with up-to-date *ab initio* methods, to improve the unsatisfactory situation of various contradicting results obtained so far.[126;129–131] The simulations were performed with particle numbers between 32 and 64 ions, the number of electrons was fixed at 64. These particle numbers are enough to get an overall well converged EOS (see section A.1.2, but they are small enough to prevent any direct demixing effects in the simulation box (see chapter 5). In this way, an accurate double tangent construction is possible. The only "uncontrolled" approximation in this approach is the use of the ideal entropy of mixing. Recently efforts were reported to circumvent this approximation by thermodynamic integration.[202] These results showed a decreased demixing temperature compared to the results by applying the ideal entropy of mixing. However, due to the additional need of EOS data for the thermodynamic integration, fewer helium fractions could be considered, making the double tangent construction more error-prone. The work of Morales *et al.*[202] was performed in parallel to this one and showed a good independent confirmation of the phase separation.

In this work, the pressures of 4, 10, and 24 Mbar were considered, as in the publication by Pfaffenzeller *et al.*[131] This made it possible to compare the results of the rather similar approaches directly. While the general agreement between both works was definitly better than the agreement with the older results by Klepeis *et al.*,[130] a much more refined view of the miscibility gap could be shown. The biggest advancement was, however, not the use of a better functional (PBE instead of LDA) or the use of BOMD instead of CPMD, but the evaluation of more different helium fractions with a much more extensive data set. This allowed a better double tangent construction without forcing a symmetric miscibility gap as in Pfaffenzeller *et al.*[131] This refined evaluation revealed a very asymmetric miscibility gap, which already gave hints to the involved interplay between melting, metallization, and demixing. Especially the connection between metallization and demixing, which was already known from similar systems like He-Hg,[203] was then topic of further work (Paper III, chapter 5). To explain the demixing behavior at high helium fractions it was necessary to calculate the melting line of helium at these high pressures, since there is no other reliable data (either experimentally or theoretically) available to date. The applied method is, however, not able to make predictions about solid-fluid phase equilibria as shown in the schematic phase diagram in figure 1.4, section 1.4.1. Additionally, no predictions about the stability of solid hydrogen-helium alloys were made, for the construction of the miscibility gap in Paper I it was assumed that these alloys are completely immiscible.

Demixing of Hydrogen and Helium at Megabar Pressures

Winfried Lorenzen, Bastian Holst, and Ronald Redmer
Institut für Physik, Universität Rostock, D-18051 Rostock, Germany
(Received 6 October 2008; published 16 March 2009)

We present results of *ab initio* finite-temperature density functional theory molecular dynamics simulations for fluid hydrogen-helium mixtures at megabar pressures. The location of the miscibility gap is derived from the equation of state data. We find a close relation between hydrogen-helium phase separation and the continuous nonmetal-to-metal transition in hydrogen. Our calculations predict that demixing of hydrogen and helium occurs in Saturn and probably also in Jupiter. These results will have a strong impact on interior models of giant solar and extrasolar planets.

DOI: 10.1103/PhysRevLett.102.115701 PACS numbers: 61.20.Ja, 31.15.A−, 64.30.−t, 71.30.+h

Author contributions

W.L. Preparation of the manuscript, all calculations for the miscibility gap and the phase diagram of helium.

B.H. Preparation of the manuscript, calculations for the electrical conductivity.

R.R. Supervision of the project, preparation of the manuscript.

4. First-order liquid-liquid phase transition in dense hydrogen

Since it was clear from the previous publication (Paper I) that the metallization of hydrogen plays an important role in the demixing of hydrogen and helium, work began to study this process in more detail. As a criterium for metallization the electrical conductivity was evaluated for isotherms as function of the pressure. This revealed a discontinuity at a given pressure, where the conductivity jumped from values below metallic-like to metallic-like values (figure 3, Paper II). This discontinuity was then systematically studied in terms of the EOS (figure 2) and radial distribution functions (RDF) (figure 4). Finally, a new phase diagram could be proposed in figure 6, with a coexistence line of a first-order liquid-liquid phase transition from a nonmetallic to a metallic phase. It can be seen from the RDFs, that the nonmetallic phase contains considerable more hydrogen molecules than the metallic phase. In such a way, it is also a phase transition from a molecular to an atomic phase. However, it should be noted that these phases are not pure molecular or pure atomic. Again these results were obtained in parallel by Morales *et al.*,[68] in general with good agreement between both works. Morales *et al.* performed additionally CEIMC calculations which already showed the general problem that PBE-DFT has a too small band gap. Therefore, the results by CEIMC are shifted to higher temperatures and pressures. Since the confirmation of this first-order transition, its study is still ongoing, see e.g. Liberatore *et al.*[114]

Both works disagreed about the location of the critical point of this transition. While Morales *et al.* found signs of a first-order transition for temperatures up to 2000 K, here, the transition was already continuous at temperatures of 1500 K. This is probably partly due to a more accurate density and temperature grid in this work. Another reason might be the bigger particle number in this work, which showed the continuous transition with less noise. The influence of the particle number on the transition pressure is studied in section 6.1 in more detail, which so far was not done in much detail in any publication (including Paper II). This convergence study shows good convergence for 512 atoms, which was used here. This should be checked for the results of Morales *et al.*[68] as well, especially for the CEIMC results which were obtained with 54 to 128 atoms.

Although the convergence of the transition pressure was not studied in detail in Paper II, one additional important result was the complex convergence behavior with respect to the **k**-point sampling and particle number (figure 1), which is discussed in more detail in section A.2.1. Indications of this behavior were already found previously,[53;68;110] however, here it could be shown that this behavior is much less prominent with a better **k**-point sampling. At the time of the publication it was assumed that this difficult convergence behavior is due to the vicinity of the phase transition, however, the later performed tests at 4 g/cm^3, i.e. far away from this transition, showed qualitatively the same behavior (see section A.2).

PHYSICAL REVIEW B **82**, 195107 (2010)

First-order liquid-liquid phase transition in dense hydrogen

Winfried Lorenzen, Bastian Holst, and Ronald Redmer
Institut für Physik, Universität Rostock, D-18051 Rostock, Germany
(Received 28 May 2010; revised manuscript received 23 September 2010; published 9 November 2010)

We use *ab initio* molecular-dynamics simulations to study the nonmetal-to-metal transition in dense liquid hydrogen. By calculating the equation of state of hydrogen at high pressures up to several megabars and temperatures above the melting line up to 1500 K we confirm the first-order nature of this transition at these temperatures. We characterize both phases based on equation of state data, the electrical conductivity, and the pair-correlation functions, which are all derived self-consistently from these simulations. We locate the respective transition line in the phase diagram and give an estimate for its critical point. We compare with available experimental data and other theoretical predictions.

DOI: 10.1103/PhysRevB.82.195107 PACS number(s): 64.70.Ja, 52.25.Fi, 61.20.Ja, 64.10.+h

Author contributions

W.L. Preparation of the manuscript, convergence tests, calculation of the isotherms, radial distribution functions, electrical conductivity, and the phase diagram.

B.H. Preparation of the manuscript, independent calculations for the electrical conductivity and isotherms with 256 atoms.

R.R. Supervision of the project, preparation of the manuscript.

5. Metallization in hydrogen-helium mixtures

It was already shown in Paper I that miscibility data at lower pressures than the calculated 4 Mbar is needed and some preliminary results for 1 and 2 Mbar were already included. Therefore, work started immediately to extend these calculations to 1 and 2 Mbar. The resulting miscibility gap for these lower pressures shows a very interesting behavior of an "island" of demixing (figure 4). It is clear from the conditions for metallization of hydrogen (Paper II, Refs. 68 and 110), that hydrogen is nonmetallic at 1 Mbar and temperatures below about 2000 K. Since Paper I already gave hints at the connection between demixing and metallization of hydrogen the explanation for the island of demixing seemed again to be the metallization. To confirm this explanation the metallization of hydrogen-helium mixtures is the central part of Paper III. Again the electrical conductivity is used as an indicator for metallization. Although there is no clear criterium for metallic conductivities at finite temperatures, values around the Mott minimum metallic conductivity at $T = 0$ of $\sigma = 2 \times 10^4 \frac{1}{\Omega m}$ are adopted. The results (figure 1) can explain very nicely the islands of demixing, as can be seen from the isolines of electrical conductivity in figure 4.

The different metallization behavior of hydrogen and helium can be explained by the density of states (figures 2 and 3). While the band gap of hydrogen closes completely at the shown conditions, which leads to a dramatic increase in conductivity, helium has an open band gap for all considered conditions.

As in Paper I, the relevance for Jupiter and Saturn is analyzed (figure 5). Although the quantitative deviations from the results of Morales *et al.*[202] are small, they might discriminate between the occurence or not-occurence of demixing in Jupiter. Therefore, this question is still open for Jupiter.

One additional result of Paper III is the direct simulation of demixing, which is only possible with large-scale simulations with big particle numbers, in this case 1024 hydrogen atoms and 512 helium atoms. While the impressive results (figure 6) and their evaluation (figures 7 and 8) agree qualitatively with the thermodynamically constructed miscibility gap, they are not suited for either assessing the validity of the ideal entropy of mixing, or deciding the question of demixing in Jupiter. On the one hand, this is due to the extreme computational demand, which makes it unfeasible for an extensive data set, especially at lower densities, where the computational time is even higher. On the other hand, these calculations still suffer from finite size effects like e.g. surface tension.

PHYSICAL REVIEW B **84**, 235109 (2011)

Metallization in hydrogen-helium mixtures

Winfried Lorenzen,[1] Bastian Holst,[1,2] and Ronald Redmer[1]
[1]*Institut für Physik, Universität Rostock, D-18051 Rostock, Germany*
[2]*CEA, DAM, DIF, F-91297 Arpajon, France*

(Received 2 September 2011; revised manuscript received 14 October 2011; published 1 December 2011)

Hydrogen-helium mixtures have long been predicted to undergo demixing at high pressures of several megabars which occur in the interiors of giant planets such as Jupiter and Saturn. This effect is most important to understand their evolution and current interior structure. *Ab initio* calculations have already proven their potential to give precise predictions for the demixing line for pressures above 4 Mbar, well above a first-order phase transition from molecular to metallic hydrogen. Here we calculate the miscibility gap for lower pressures between 1 and 2 Mbar using *ab initio* molecular dynamics simulations. By using the Kubo-Greenwood formula we obtain the electrical conductivity and reveal the close connection between metallization in the hydrogen subsystem and the location of the miscibility gap. Especially, we find direct evidence for H-He demixing by performing simulations for large particle numbers.

DOI: 10.1103/PhysRevB.84.235109 PACS number(s): 31.15.A−, 61.20.Ja, 62.50.−p, 64.30.−t

Author contributions

W.L. Preparation of the manuscript, calculations for the electrical conductivities, density of states, miscibility gap, and helium melting line. Simulations for the direct observation of demixing in the simulation box.

B.H. Preparation of the manuscript.

R.R. Supervision of the project, preparation of the manuscript.

Part III.

Further results

6. Hydrogen

6.1. Finite size effects on the plasma phase transition

The accurate calculation of phase transitions is a challenge for all simulation techniques. On the one hand, the underlying theory has to be valid for both phases and the transition region. On the other hand, the convergence of the calculations has to be checked very carefully. A very good example for this problem is the first-order nonmetal-to-metal transition in hydrogen. For example a MD simulation with empirical potentials will not reproduce the phase transition because the interaction of the hydrogen atoms will change dramatically and its full density and temperature dependence has to be known. Therefore an *ab initio* method like FT-DFT-MD is necessary. Since these methods are in general computationally involved, special care has to be taken for the convergence issue. This problem was already discussed for the **k**-point convergence in Paper II for one density and temperature condition. Here, additionally, the convergence of the transition pressure is investigated.

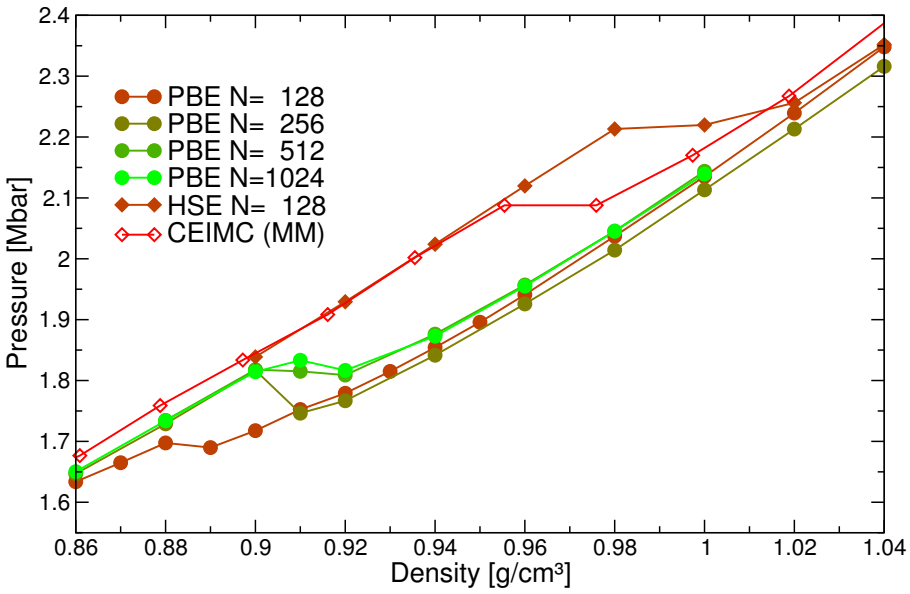

Figure 6.1.: First-order phase transition in hydrogen at 1000 K. Shown are FT-DFT-MD results with the PBE functional (filled circles, present work) with different particle numbers, results with the HSE functional with 128 particles (filled diamonds, present work), and the CEIMC results of Morales *et al.*[68] (open diamonds). The particle number is color-coded from low (red, 54) to high (green, 1024).

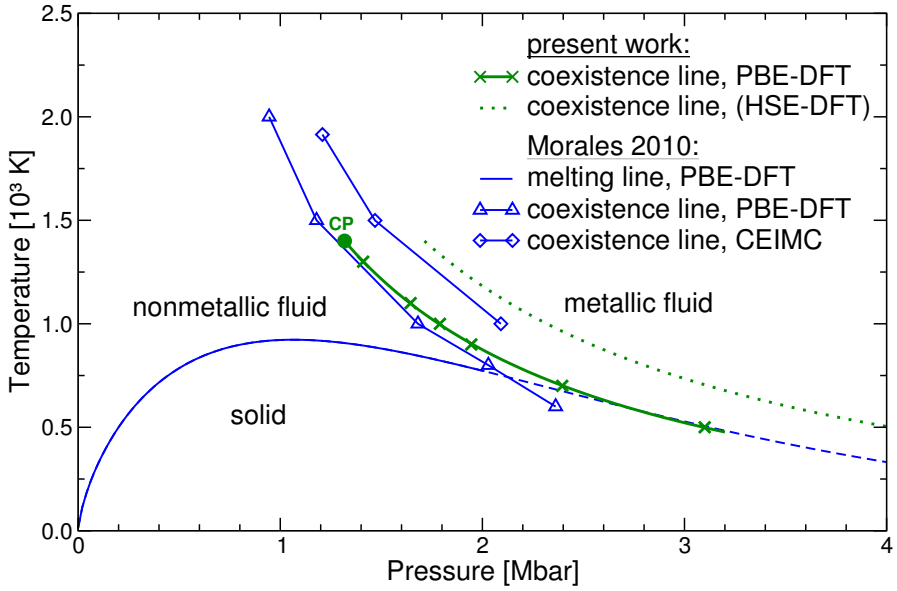

Figure 6.2.: High pressure phase diagram of hydrogen. The PBE-DFT and CEIMC results by Morales *et al.*[68] are shown in blue, the present work in green. The solid line is the result of Paper II, the dotted line indicates the estimated HSE-DFT result.

For this purpose, the first-order transition was calculated for the 1000 K isotherm with different particle numbers between 128 and 1024, which is shown in figure 6.1. A good convergence can be observed for a particle number of 512, which is also the number used in Paper II. Note that here only the convergence with respect to the particle number at a fixed **k**-point sampling (BMVP) is studied. So it might be possible to obtain converged results with a lower particle number, but better **k**-point sampling. This question is relevant, because the CEIMC results by Morales *et al.*[68] were obtained with a small particle number (54 atoms), but a very accurate **k**-point sampling ($4\times4\times4$ Monkhorst-Pack), see next section.

6.2. Plasma phase transition with HSE

One remaining problem is the too small band gap of PBE calculations, which is known for a long time.[163] A corrected band gap would shift the nonmetal-to-metal transition to higher pressures and temperatures, which could already be shown by Morales *et al.*[68] by employing the CEIMC method. Within DFT, band gaps can be calculated more accurately with the HSE functional,[166;170;178] i.e. a higher rung on Perdew's ladder of XC functionals (table 2.1, section 2.2.2). Although these calculations are much more involved (about 100 times), it was possible to calculate the first-order transition with 128 atoms with the HSE functional, using a screening parameter of 0.2/Å.[166;167] Both results (CEIMC and HSE-DFT) are shown in figure 6.1 and yield about 15% and 23% higher transition pressures, respectively. Since both calculations were performed with small particle num-

bers (CEIMC: 54 atoms with convergence tests with 128 atoms) a further increase of the transition pressure might occur, and the exact location of the first-order phase transition is still unclear. Under the assumption that the 1.3 fold increase of the transition pressure between the HSE and PBE simulations with 128 atoms holds also for the calculations with higher particle numbers, an estimated revised coexistence line can be obtained, which is shown in figure 6.2 in comparison to the so far published coexistence lines.[68;113] Although this simple estimate indicates the range of possible locations of the coexistence line, the location of the critical point is even more uncertain. However, this will be of great importance for an experimental verification of this first-order transition, since these high densities at low temperatures are very difficult to probe (see section 1.3).

7. Helium

7.1. Equation of state calculations

One aim of this work was the improvement and extension of the current helium EOS[61] as an input for modeling giant planets and brown dwarfs. When calculating a wide range EOS, special care has to be taken for several problems, which are outlined in the following.

While the PAW method works in general very well and reduces the computational cost dramatically, it will break down at ultrahigh densities. In principle, problems might arise if the PAW spheres start to overlap, i.e. when the particle distance is smaller than two times the PAW cutoff radius. However, very often the error is negligible[182] and problems arise only when the particle distance is smaller than the cutoff radius. The radial PAW cutoff of the standard helium potential supplied with VASP is about $r_c = 0.52$ Å. This corresponds to the mean particle distance of helium at a density of 11 g/cm^3. Since the EOS is needed also for densities of 100 g/cm^3 and above, it is clear that this potential is not sufficient. Therefore, a full Coulomb potential is used for densities above 10 g/cm^3, see also the convergence tests in section A.1.1. Due to this Coulomb potential, much higher plane wave cutoff energies are needed. A cutoff energy of 4000 eV was used for these calculations, which yields converged pressures to usually better than 1%. However, work is in progress to improve this convergence to better than 0.25%.

In addition to the difficulties at high densities, problems arise also at high temperatures. Since the occupation of the energy bands is determined by the fermi distribution, high temperatures lead to occupation of higher bands, especially for low densities. Therefore, it has to be ensured that enough bands are treated in the FT-DFT calculations. On the one hand, it is important for the used algorithm (RMM- DIIS)[204] to have enough free bands, on the other hand, it is important for the convergence of the calculations, see section A.1.3. However, the computational time scales roughly with N_{bands}^2 and the unnecessary use of too many bands should be avoided. This problem is amplified by the fact that low densities are computationally more demanding by themselves, due to the increasing number of plane waves. In consequence very low densities at very high temperatures are nearly impossible to calculate within plane wave FT-DFT-MD simulations. These difficulties can be alleviated a little by a reduced particle number, but only to some extend.

Apart from these more technical problems, special care has to be taken at conditions where solid structures might appear, since the solid structure of helium has of course a direct influence on the EOS data. Because the high pressure solid phases of helium are still unknown, it was assumed for the calculations at temperatures below the melting line that it is in the fcc structure, however, test calculations with hcp and bcc lattices were performed. While the energies from the fcc and hcp structures were always very close to each other, these test calculations indicated a possible transition from hcp/fcc to bcc at very high pressures of more than 100 Mbar. At first sight it is strange that the structure should change from a closed-packed one to a less dense system

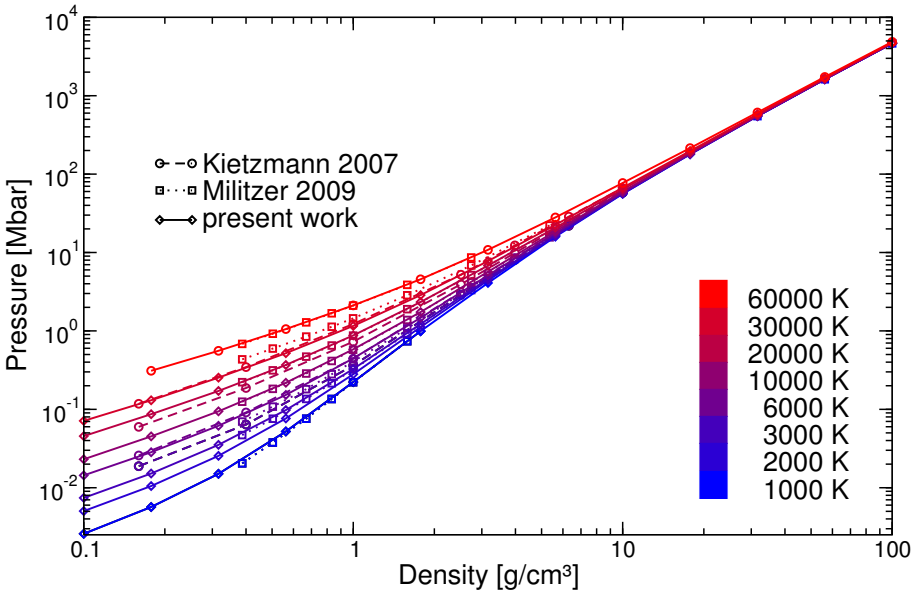

Figure 7.1.: Pressure isotherms of the calculated helium EOS (solid lines with diamonds) from 1000 K (blue) to 60000 K (red) in comparison with the one from Kietzmann *et al.*[61] (dashed lines with circles) and Militzer[27] (dotted lines with squares).

at high densities. An explanation would be the metallization of helium at these high pressures. In that case, the localized electrons at the helium ions which are causing the repulsion between the helium atoms would change to a metallic-like delocalized state. The helium ions in turn would need less space and might turn into a less dense structure. Certainly a more quantitative analysis of the solid phase diagram with the help of free energy methods and electrical conductivity calculations is needed, which is difficult at these extreme conditions and remains for future work.

7.2. Results for the equation of state

The resulting EOS is shown in figure 7.1 for pressure isotherms between 1000 and 60000 K, and densities between 0.1 and 100 g/cm^3, together with the earlier EOS data by Kietzmann *et al.*[61] and the results by Militzer.[27] For temperatures of $T \leq 10000$ K all results are calculated with 108 atoms, while for higher temperatures and low densities 32 atoms are used. This is due to the increasing computational demand for high temperatures and low densities. However, especially for these conditions lower particle numbers are sufficient for accurate results; the deviations between both particle numbers are below 1.0%. For a quantitative comparison of the available EOS data the results were interpolated with the software matti[208] to obtain isotherms for the same temperatures as in Kietzmann *et al.*[61] and Militzer.[27] For these isotherms the pressure deviations $\frac{P-P_{\mathrm{WL}}}{P_{\mathrm{WL}}}$ were calculated and are shown in figure 7.2. As can be seen from this comparison, the deviations can amount up to 10%, especially for low densities and temperatures. The differences between the

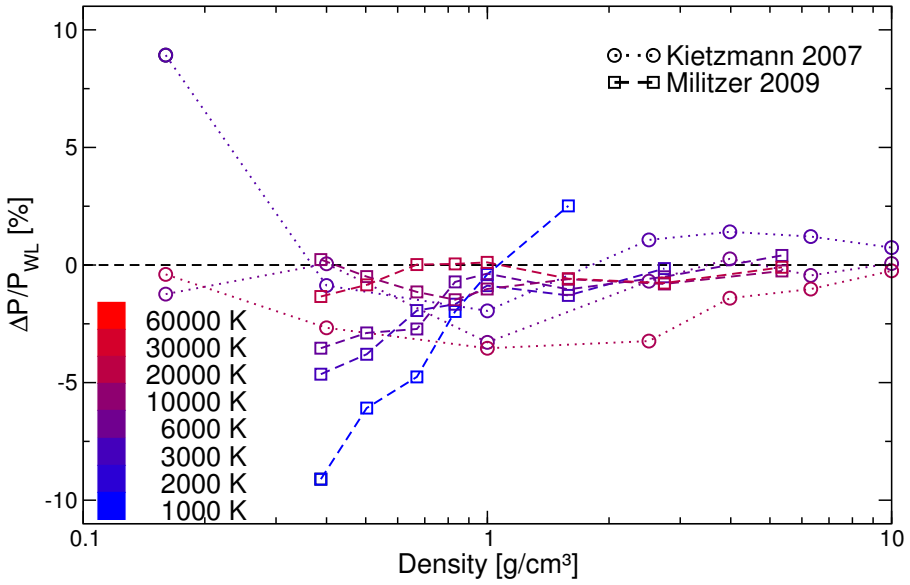

Figure 7.2.: Deviation between the pressures from the EOS data of Kietzmann *et al.*[61] (circles and dotted lines) and Militzer[27] (squares and dashed lines) and the EOS data from this work.

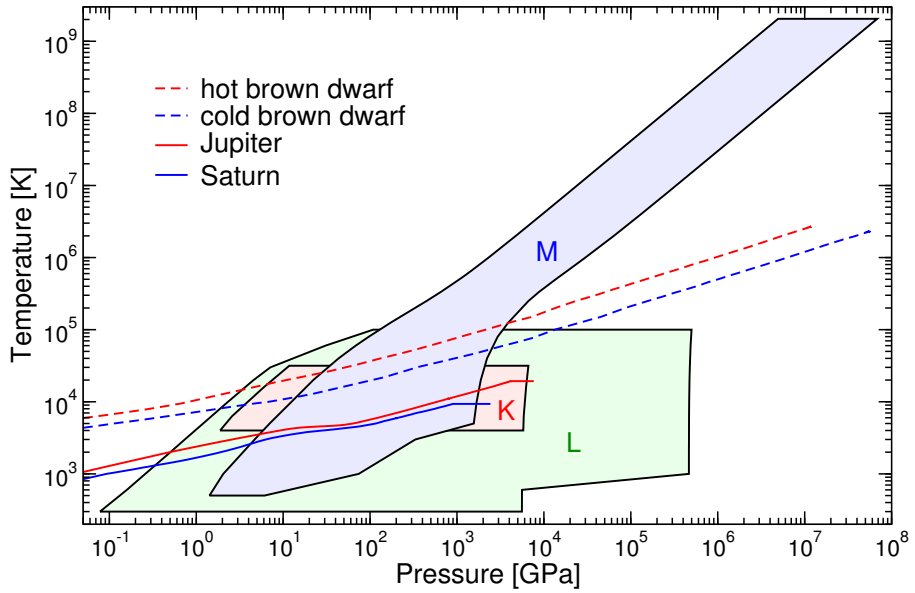

Figure 7.3.: Pressure-temperature coverage of *ab initio* EOS data by Kietzmann *et al.*[61] (red area, "K"), Militzer[27] (blue area, "M"), and the current work (green area, "L"). For comparison isentropes of brown dwarfs,[205] Jupiter,[206] and Saturn[207] are shown, which are the main application of the current EOS data.

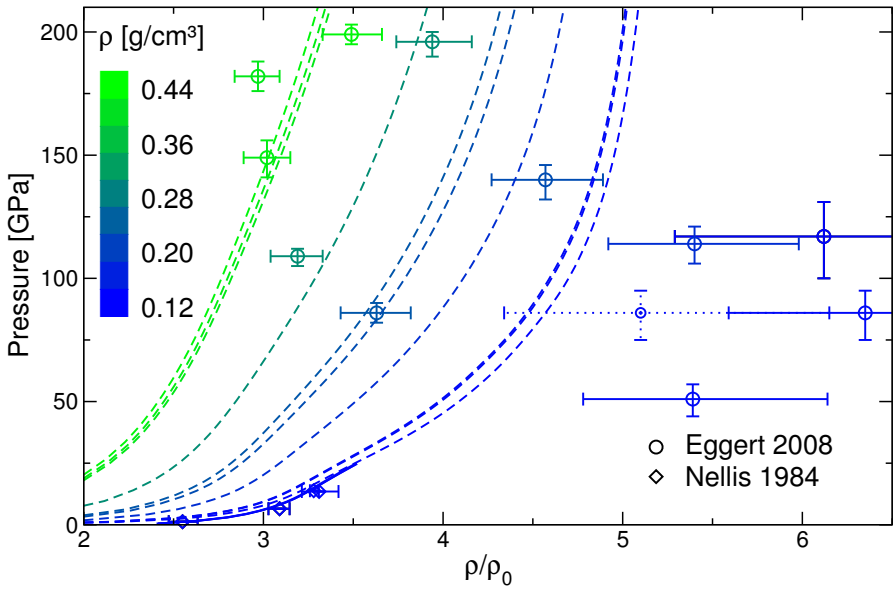

Figure 7.4.: Hugoniots of helium. Experimental data by Nellis *et al.*[59] (diamonds) and Eggert *et al.*[46] (circles) and the corresponding theoretical Hugoniot relations from this work (solid and dashed lines, respectively). The colors indicate the initial density from 0.122 g/cm^3 (blue) to 0.429 g/cm^3 (green). The dotted point indicates as an example the correction for the quartz standard,[209] a similar shift can be expected for the other results by Eggert *et al.*[46] as well.

new results and the ones by Kietzmann *et al.*[61] are probably due to a better convergence of the simulations. Although the here used particle number for the low temperatures is higher than in Ref. 27 (64 atoms), this should not be the sole reason for the deviations. Since two different codes were used in the work of Militzer[27] (VASP with PAW, and CPMD with Troullier-Martins norm-conserving pseudopotentials) it is unclear if this can explain the deviations. One possible reason could be the Γ point used in Ref. 27. At least for 32 atoms the results obtained with the Γ point can deviate up to 8% from a better **k**-point sampling (see section A.1.2).

The coverage of all EOS data is shown in figure 7.3 in comparison with isentropes of different astrophysical objects. Since these are the main applications of the provided EOS, coverage of the thermodynamic conditions along most of the isentropes is desirable. This comparison shows that the current EOS data has the widest coverage so far, however, for the outer regions of Saturn and Jupiter and both the outer and inner regions of brown dwarfs different EOS models are necessary.

7.3. Comparison with experimental data

There are two distinct sets of shock wave experiments to date. The first one by Nellis *et al.*[59] starts with cryogenic liquid helium and uses a gas-gun to shock the material. The second set of

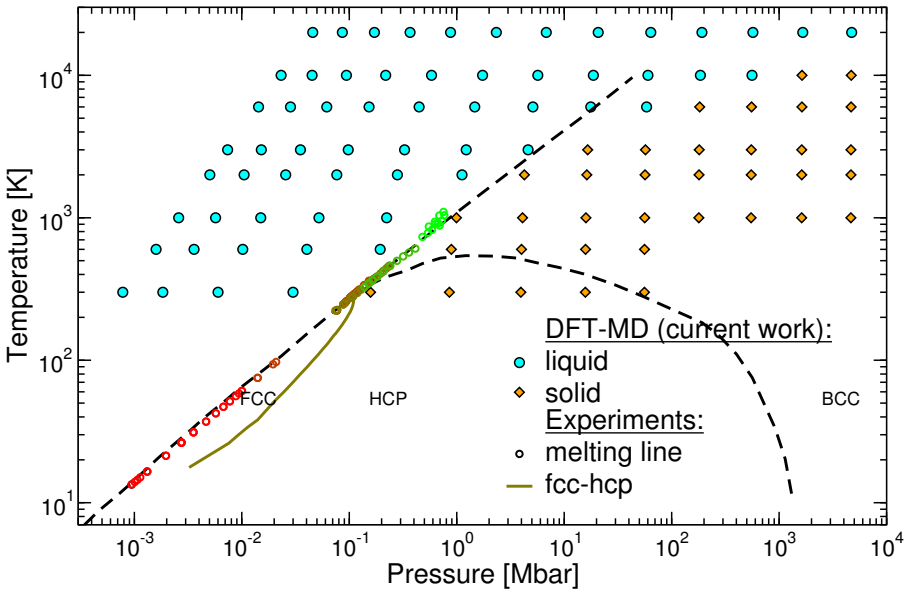

Figure 7.5.: Calculated phase diagram of helium together with the same experimental melting data as in figure 1.3. The experimental transition line from fcc to hcp is taken from Ref. 83. The dashed lines are the proposed *hypothetical* phase diagram by Loubeyre.[210]

experiments by Eggert *et al.*[46] starts with precompressed helium at room temperature and the shock wave is driven by a high-power laser. Because the Hugoniot depends heavily on the starting condition, the Hugoniot relations for all of the individual starting points were evaluated. In order to obtain smooth curves, additional isotherms were interpolated from the original calculated EOS data. The results are shown in figure 7.4 together with the experimental data. While the results agree very well with the gas-gun data, considerable deviations can be observed for the laser data at low precompression. However, since the realization of the laser experiments, the used quartz-standard has been questioned, and it was estimated that instead of the reported maximum compression of 6.3 in fact only a compression of 5.1 was reached.[209] This revised data point is also shown in figure 7.4. Later on Celliers *et al.*[120] estimated that *on average* the compression ratio might be about 10% less then reported previously. Keeping these uncertainties in mind, also the data for the laser experiments might agree with the calculated Hugoniots. This has to be checked in the future by reanalyzing the experimental data, as it was already done for hydrogen.[209]

7.4. Phase diagram

It was assumed for all EOS calculations that the solid structure is fcc. Under this assumption, an approximated high pressure melting line can be obtained, just by observing if the system melts or not. For this purpose, all calculations near or below the expected melting line were started in the fcc structure. At high temperatures above about 10000 K, the simulations were heated starting

from lower temperatures to prevent an accidental melting due to the velocity initialization. At the final temperature, the RDFs and diffusion coefficients[211;212] were analyzed over a few thousand timesteps to determine if the crystal structure is stable or melts. The results for all EOS data points up to 20000 K and additional 300 and 600 K data is shown in figure 7.5 together with the experimental melting data[38;65;73–76] and the proposed phase diagram by Loubeyre.[210] This extends the previous results from Paper I to a wider pressure and temperature range.

One problem of this approach is the assumed fcc structure of the solid, which is probably realistic at pressures up to some 10 Mbar. While the experiments in this region indicate an hcp structure, the results obtained with the very similar fcc structure can be expected to differ only little. However, at higher pressures a transition to a bcc structure was proposed,[77] which is connected to the metallization of helium, in accordance with the solid structure of a one-component plasma being bcc.[213] As a consequence, the melting line at very high pressures might be different from the results obtained here. Apart from these fundamental uncertainties, also some technical problems remain. In every finite size simulation for melting and freezing by heating and cooling, respectively, the system will experience a hysteresis for the melting temperature, especially when the particle number is low. Since here only melting was simulated, the obtained temperatures are likely too high. However, a very accurate calculation of the melting line and high pressure phases was not the aim of this study. Still, the results are in good agreement with the available experimental data, and are, to the best of my knowledge, the only *ab initio* data for the high pressure phase diagram of helium to date.

8. Hydrogen-helium mixtures

8.1. Equation of state

All planetary models so far rely on the linear mixing approximation for the EOS of hydrogen, helium, and heavier elements, also known as the additive volume rule.[138;206;214] Within this approximation the density ρ_x of a hydrogen-helium mixture with the helium mass fraction x_M at a given temperature and pressure can be calculated as

$$\frac{1}{\rho_x} = \frac{x_M}{\rho_{\mathrm{He}}} + \frac{1 - x_M}{\rho_{\mathrm{H}}}, \tag{8.1}$$

where ρ_{H} and ρ_{He} are the densities of pure hydrogen and helium at these temperatures and pressures, respectively. While all the individual EOS data has seen much progress in recent years, the influence of a real mixture EOS for planetary models is still missing. However, first attempts to assess the accuracy of the linear mixture EOS data compared to a real mixture EOS have been

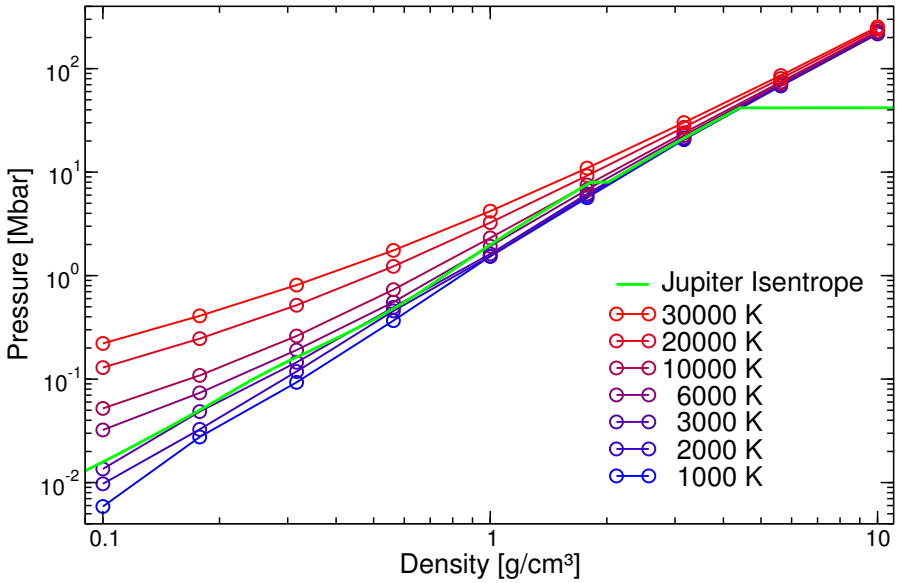

Figure 8.1.: Pressure isotherms of the calculated mixture EOS from 1000 K (blue) to 30000 K (red) for a helium fraction $x = 0.086$. For comparison the Jovian isentrope[206] is shown (green line).

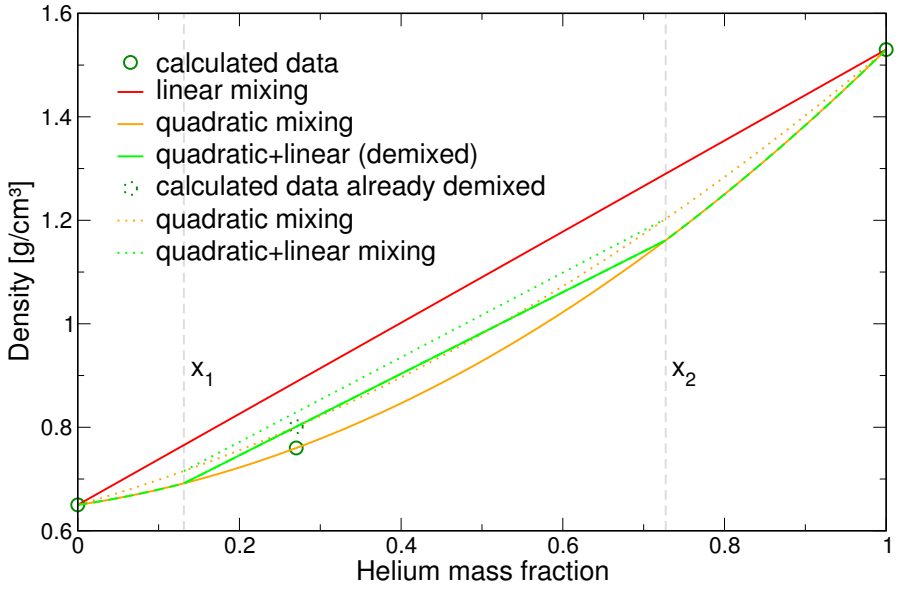

Figure 8.2.: Schematic overview of the mixing rules with and without demixing for approximately 1 Mbar and 5000 K. The linear mixing (equation 8.1, solid red line) interpolates between both pure systems. The quadratic mixing (equation 8.2, orange line) takes the additional calculated mixture data into account. If demixing occurs, the phases x_1 and x_2 have to be mixed linearly (dashed and solid green line). If the calculated data already contains demixing effects (dotted circle), this approach overestimates the effect (dotted lines).

made,[112;215] showing up to 10% deviations for a mixture of $x = 1/3$. Therefore, one important goal is the calculation of a hydrogen-helium mixture EOS, which can be used as an input for planetary models. First results for such an EOS for a helium fraction of $x \approx 0.086$ (the mean helium fraction of Jupiter and Saturn) are shown in figure 8.1, in comparison with the Jovian isentrope. These calculations were performed with "only" 74 hydrogen and 7 helium atoms and are only a first step in that sense. A more detailed study of the deviations to the linear mixing approximation is still missing and should be based on EOS data on the same level of accuracy. To use this additional input for planetary models with varying helium fractions, the quadratic mixing rule

$$\frac{1}{\rho_x} = \left[\frac{x_M^2 - x_M x_{\mathrm{HHe}}}{1 - x_{\mathrm{HHe}}}\right]\frac{1}{\rho_{\mathrm{He}}} - \left[\frac{x_M^2 - x_M}{x_{\mathrm{HHe}}^2 - x_{\mathrm{HHe}}}\right]\frac{1}{\rho_{\mathrm{HHe}}} + \left[\frac{x_M^2 - x_M(1 + x_{\mathrm{HHe}}) + x_{\mathrm{HHe}}}{x_{\mathrm{HHe}}}\right]\frac{1}{\rho_{\mathrm{H}}} \quad (8.2)$$

can be used instead of the linear one, where ρ_{HHe} is the density of the additional calculated mixture EOS with the helium mass fraction x_{HHe}. Both mixing rules (linear and quadratic) are shown in figure 8.2 (solid red and orange lines, respectively). Special care has to be taken when the temperature

and pressure are inside the demixing region. In this case, the system consists of a linear mixture of two phases with different helium fractions. Therefore, the two contributing EOS with these helium fractions have to be calculated by the quadratic mixing rule (dashed green lines in figure 8.2), which then have to be evaluated with the linear mixing rule (solid green line). However, if the calculated mixture EOS already contains demixing inside the simulations, the resulting density should already be on that line, and a subsequent quadratic and linear mixing would lead to a double counting of the demixing effects (green dotted line). In that case better results might be obtained by just using the quadratic mixing rule (orange dotted line). This has to be studied in more detail in the future and a reliable method of mixing has to be developed.

8.2. Complete miscibility gap

Since Paper I and Paper III contain only parts of the miscibility gap, the complete miscibility gap with all available data is shown in figure 8.3. As a very crude estimation for the liquidus line, a linear interpolation between the (estimated) melting temperatures of hydrogen and helium are used. An accurate calculation for the helium rich phase diagram at low temperatures would be very interesting, but also very complicated and not necessary for planetary applications.

As stated in Paper I, the abrupt increase of the demixing temperature at high helium fractions happens at a constant hydrogen partial density, which coincides with the Mott density of $a_0 n_H^{1/3} \approx 0.25$, where a_0 is the Bohr radius. This is illustrated in figure 8.4, where this quantity is shown for all considered pressures as a function of the helium fraction x. At each "critical" helium fraction, i.e. the helium fraction where the demixing temperature increases, the value corresponds to the Mott-criterion.[97] However, since especially for high helium fractions the errors of the ideal entropy of mixing might be large,[202] it remains to be seen if this effect persists also with a more accurate method.

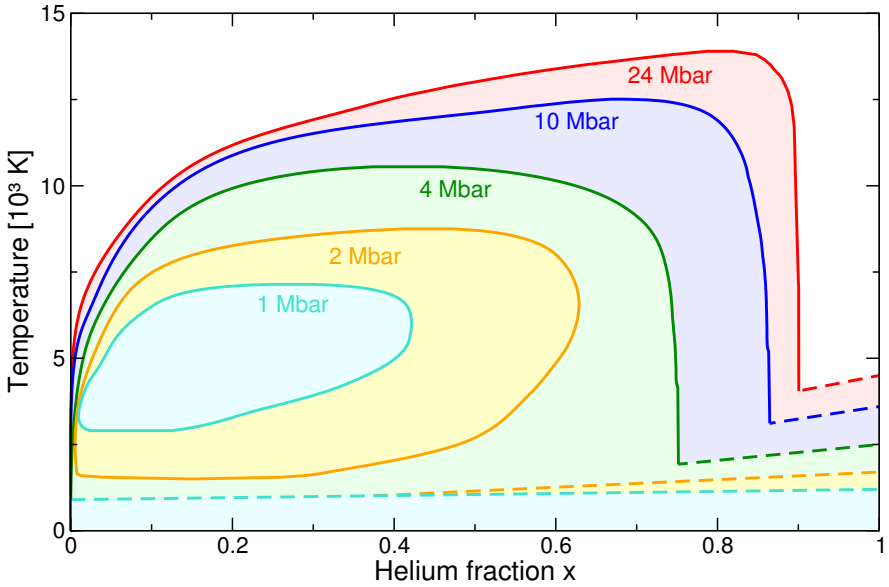

Figure 8.3.: Complete miscibility gap of hydrogen and helium (solid lines). The dashed lines indicate a possible liquidus line.

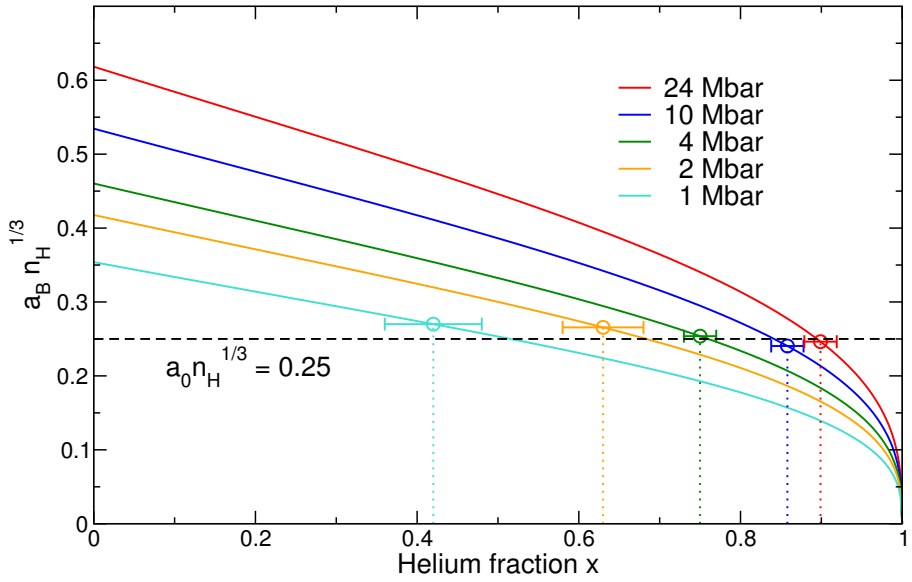

Figure 8.4.: Mott density of the hydrogen subsystem for all considered pressures (solid lines). The temperatures were chosen so that the critical helium fractions (circles with dotted lines) could be determined easily (around 5000 K), however, the lines are only very weakly temperature dependent. The errorbars are the estimated uncertainty in determining the critical helium fraction.

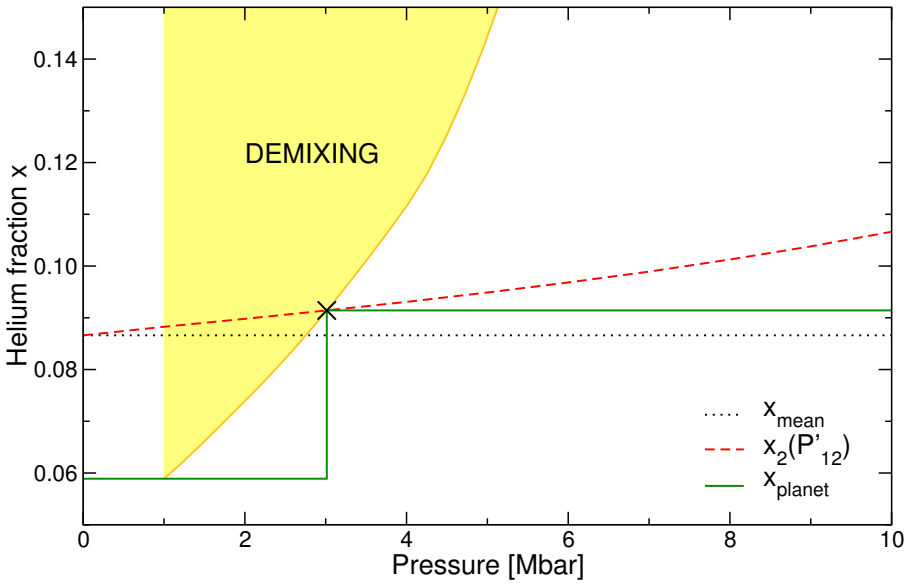

Figure 8.5.: Construction of a thermodynamic stable planet, where demixing has just started, for the example of Jupiter. The transition pressure is obtained by the intersection of the lower end of the demixing region (orange line) and the inner helium fraction $x_2(P_{12})$ (dashed red line).

8.3. Consequences for Jupiter and Saturn

As was already shown in Paper I and Paper III, the miscibilty gap will have a considerable influence on the interior structure and evolution of Jupiter and Saturn. Therefore, a way to construct a thermodynamic stable interior structure model is important, especially for the evolution of Saturn.[216]

Here, the schematic construction of thermodynamic stable structure models will be discussed for the example of a warm giant planet (current Jupiter or former Saturn), where demixing has just begun, and a cold planet (current Saturn) which is deep inside the demixing region. Qualitatively this was already discussed by Stevenson and Salpeter[128] for different possible demixing scenarios, whereas the discussion here is (although still schematic) based on the new calculated miscibility data and current isentropes of Jupiter and Saturn. For simplicity, the heavier elements are left out of the discussion, but for real applications a reasonable treatment of these constituents has to be applied.

Under the assumption that the demixing and rain-out of helium is fast compared to the evolution time scales, at each timestep in the evolution, no part of the interior structure model should be inside the demixing region. Since all planets cool down during their evolution, at some point the planetary isentrope should enter the demixing region, which is schematically illustrated for the Jupiter case in figure 8.5. For each pressure-temperature point on the planetary isentrope the two corresponding stable helium fractions have to be derived from the miscibility gap, and no part of the planetary interior should enter the region between these two lines (yellow area in figures 8.5 and 8.6). As

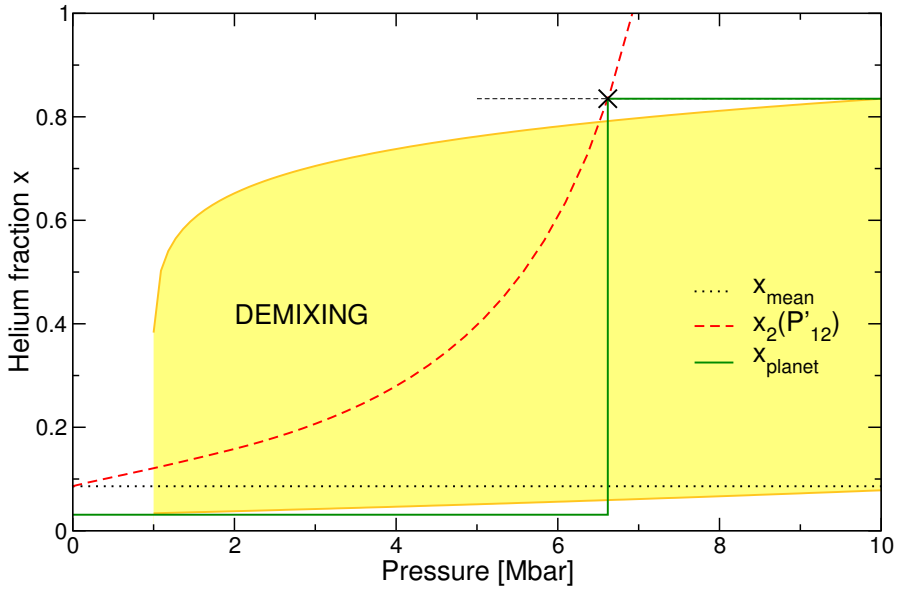

Figure 8.6.: Construction of a stable planet deep inside the demixing region (Saturn). P_{12} is obtained by the intersection of the maximum of the demixing region (dashed black line) and $x_2(P_{12})$ (dashed red line).

can be seen, the mean helium fraction violates this requirement. Therefore, the helium fraction in the outer layer has to be equal to the minimum of the demixing area. The second input parameter, the transition pressure P_{12}, can be obtained by extracting the inner helium fraction x_2 for different assumed P'_{12}. The intersection of this function $x_2(P'_{12})$ and the lower end of the demixing region yields the correct transition pressure.

When the planet cools further, the demixing region grows and at some point no intersection can be found, which is the case for todays Saturn, see the schematic plot in figure 8.6. In this case, the intersection between $x_2(P'_{12})$ and the maximum of the demixing region defines the transition pressure P_{12}.

In contrast to the discussion by Stevenson and Salpeter[128] which allowed for inhomogeneous layers, the three-layer structure is enforced here. While this approach ensures thermodynamic stability, the enforcement of two homogeneous fluid layers might overestimate the demixing effect, since helium fractions nearer to the mean helium fraction would still be stable in the inner region of the planet. In reality, this effect might be alleviated by the convection in both layers, leading again to homogeneous layers. Still, an interior structure model which allows for helium gradients might be necessary to asses the importance of this effect.

After this scheme is employed to derive the outer helium fraction and the transition pressure, the new calculated isentrope has to be compared with the miscibility gap, to derive an updated demixing region. This process has to be iterated, until the results are converged. Therefore, it is advantageous for planetary evolution calculations to start with the values from the previous timestep, and not with the mean helium fraction. The application of this procedure both with homogeneous and

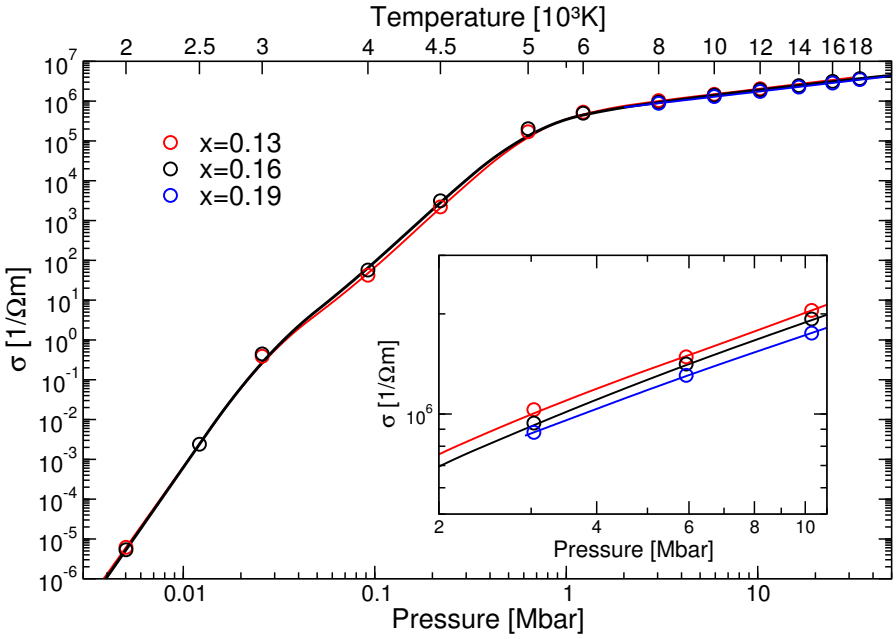

Figure 8.7.: Electrical conductivity (circles) along Jupiter's isentrope for the three relevant helium fractions, mean helium fraction (black), outer helium fraction (red), and inner helium fraction (blue). The lines are guide to the eye. The inset shows the same data near the commonly used transition pressures P_{12}.

inhomogeneous layers is already in progress.

8.4. Conductivity in Jupiter

Apart from the interior structure models, which need an accurate EOS as input, dynamo simulations for the magnetic field are of great importance, since these fields are measured and can give valuable additional information,[217;218] thereby providing a possible check for the interior structure model.[219–221] These dynamo simulations need further material data such as the electrical and thermal conductivity.[222] Therefore, these quantities were derived along the Jupiter isentrope for the mean helium fraction, as well as the (smaller) outer helium fraction x_1 and the (higher) inner helium fraction x_2. Because the simulations contain only hydrogen and helium and not the full planetary mixture as used in the models, and the limited particle number cannot reproduce the exact helium fractions, "along the isentrope" is defined as having the same pressure and temperature as the isentrope. The influence of heavier elements on the conductivity should be small, since they only amount to few percent. However, it is not possible with VASP to adjust the pressure of the simulation, but only the density. Therefore, two simulations with resulting pressures near the Jovian pressure were performed at each considered temperature. From these two simulations 20 snapshots each were taken to calculate the electrical conductivity σ and the thermal conductivity λ. Together with the pressure of each snapshot, this results in $\sigma(P)$ and $\lambda(P)$. Then a linear fit is

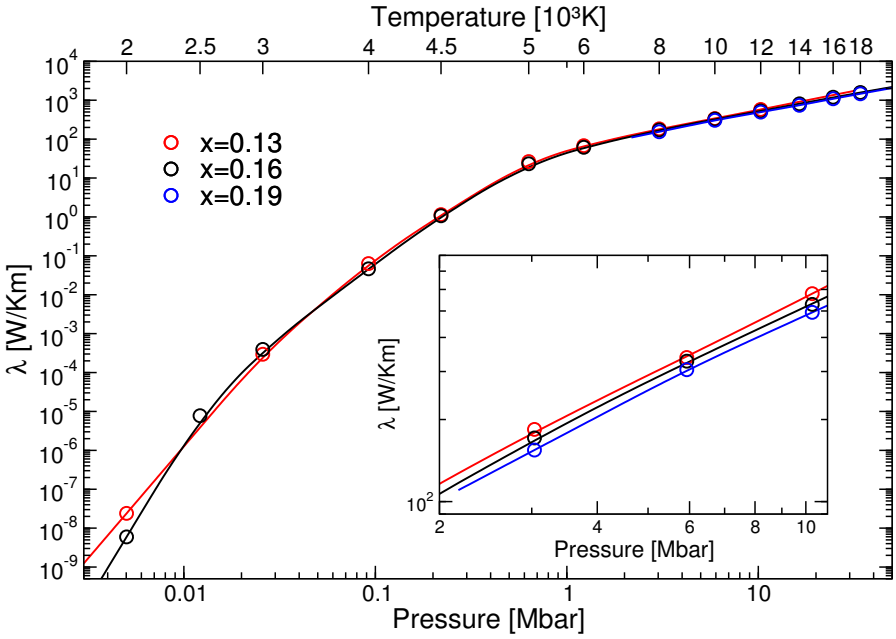

Figure 8.8.: Electronic contribution to the thermal conductivity (circles) along Jupiter's isentrope.

applied to extract the conductivity data at the designated pressure. The linear fit is possible because the pressure region is very small (usually within few percent of this pressure) and the exact functional dependence is not necessary. A simple average of all conductivity data would yield very similar results, but might be less accurate, if one simulation is very near the designated pressure, while the other is further away.

All calculations were performed with 256 electrons, resulting in $N_H = 216$ and $N_{He} = 20$ for the mean helium fraction ($x = 0.085$), $N_H = 222$ and $N_{He} = 17$ for the outer helium fraction ($x_1 = 0.071$), and $N_H = 208$ and $N_{He} = 24$ for the inner helium fraction ($x_2 = 0.103$). Converged results were obtained with the standard H and He PAW potentials and a plane wave cutoff of 800 eV (see also section A). The MD simulations were performed with the BMVP, while a $4 \times 4 \times 4$ **k**-point set was used for the conductivity calculations. The results are shown in figures 8.7 and 8.8 and are published in Ref. 201. Note that the shown thermal conductivity is only the *electronic* contribution, and for low pressures the ionic thermal conductivity will dominate. Both the electrical and the thermal conductivity increase over more than ten orders of magnitude in the outer region, i.e. at pressures below $\sim$ 1 Mbar, where hydrogen is molecular.[16;110] At higher pressures, i.e. deeper inside the planet, hydrogen is mostly dissociated and has metallic-like conductivities, which are still increasing, but not as steep as before. Compared to these dramatic changes in conductivity, the influence of different helium fractions inside of Jupiter are very small. At high pressures, more helium reduces systematically the electrical and thermal conductivity, as expected. However, this behavior is not as clear for the low pressure molecular phase. Partly, this might be due to the difficult evaluation of the conductivity at these conditions, and could therefore be improved by even more snapshots. Another explanation might be the varying influence of the helium amounts on the EOS data especially in the transition region between molecular and atomic

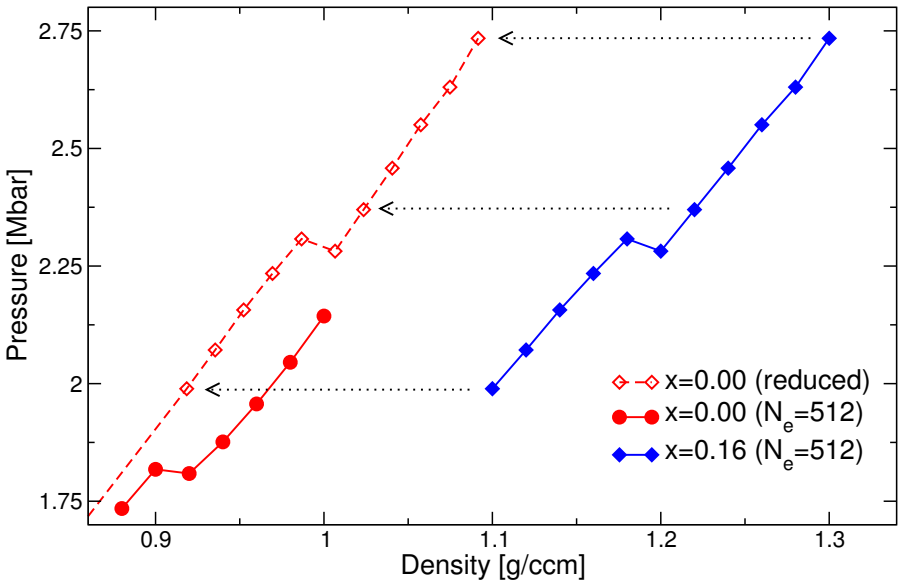

Figure 8.9.: Pressure isotherms of hydrogen (red) and a hydrogen-helium mixture ($x = 0.16$, blue) at 1000 K (filled symbols). The pressure isotherm of the reduced hydrogen subsystem is indicated by the open symbols, see text.

hydrogen, which in turn would lead to different densities of the hydrogen subsystem. Both effects should be studied for more accurate results, but since the overall influence is small, this is not necessary for the purpose of this work.

8.5. First-order phase transition

The occurrence of a first-order liquid-liquid phase transition from a nonmetallic molecular to a metallic atomic phase in pure hydrogen leads directly to the question what influence the addition of helium has on this transition.[223] First calculations for this problem indicated a stabilization of the hydrogen molecules due to the admixture of helium,[112] however, the first-order phase transition was still uncertain at that time. To check the persistence of the transition, first calculations with 512 electrons were performed for the mean helium fraction of Jupiter, the same as for the conductivity calculations. The results for the 1000 K isotherm are shown in figure 8.9, together with the 1000 K isotherm of pure hydrogen for comparison. A first-order transition can be observed also from these calculations, but, while the pressure in general gets lower with the addition of helium, the transition pressure gets shifted upwards. Because helium should undergo very little change at these moderate conditions, it can be expected that the biggest effect of helium is due to the consumed volume. Under this assumption, the reduced density of the hydrogen subsystem can be calculated by the

linear mixing approximation as

$$\frac{1 - x_M}{\rho_{\mathrm{H}}} = \frac{1}{\rho} - \frac{x_M}{\rho_{\mathrm{He}}}, \tag{8.3}$$

where ρ_{He} can be extracted from the calculated helium EOS (chapter 7). The resulting shifted isotherm is also shown in figure 8.9 and confirms that the assumption is valid within $\sim$ 5% in pressure. The main deviation remains the shifted transition pressure, which is in accordance with the results of Vorberger *et al.*[112], i.e. the additional helium stabilizes the hydrogen molecules.

A similar structure analysis as in Paper III (chapter 5), i.e. RDF calculation and droplet search, shows again the metallization of hydrogen as the driving force behind the demixing, because all simulations above the phase transition show direct evidence of demixing. This makes the topic of non-congruent phase transitions even more relevant, since demixing, i.e. two phases with different helium fractions would be a consequence of a non-congruent phase transition.[223] However, the limited particle number cannot quantitatively evaluate the thermodynamic effects of non-congruency and a more detailed study of this phenomenon remains for future work. A very fascinating question is the effect of helium on the critical point, because this effect is dramatic for the comparable system Hg-He.[224]

Part IV.

Conclusion

9. Summary

In this work, the properties of hydrogen, helium, and their mixture at extreme conditions as relevant for giant planets have been studied with an up-to-date *ab initio* method. Special attention has been paid to phase transitions that occur at these high pressures. For hydrogen, this is the first-order liquid-liquid phase transition, which has already been discussed for several decades as the *plasma phase transition*. Here, conclusive theoretical evidence for this first-order transition is obtained with FT-DFT-MD simulations, independently confirming the results of another group, which have been obtained in parallel.

This nonmetal-to-metal transition has a huge impact on the behavior of hydrogen-helium mixtures, namely the phase separation of hydrogen and helium. This miscibility gap has been calculated accurately, and for the first time, the results have the potential to solve several questions regarding the interior structure and evolution of Jupiter and Saturn. Until now the distribution of helium inside the planets, specifically the lower (measured) helium content in the atmosphere of Saturn compared to Jupiter and the solar value, and the excess luminosity of Saturn have been without a proven explanation.

Additionally, a first step towards a real mixture EOS has been made, which can be used instead of the linear mixing approximation in the future. For this mixture, the first-order nonmetal-to-metal transition has also been studied, and its existence could be shown.

The electrical and thermal conductivity along the Jupiter isentrope have been calculated to eliminate the so far great uncertainties of this input data for dynamo simulations for the magnetic field of giant planets.

For helium, an extended *ab initio* EOS data set has been calculated, which has the widest coverage of astrophysical objects such as giant planets and brown dwarfs so far. This EOS data was compared to experiments with promising results. From these calculations, first results for an *ab initio* high pressure phase diagram has been obtained, which is in agreement with available experimental data at megabar pressure.

10. Outlook

There are many fascinating developments which can be expected in the future. The biggest question for hydrogen is, of course, if and when the first-order phase transition in the liquid can be confirmed experimentally and by which method. At the moment, static DAC experiments at low temperatures are limited to solid hydrogen, while dynamic shock wave experiments reach high temperatures too fast; their results are beyond the critical point of this transition. But advancements have been reported for both methods recently,[34;108] and although both experiments are inconclusive at the moment,[116] they are a step in the right direction. While all recent *ab initio* results show qualitatively similar results, an accurate quantitative calculation of the coexistence line and its critical point with either CEIMC or HSE-DFT will help in designing future experiments.

For hydrogen-helium mixtures, a great step forward would be an experimental verification of phase separation at high pressures. Recently, some possible paths to reach this aim have been proposed, for example by measuring the dynamic electrical conductivity[225] or by employing X-ray Thomson scattering techniques.[226] A very accurate and extensive data set of the miscibilty gap is needed for interior structure models of giant planets. While the results in this work provide the extensive data set, they rely on the ideal entropy of mixing approximation. This approximation has been circumvented by using thermodynamic integration.[202] However, due to the additional demand of this method, some accuracy is lost for the double tangent construction, and the data set is not as extensive. Therefore, further work is necessary, especially to decide if Jupiter is inside the demixing region or not.

Recently, reflectivity measurements for helium with precompressed Hugoniot experiments have been published.[46;120] Theoretical studies are already available for these Hugoniots,[27] and results are also part of this work. Both theoretical results show lower compression ratios than the measured ones. A plausible explanation has been given by Knudson and Desjarlais,[209] who could show that the used quartz standard was inadequate. Therefore, the results should be reanalyzed in more detail, and calculations for the electrical conductivity and optical reflectivity along those Hugoniots should be performed in the future.

Part V.

Appendix

A. Convergence

For all numerical simulations, it is necessary to perform convergence tests with respect to a variety of parameters, FT-DFT-MD is no exception. These parameters include the plane wave cutoff E_{cutoff}, the radial PAW cutoff r_c, finite size effects like the **k**-point sampling and the particle number, and, especially for high temperatures, the number of bands for the FT-DFT calculations. For the MD simulations the size of the timestep has to be checked, and again the convergence with respect to finite size effects is of importance.

In general, it is possible to perform the convergence tests with respect to the electronic structure calculations independently from the convergence with respect to the MD simulations (i.e. first converge the electronic structure with static calculations and after that converge the MD simulations). However, this is not the case in the vicinity of phase transitions, especially when they are driven by changes in the electronic structure, like e.g. the PPT, see figure A.12 in section A.2 and Paper II.

Typically, all convergence tests are performed in a similar way. The parameter of interest will be varied from “light“ and computationally easy settings, to ”tight“ and demanding settings, while all other parameters stay fixed either at already reasonably converged settings (if known) or also at tight settings. Then, the quantities of interest will be evaluated in dependence on this parameter and their deviation to the best value has to be analyzed. Since the main results of all the simulations are the EOS data, the pressure and the internal energy are of main interest. Because the pressure has well defined absolute values, the *relative* deviation between the pressure P_{current} at the current setting and the pressure P at the best setting can be studied, i.e. $\frac{\Delta P}{P} = \frac{P_{\text{current}} - P}{P}$. Usually, a value of better than 1% is desirable. However, this quantity is meaningless for the energy, since it has no absolute defined value and can be shifted by an arbitrary constant. Therefore, only the *absolute* deviation $\Delta U = U_{\text{current}} - U$ can be analyzed. A convergence of better than few meV/atom is aimed at for most of the calculations. However, this is not always possible for very high densities as considered for helium. To assess the quality of the calculations in these regions, the energy deviations are compared to a reference energy, which is calculated from the (ideal) relation $PV = 2/3U_{\text{ref}}$. Then a relative convergence $\frac{\Delta U}{U} = \frac{\Delta U}{U_{\text{ref}}}$ can be quantified which should be better than 1%.

Since MD simulations are performed, the forces on the ions have to be known accurately. Although their convergence is usually similar to the pressure convergence, it should be checked explicitly. Since it can always occur that the force components on some ions are nearly zero, their relative deviations $\frac{\Delta F}{F} = \frac{F_{\text{current}} - F}{F}$would be nearly arbitrary. Therefore, only the force components with an absolute value ≥ 0.05 eV/Å are taken into account.

In section A.1, the convergence of the pressure, energy, and the forces with respect to all important parameters for static DFT calculations is analyzed. The convergence of the MD simulations is shown in section A.2, and section A.3 deals with the convergence of the electrical and thermal conductivity.

A.1. Convergence of the electronic structure calculations

A.1.1. Plane wave cutoff and PAW cutoff

The convergence with respect to the plane wave and PAW cutoff should be independent from finite size effects, i.e. from particle number and **k**-point sampling, if the particle number is high enough to represent the physical system at all. Therefore, a rather small system size of 64 and 32 atoms for hydrogen and helium, respectively, was chosen. This system size is usually big enough for simple EOS calculations, while its electronic structure can be calculated easily with very high precision. Since the required plane wave cutoff is directly dependent on the radial PAW cutoff, these convergence tests were performed for all available PAW cutoffs. For each density and temperature condition, a MD simulation was performed with reasonable plane wave and PAW cutoffs, which has to be checked again afterwards. Then, snapshots of these simulations were used for static calculations with varying cutoffs.

For hydrogen, the standard "H" potential with a PAW cutoff $r_c \approx 0.52$ Å and the harder "H_h" potential with $r_c \approx 0.43$ Å were considered. The snapshots were calculated with plane wave cutoffs between 100 and 2000 eV for both potentials. The result with 2000 eV was taken as the correct reference value. The outcome for the pressure, the energy, and the forces are shown in figures A.1, A.2, and A.3 for a temperature of 1000 K and densities between 0.4 and 4 g/cm^3. The results for 10000 K are not shown, but they are basically identical. For all densities, the pressure is converged to much better than 0.5% for a plane wave cutoff energy of 700 eV with the standard potential, while the harder potential needs a cutoff energy of 1200 eV for a similar convergence. A further increase in the cutoff energy yields almost no improvement in both cases. These plane wave cutoffs lead to an energy convergence of better than 2 meV/atom for all snapshots. The convergence of the forces are shown only for a density of 0.4 g/cm^3, the results for the other conditions are similar. Although the individual force components exhibit some noise, on average they are also converged to much better than 0.5%. Finally, in figure A.4 both PAW cutoffs are compared, where the result with the harder potential is taken as the reference value. For all densities the deviations are below 0.5% at 1000 K, but they begin to increase at high densities. At 10000 K the increase begins earlier, and at 4 g/cm^3 the deviations are nearly 1%. This can be understood from the coordination numbers shown in the inset in figure A.4, which are a measure of how many atoms are on average inside a sphere around an atom with a given radius. At 1000 K almost no atom is inside the PAW sphere of the standard potential, while at 10000 K already a small but significant number of atoms is inside this sphere.

There is only one PAW potential for helium supplied with VASP, which has a cutoff of $r_c \approx 0.52$ Å. Because also results at extreme densities of helium are reported in this work, a full Coulomb potential was used for high densities. Of course, this potential needs much higher plane wave cutoffs. While for the PAW potential again a cutoff of 2000 eV was used as reference, for the Coulomb potential 100000 eV was used if possible. The results are shown in figures A.5 (pressure), A.6 (energy), and A.7 (forces). Again the pressure is converged to much better than 0.5% at a plane wave cutoff of 700 eV. At 1 g/cm^3 the convergence gets worse afterwards, before it reaches very good values again at 1200 eV. This peculiar behavior exists also at the higher densities, but the deviations are much smaller and cannot be seen in this figure. With the Coulomb potential, the pressure converges systematically better with higher densities. For 1 g/cm^3, it is barely possible to

reach convergence of better than few percent, while for 10 g/cm^3, 1% convergence is reached at about 5000 eV and 0.5% is reached at about 8000 eV. For 100 g/cm^3, convergence of better than 0.5% is already reached at 2000 eV. This behavior follows from the fact that electrons should be a homogeneous electron gas in the high density limit, which can be represented easily by plane waves. The energy convergence is a little more involved, but for 1 and 10 g/cm^3, convergence of better than 5 meV/atom is reached at 700 eV with the PAW potential. At 100 g/cm^3 1400 eV is needed for a similar convergence, but there the PAW potential is not applicable anyway. It is nearly impossible to reach a similar *absolute* convergence with the Coulomb potential. Therefore, the energy deviations are compared to the reference energy in this case, as explained in the beginning of this chapter. This *relative* convergence is shown in the inset of figure A.6. There, a convergence of better than 0.5% can be seen for 8000 and 4000 eV at 100 and 10 g/cm^3, respectively. The convergence of the forces (figure A.7) for 1 g/cm^3 at 1000 K is similar to the results for hydrogen, good convergence is reached at a 700 eV plane wave cutoff. In figure A.8, the deviations between the PAW and the Coulomb potential are shown for 1000 and 10000 K. Since it is impossible to reach converged results with the Coulomb potential at low densities, the pressures were extrapolated with a function $P(E_{\text{cutoff}}) = A + \frac{B}{E_{\text{cutoff}}}$ to estimate the converged result. As can be seen, the deviations are below 0.5% at densities up to 10 g/cm^3, but they increase dramatically at higher densities. Again, this behavior can be understood by the coordination numbers in the inset of figure A.8, showing a large amount of atoms inside the PAW sphere.

All published results (chapters 3 to 5) of this work were obtained with the standard PAW potentials with a 1200 eV plane wave cutoff. Since the considered densities are low enough, i.e. smaller than 4 g/cm^3 and 10 g/cm^3 for hydrogen and helium, respectively, this choice is valid. The used plane wave cutoff is more than enough for converged results and was subsequently reduced to 800 eV for the additional results in chapters 6 to 8. For the helium EOS at densities above 10 g/cm^3, the Coulomb potential was used, however, only with a plane wave cutoff of 4000 eV, therefore ”only“ reaching convergence of the pressure to about 1%.

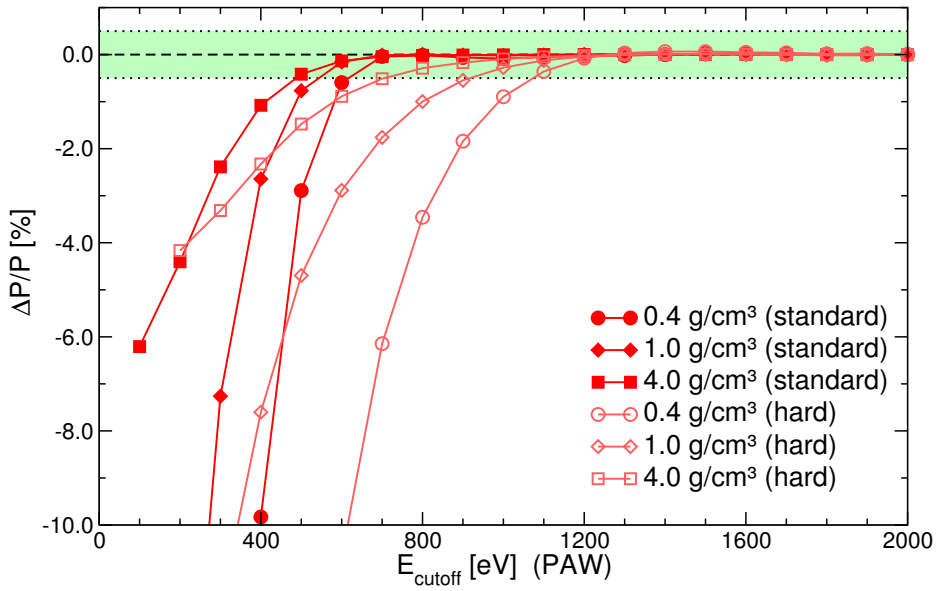

Figure A.1.: Pressure convergence for hydrogen with respect to the plane wave cutoff at 1000 K. Shown are results for the standard PAW (filled symbols) and the hard PAW (open symbols) potentials. The green area indicates convergence of better than 0.5%.

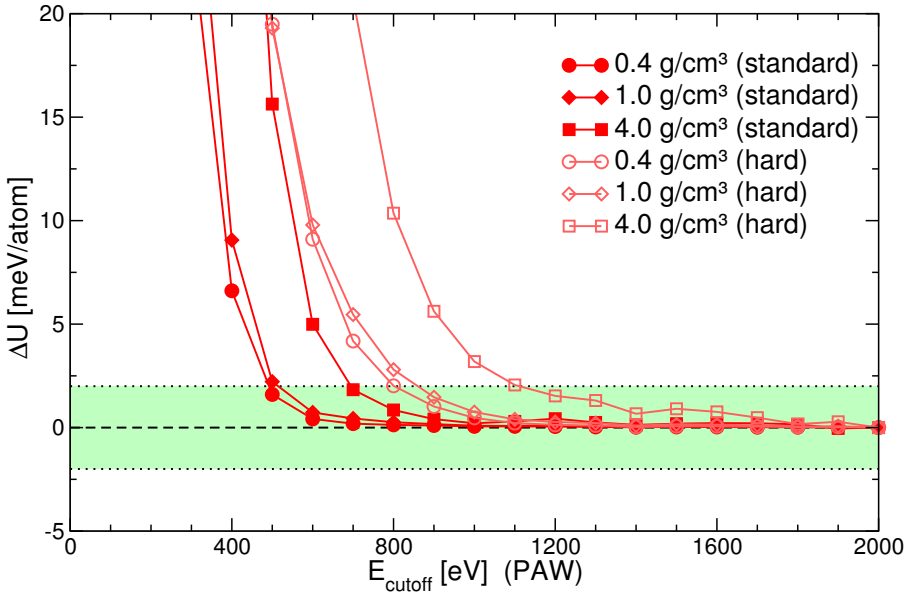

Figure A.2.: Energy convergence for hydrogen for the same parameters. The green area indicates convergence of better than 2 meV/atom.

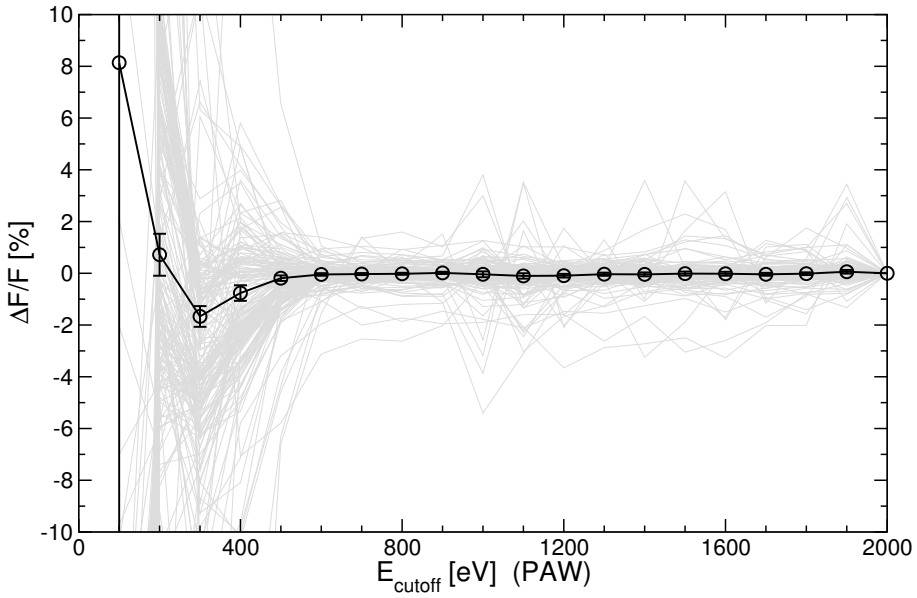

Figure A.3.: Convergence of the force components of all hydrogen ions (gray lines) at 0.4 g/cm^3 and 1000 K. The mean values are shown in black.

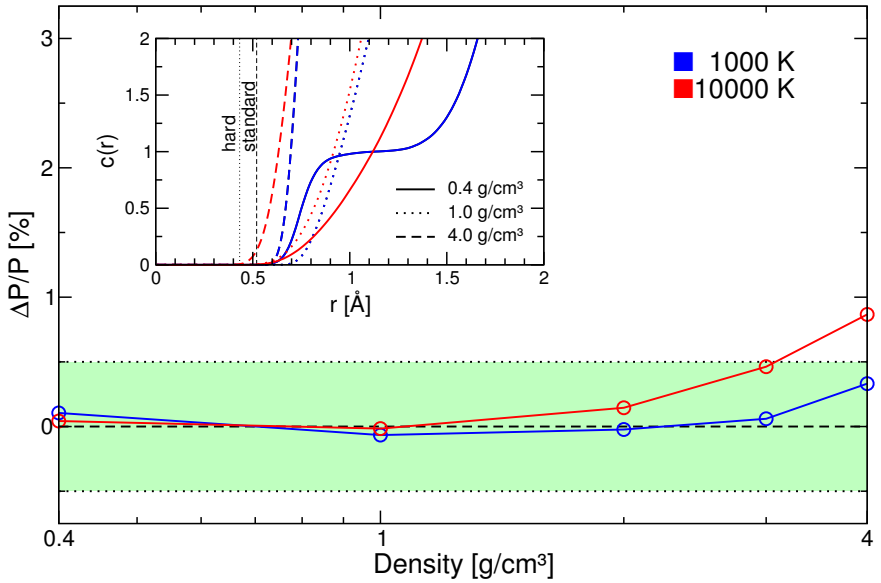

Figure A.4.: Pressure deviations between the standard and the hard PAW potential at 1000 (blue) and 10000 K (red). The green area indicates less than 0.5% deviation. Inset: Coordination number of hydrogen compared to the different PAW cutoff radii.

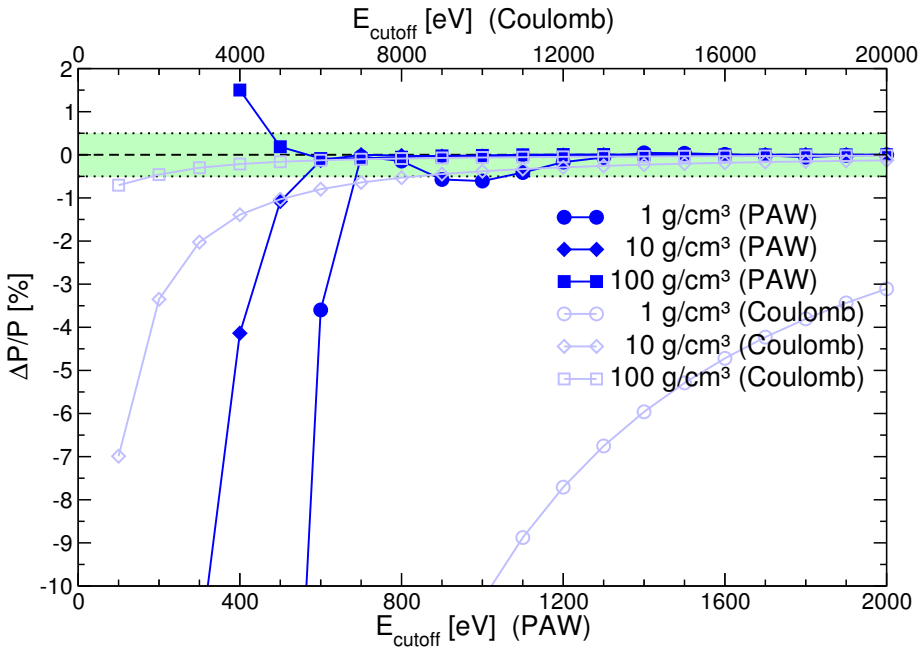

Figure A.5.: Pressure convergence for helium with respect to the plane wave cutoff energy at 1000 K. Shown are results for the PAW (filled symbols, bottom axis) and the Coulomb (open symbols, top axis) potentials.

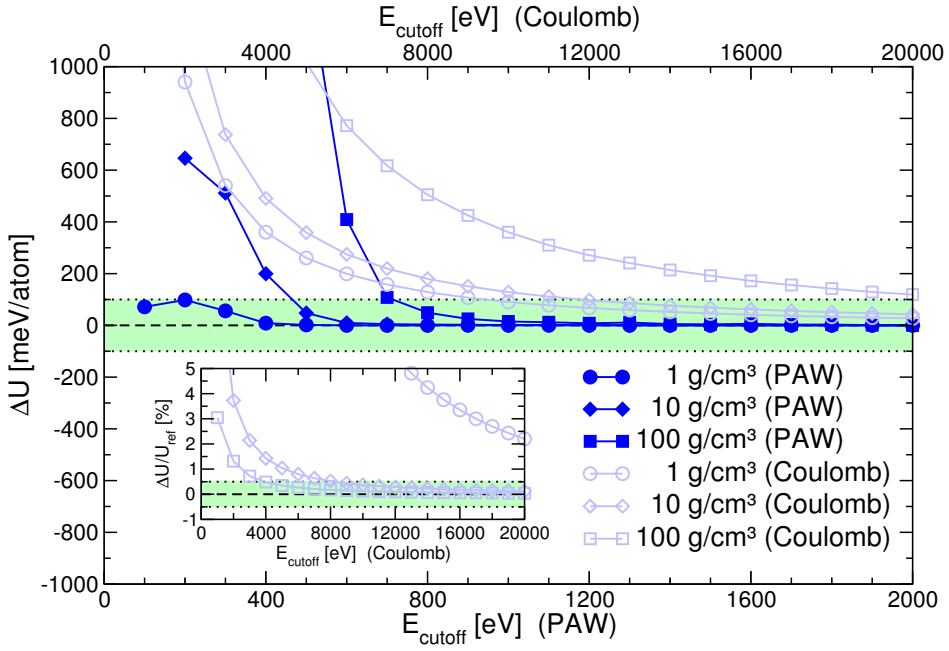

Figure A.6.: Energy convergence for helium for the same parameters. The inset shows the relative convergence to the reference energy (see text).

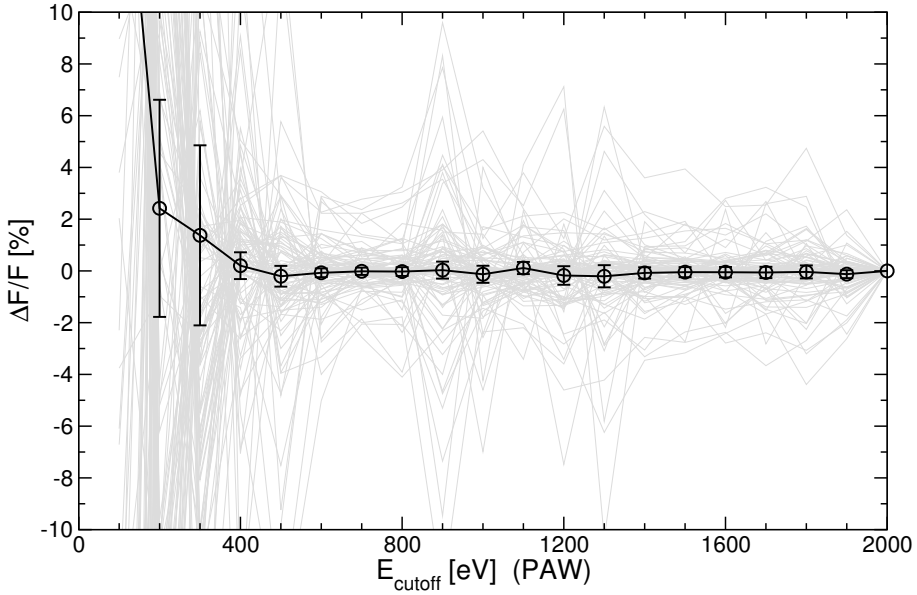

Figure A.7.: Convergence of the force components of all helium ions (gray lines) at 1 g/cm^3 and 1000 K. The mean values are shown in black.

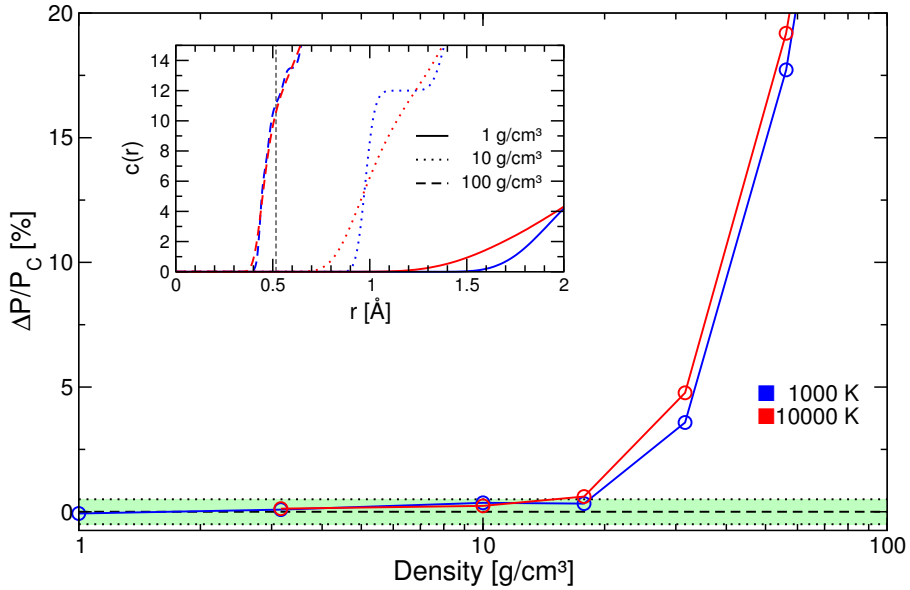

Figure A.8.: Pressure deviations between the PAW and the Coulomb potential. Inset: Coordination number of helium compared to the PAW cutoff radius.

A.1.2. **k**-point sampling and finite size effects

Since the computational time scales roughly linearly with the number of used **k**-points, it is desirable to use as few points as possible with still converged results. The number of needed **k**-points is connected to the size of the simulation box, which in turn is of course directly connected to the particle number. Usually, a larger simulation box needs less **k**-points to reach a good convergence. Therefore, the tests were performed with several different particle numbers. All convergence tests were performed with the established plane wave and PAW cutoffs from the previous section. Here, the snapshots were evaluated with different Monkhorst-Pack grids from $1\times1\times1$ (equivalent to the Γ point) to $9\times9\times9$, as well as the BMVP. The result obtained with the $9\times9\times9$ grid was taken as the reference value.

The results for hydrogen are shown in figure A.9 for a temperature of 1000 K. The pressure converges fast with the number of **k**-points, usually a $2\times2\times2$ grid is enough to reach convergence of better than 0.5%. However, this needs already about four times more computational time than a single **k**-point. While the results with the Γ point alone are usually converged within few percents (which might be acceptable for some applications), in general a better choice is the BMVP, which is for most cases converged to better than 1%.

Similar results were obtained for helium (figure A.10). While the pressure calculated at the Γ point can deviate up to about 8% compared to a better sampling for low particle numbers, the BMVP is again usually converged to better than 1%.

As expected the convergence gets in general better with larger volumes, i.e. higher particle numbers or lower densities. Therefore, it is often beneficient to increase the particle number instead of the number of **k**-points, thus getting better statistics or a better sampling of a phase transition.

Since good convergence can be reached with the BMVP, this point was chosen for all MD simulations in this work. Note that the convergence tests in this section are only for *static* calculations, the convergence of MD simulations with respect to the particle number and **k**-point sampling is discussed in section A.2.

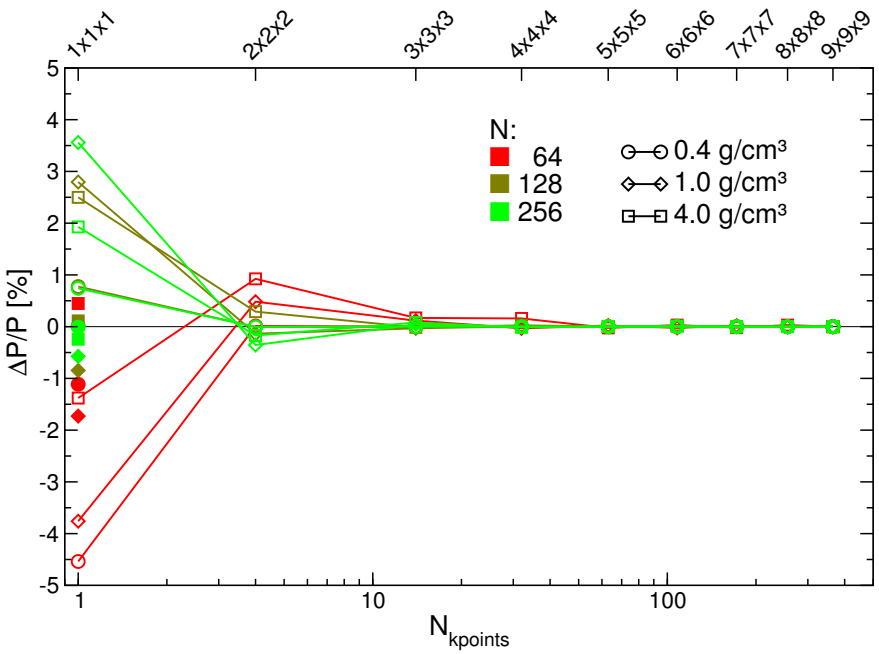

Figure A.9.: Convergence with respect to **k**-point sampling (Monkhorst-Pack: open symbols; BMVP: filled symbols) for hydrogen with different particle numbers. The corresponding Monkhorst-Pack grids are noted on the top axis.

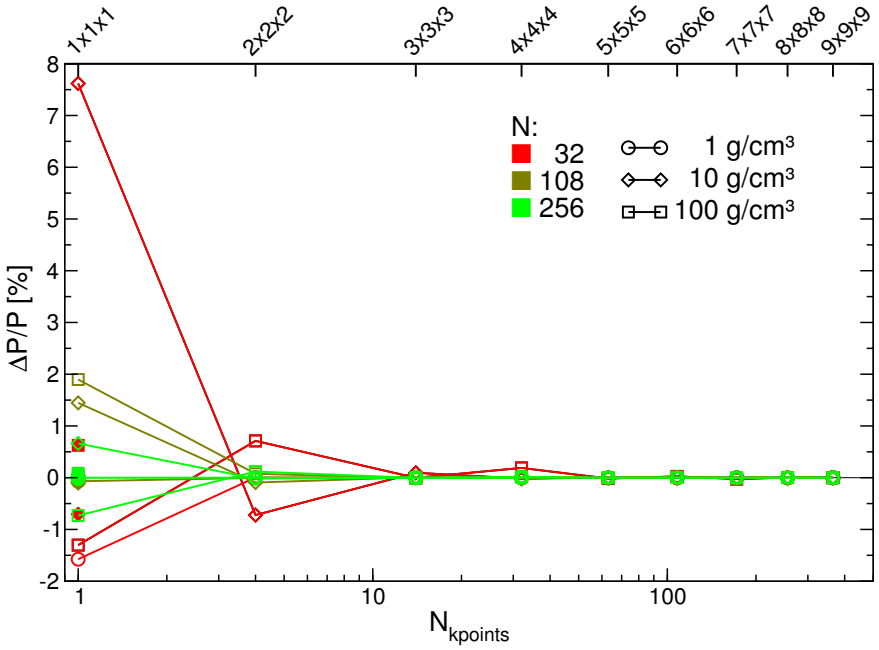

Figure A.10.: Convergence with respect to **k**-point sampling (Monkhorst-Pack: open symbols; BMVP: filled symbols) for helium with different particle numbers. The corresponding Monkhorst-Pack grids are noted on the top axis.

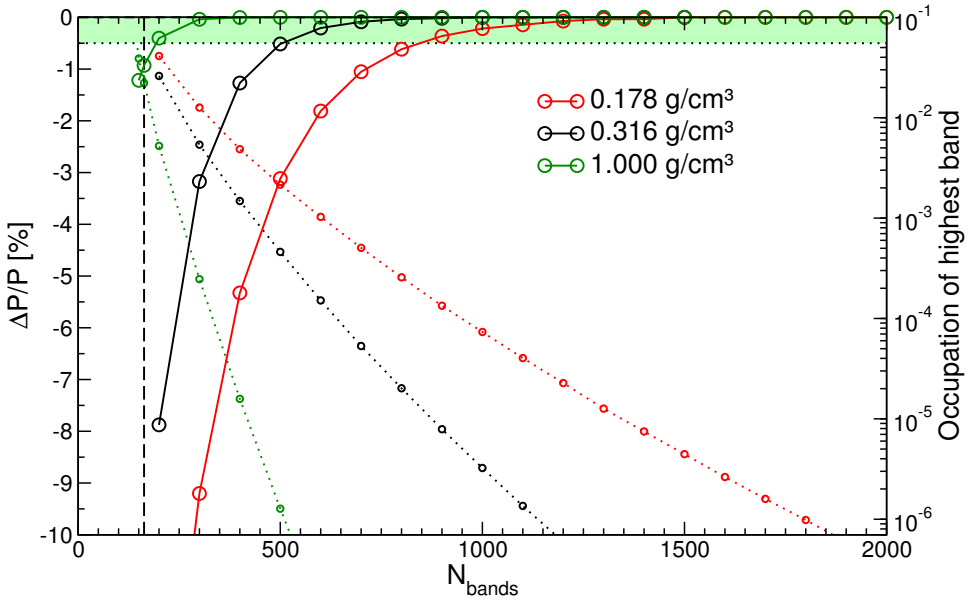

Figure A.11.: Convergence of the pressure with respect to the number of considered bands for helium at a temperature of 30000 K (solid lines). The occupation of the highest band is also shown (dotted lines, right axis). The dashed line indicates the default value of VASP.

A.1.3. Number of bands

In finite-temperature DFT, the occupation of the electronic states (or bands) is determined by the fermi distribution. While this function is near a step function at high densities and low temperatures, it gets smeared out at high temperatures and low densities, leading to higher occupied bands. Therefore it is necessecary to consider enough electronic states in the calculations. Additionally it is important for the used algorithm (RMM-DIIS)[204] to have enough empty bands in the calculation. On the other hand, the compuational time scales roughly with N_{bands}^2, making simulations at high temperatures very demanding. Since high temperatures and low densities were considered only for helium, explicit convergence tests were only performed for this element. In figure A.11, the convergence with respect to the number of bands is shown for a temperature of 30000 K and densities between 0.178 and 1 g/cm^3. In general, the convergence is always better than 0.5%, if the occupation of the highest band is below 1×10^4. This was ensured for all calculations for the helium EOS in chapter 7.

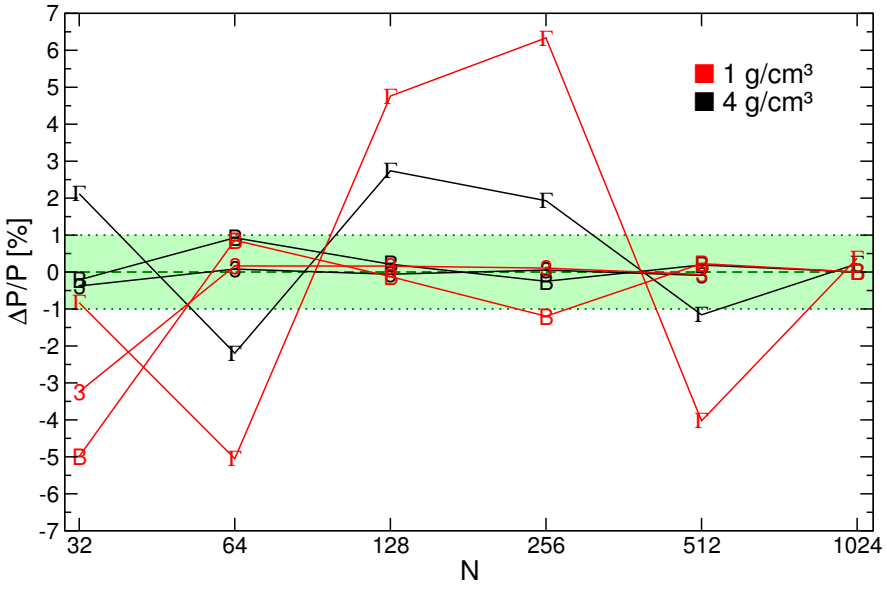

Figure A.12.: Convergence of the pressure with respect to the particle number for the Γ point (Γ), the BMVP (B), and a 3×3×3 Monkhorst-Pack grid (3). Shown are results for hydrogen at a density of 1 (black) and 4 g/cm^3 (red) and a temperature of 1000 K.

A.2. Convergence of the MD simulations

So far, only the convergence of the static electronic structure calculations has been studied. The main goal are, however, MD simulations, which might influence the results of the previous section. Depending on the convergence behavior of the electronic structure calculation, the convergence might be either less or more involved. If the convergence with respect to some parameter fluctuates statistically for different snapshots, even a bad convergence of the static DFT calculations might lead to reasonable MD results. If in contrast the convergence is systematic for all snapshots, than the MD results might be even worse than the static DFT calculations.

Due to the PAW method and the very good convergence with respect to the plane wave cutoff (no change at all after convergence is reached), it can be expected that this behavior persists for the MD simulations. The convergence with respect to the **k** points is analyzed in the next section.

An additional parameter for MD simulations is the size of the used timestep, which is discussed in section A.2.2.

A.2.1. Particle number and finite size effects

The most obvious parameter which has to be checked for all MD simulations is the number of particles considered. Similar to the convergence tests for the *static* calculations in section A.1.2, MD simulations for hydrogen with different particle numbers were performed at 1 and 4 g/cm^3 at 1000 K. Since the system size has an influence on the **k**-point convergence, all simulations were

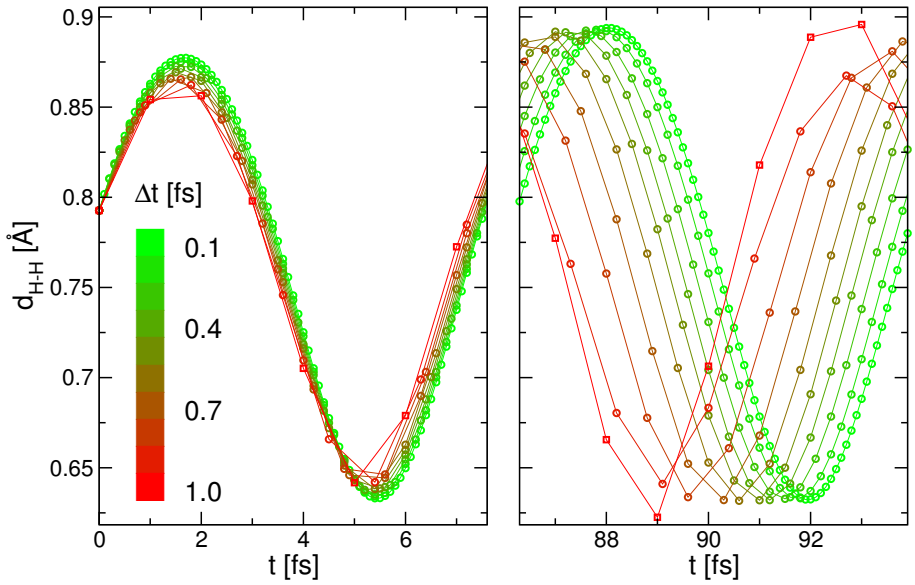

Figure A.13.: Molecular distance of one selected hydrogen molecule at 0.4 g/cm^3 and 1000 K over time with different timesteps, all starting from the same configuration.

performed at the Γ point, the BMVP, and (if computationally feasible) with a 3×3×3 Monkhorst-Pack grid. The result with 1024 hydrogen atoms and the BMVP was chosen as the best reference value, because it was not possible to use a larger **k**-point set at this particle number. The other possible choice, 512 hydrogen atoms and a 3×3×3 **k**-point set would change the outcome very little. The results are shown in figure A.12, the results for 1 g/cm^3 were also part of Paper II (chapter 4). As can be seen, 64 hydrogen atoms yield well converged results (within 0.2%) with a good **k**-point sampling, i.e. 3×3×3. While the BMVP reaches a convergence of about 1% at the same particle number, the Γ point converges very badly for both densities.

Again, it can be seen that the BMVP, which was used throughout this work, is a very good choice for MD simulations.

A.2.2. Time step

The timestep for a MD simulation has to be chosen very carefully. It has to be small enough to resolve all important oscillations in the system, but the timestep should also be large enough that reasonable timescales can be simulated. The fastest oscillation which occurs in the considered systems, i.e. hydrogen and helium, is the vibration of the hydrogen molecule, which has a period of about 7.6 fs.[227] A common recommendation for the timestep is 1/30 of this period,[149] depending on the integration algorithm. To test this recommendation, a simulation for pure hydrogen at 0.4 g/cm^3 and 1000 K was performed, conditions where hydrogen is mostly in the molecular phase. One molecule was selected randomly from this simulation and its distance $d_{\text{H-H}}$ was calculated over time with different timesteps between 0.1 and 1.0 fs, see figure A.13. A small but

systematic drift can be observed between the different timesteps, which prevails even at the smallest ones (0.1 and 0.2 fs). But even for a very large timestep of 1.0 fs this drift is only about 3%, which is still acceptable for many applications. However, especially when the density increases, a too large timestep is more problematic, because the molecules might dissociate two early due to unphysical collisions. For example, the transition pressure of the first-order phase transition in liquid hydrogen gets shifted a few percent downwards with a timestep of 1.0 fs compared to 0.3 fs.

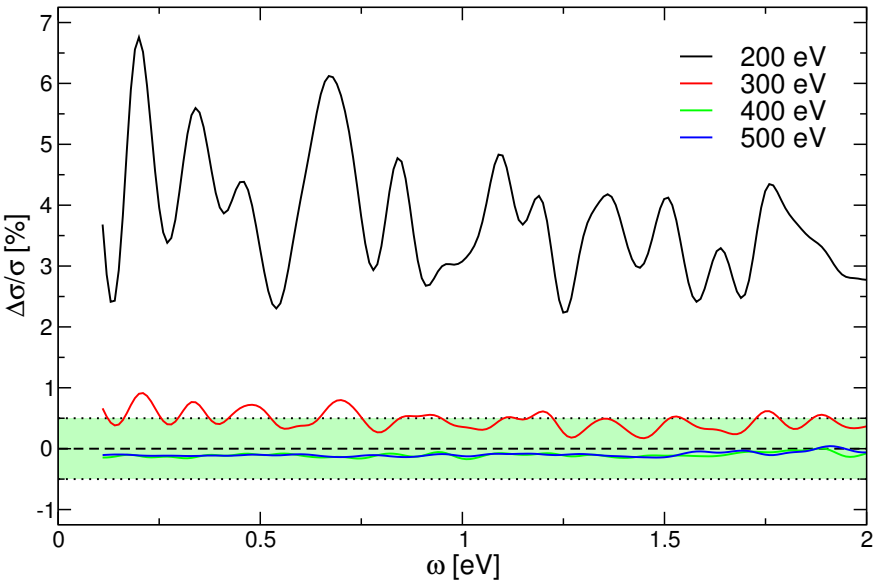

Figure A.14.: Convergence of the dynamic electrical conductivity with respect to the plane wave cutoff for the example of hydrogen at 1 g/cm^{3}and 1000 K. Shown is the deviation of $\sigma(\omega)$ from the one calculated with a cutoff energy of 1000 eV.

A.3. Convergence of the electrical and thermal conductivity

The convergence behavior of the conductivity concerning **k** points, particle number, and plane wave cutoff is not necessarily the same as for the thermodynamic quantities. For this reason, additional convergence tests have to be performed, which are discussed in the following sections. In this work, extensive electrical conductivity calculations were performed for pure hydrogen with 512 electrons (Paper II, chapter 4) as well as electrical and thermal conductivity calculations for hydrogen-helium mixtures with 256 electrons (Paper III, chapter 5 and section 8.4). Therefore, only for these systems convergence tests are shown here. Although only the static limits of the conductivities were of interest for this work, the dynamic conductivities are compared. This allows for a more quantitative convergence test, since the static limit is sensitive to the specific parameters of obtaining it, e.g. in which region the regression was applied. For this purpose the relative deviation between the dynamic conductivity at each parameter setting compared to the best result is evaluated, i.e. $\frac{\sigma_{\text{current}}(\omega)-\sigma(\omega)}{\sigma(\omega)} = \frac{\Delta\sigma(\omega)}{\sigma(\omega)}$ and $\frac{\lambda_{\text{current}}(\omega)-\lambda(\omega)}{\lambda(\omega)} = \frac{\Delta\lambda(\omega)}{\lambda(\omega)}$. A typical outcome of this procedure can be seen for the plane wave convergence in figure A.14. Since this function is nearly constant apart from the oscillations due to the discrete energy bands, the average over ω in the region between the mean band distance and about 2 eV is taken as the averaged convergence $\overline{\Delta\sigma(\omega)/\sigma(\omega)}$ and $\overline{\Delta\lambda(\omega)/\lambda(\omega)}$, respectively.

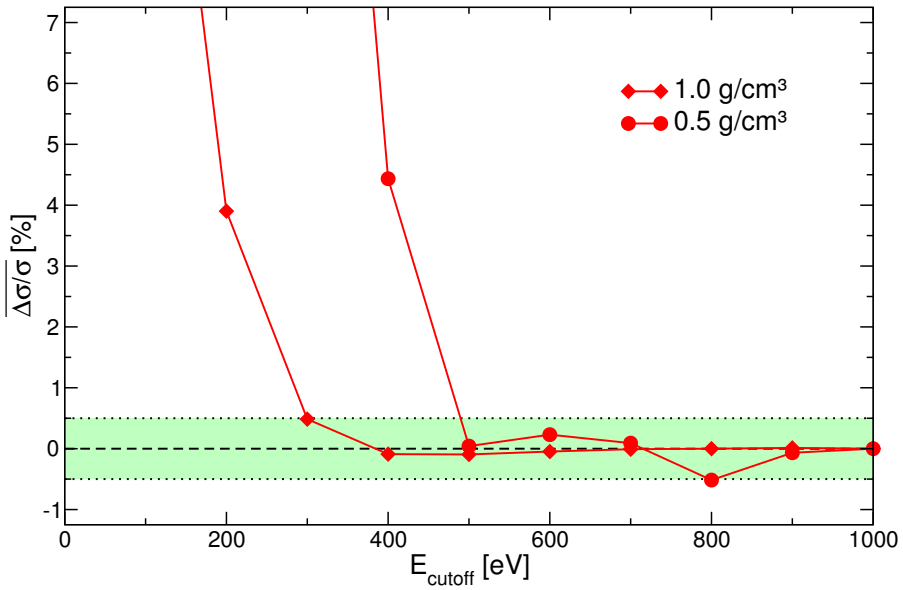

Figure A.15.: Averaged convergence of the electrical conductivity $\sigma(\omega)$ with respect to the plane wave cutoff for hydrogen at 1000 K.

A.3.1. Plane wave cutoff

No accurate forces on the ions and no pressures are needed for snapshots of the electrical conductivity. Therefore, a reduced plane wave cutoff might be sufficient, which would reduce the computational demands. To study this effect, the conductivities were calculated with $4\times4\times4$ Monkhorst-Pack **k**-point set and different plane wave cutoffs up to 1000 eV. As an example, the result for pure hydrogen at 1000 K and 1 g/cm^3 is shown in figure A.14. Already from this figure, it is clear that a much lower plane wave cutoff is needed for the conductivity calculations than for the MD simulations. For all further analysis, only the averaged convergence is shown as explained in the previous section.

The results for the electrical conductivity of hydrogen are shown in figure A.15 for 0.5 and 1 g/cm^3 at 1000 K, the relevant region where conductivity calculations were performed. Very good convergence of better than 0.5% is reach for a 500 and 400 eV plane wave cutoff, respectively.

The results for the electrical and thermal conductivity of hydrogen-helium mixtures along the Jovian isentrope are shown in figures A.16 and A.17, respectively. For the electrical conductivity 400 eV are always enough, while the thermal conductivity needs a higher plane wave cutoff of 600 eV at the lowest density.

As expected the plane wave cutoff can be reduced compared to the MD simulations. All published results were obtained with a 1200 eV cutoff, while the results in section 8.4 where obtained with 800 eV; both settings are more than enough for well converged results.

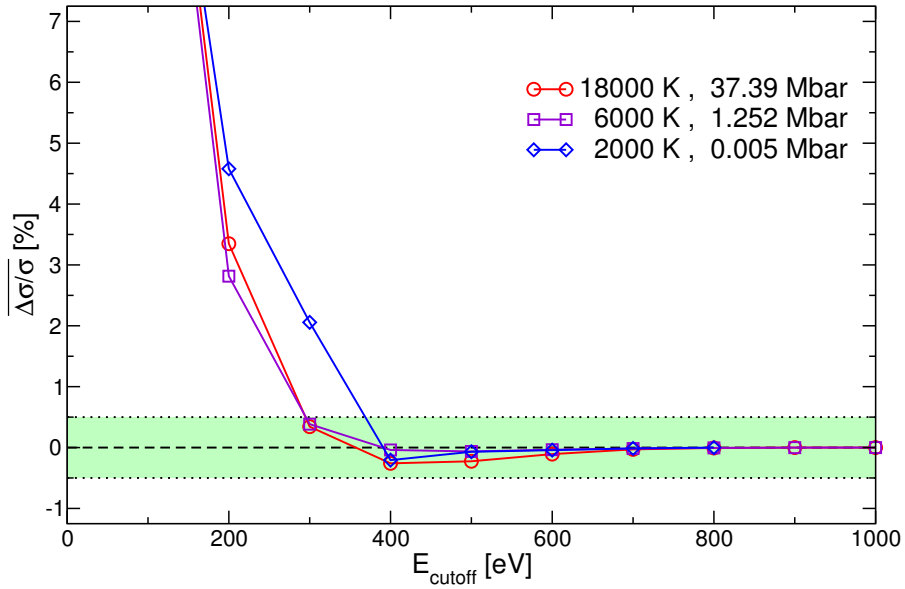

Figure A.16.: Averaged convergence of the electrical conductivity $\sigma(\omega)$ with respect to the plane wave cutoff for a hydrogen-helium mixture along the Jovian isentrope.

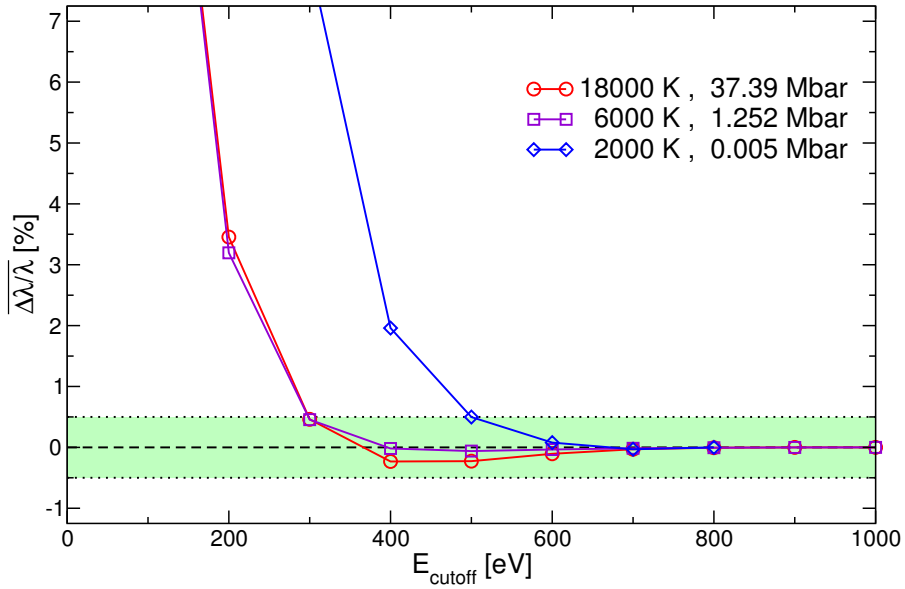

Figure A.17.: Averaged convergence of the thermal conductivity $\lambda(\omega)$ with respect to the plane wave cutoff for a hydrogen-helium mixture along the Jovian isentrope.

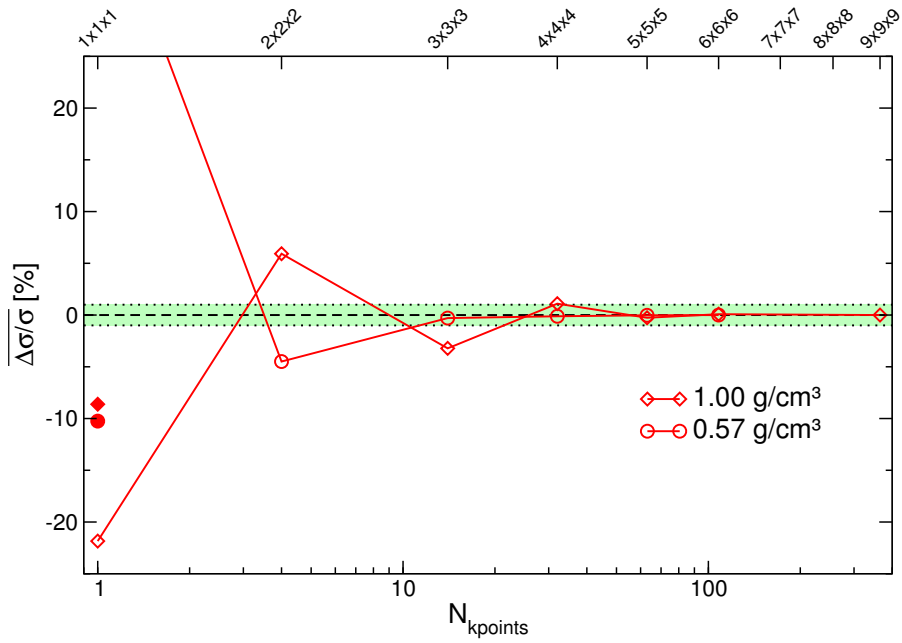

Figure A.18.: Averaged convergence of the electrical conductivity $\sigma(\omega)$ with respect to the **k**-point sampling (Monkhorst-Pack: open symbols, BMVP: filled symbols) for hydrogen at 1000 K. The corresponding Monkhorst-Pack grids are noted on the top axis.

A.3.2. **k**-point sampling

While the plane wave cutoff can be reduced for conductivity calculations, it can be expected that the convergence with respect to the **k**-point sampling is more involved. To check this convergence, the same snapshots as before were evaluated with the converged plane wave cutoffs for different **k**-point sets up to $9\times9\times9$. Again, only the averaged convergence is shown. The results for pure hydrogen are shown in figure A.18 for the same parameters as before and reveal a very good convergence to better than 0.5% with a $4\times4\times4$ **k**-point set. As expected, the convergence is better for the lower density, since its volume is larger, and a $3\times3\times3$ **k**-point sampling is sufficient. Again, it can be seen that the BMVP yields much better results than the Γ point, but in this case still deviates up to about 10% from the converged value.

The results for the electrical and thermal conductivity along Jupiter's isentrope are shown in figures A.19 and A.20, respectively. Again a $4\times4\times4$ **k**-point sampling is always sufficient for well converged results, which can be reduced for the lower densities. At the lowest density even the BMVP and the Γ point yield converged conductivities.

All results in this work (Paper II, Paper III, and section 8.4) were obtained with a $4\times4\times4$ Monkhorst-Pack grid, and are thus well converged.

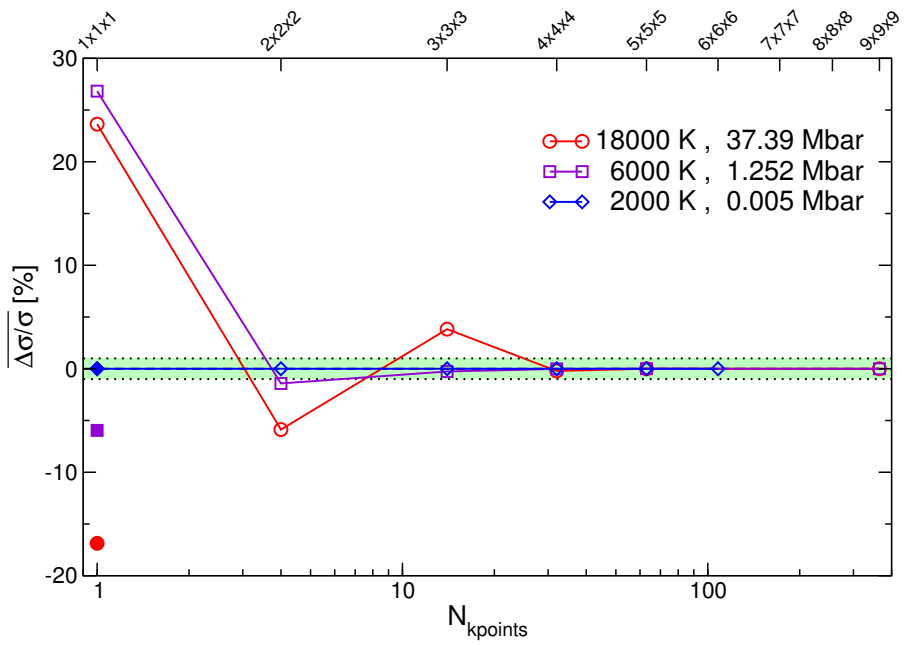

Figure A.19.: Averaged convergence of the electrical conductivity $\sigma(\omega)$ with respect to the **k**-point sampling (Monkhorst-Pack: open symbols, BMVP: filled symbols) for a hydrogen-helium mixture along the Jovian isentrope. The corresponding Monkhorst-Pack grids are noted on the top axis.

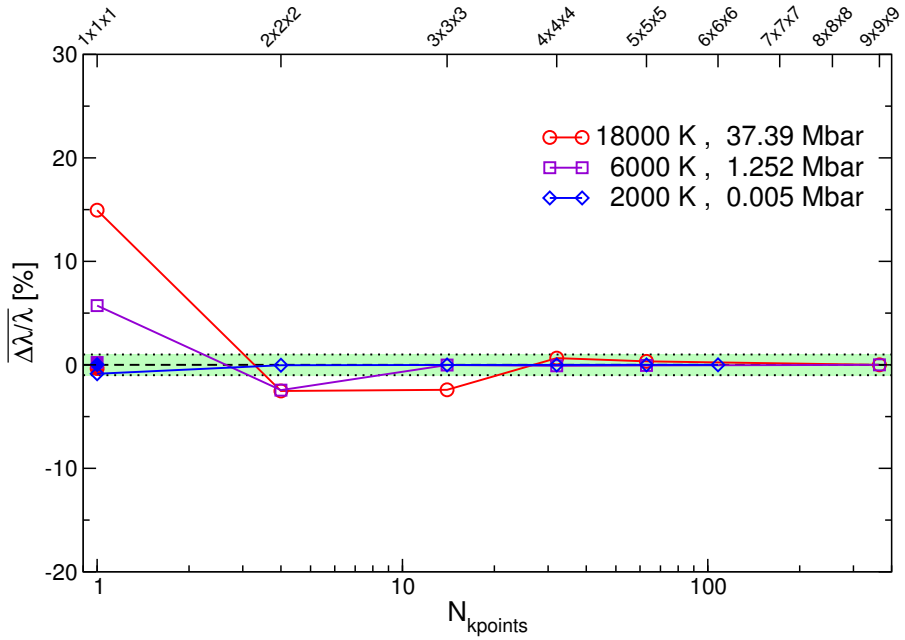

Figure A.20.: Averaged convergence of the thermal conductivity $\lambda(\omega)$ with respect to the **k**-point sampling (Monkhorst-Pack: open symbols, BMVP: filled symbols) for a hydrogen-helium mixture along the Jovian isentrope.

B. Bibliography

[1] J. D. Lindl, P. Amendt, R. L. Berger, S. G. Glendinning, S. H. Glenzer, S. W. Haan, R. L. Kauffman, O. L. Landen, and L. J. Suter, Phys. Plasmas **11**, 339 (2004).

[2] K. Lodders, Astrophys. J. **591**, 1220 (2003).

[3] A. Gurnett and A. Bhattacharjee, *Introduction to Plasma Physics: With Space and Laboratory Applications* (Cambridge University Press, 2005).

[4] L. M. Haffner, R. J. Reynolds, S. L. Tufte, G. J. Madsen, K. P. Jaehnig, and J. W. Percival, Astrophys. J. Suppl. Ser. **149**, 405 (2003), (interstellar medium); IPP, Max-Planck-Gesellschaft zur Förderung der Wissenschaften e. V., (stellarator, tokamak); NASA/JPL/University of Arizona, "photojournal.jpl.nasa.gov/catalog/pia02873," (2001), (Jupiter); SOHO (ESA & NASA), "sohowww.nascom.nasa.gov/gallery/images/eit5prom.html," (2001), (solar core); NASA/courtesy of nasaimages.org, "www.nasaimages.org/luna/servlet/s/h721lc," (1999), (solar corona); Lawrence Livermore National Laboratory, (ICF).

[5] W.-D. Kraeft, D. Kremp, W. Ebeling, and G. Röpke, *Quantum Statistics of Charged Particle Systems* (Akademie-Verlag Berlin, 1986).

[6] R. Redmer, Phys. Rep. **282**, 35 (1997).

[7] D. Kremp, V. Bezkrovniy, W. D. Kraeft, and M. Schlanges, Contrib. Plasma Phys. **45**, 266 (2005).

[8] D. Saumon, G. Chabrier, and H. M. van Horn, Astrophys. J. Suppl. Ser. **99**, 713 (1995).

[9] M. Ross, F. H. Ree, and D. A. Young, J. Chem. Phys. **79**, 1487 (1983).

[10] M. Ross, Phys. Rev. B **58**, 669 (1998).

[11] A. Bunker, S. Nagel, R. Redmer, and G. Röpke, Phys. Rev. B **56**, 3094 (1997).

[12] H. Juranek and R. Redmer, J. Chem. Phys. **112**, 3780 (2000).

[13] H. Juranek, R. Redmer, and Y. Rosenfeld, J. Chem. Phys. **117**, 1768 (2002).

[14] R. Redmer, B. Holst, H. Juranek, N. Nettelmann, and V. Schwarz, J. Phys. A **39**, 4479 (2006).

[15] B. Holst, N. Nettelmann, and R. Redmer, Contrib. Plasma Phys. **47**, 368 (2007).

[16] B. Holst, R. Redmer, and M. P. Desjarlais, Phys. Rev. B **77**, 184201 (2008).

[17] R. Car and M. Parrinello, Phys. Rev. Lett. **55**, 2471 (1985).

[18] N. D. Mermin, Phys. Rev. **137**, A1441 (1965).

[19] J. P. Perdew, A. Ruzsinszky, J. Tao, V. N. Staroverov, G. E. Scuseria, and G. I. Csonka, J. Chem. Phys. **123**, 062201 (2005).

[20] A. E. Mattsson, P. A. Schultz, M. P. Desjarlais, T. R. Mattsson, and K. Leung, Model. Simul. Mater. Sci. Eng. **13**, R1 (2005).

[21] M. Knaup, P.-G. Reinhard, and C. Toepffer, Contrib. Plasma Phys. **39**, 57 (1999).

[22] M. Knaup, G. Zwicknagel, P.-G. Reinhard, and C. Toepffer, Nucl. Instr. Meth. A **464**, 267 (2001).

[23] M. Knaup, P.-G. Reinhard, C. Toepffer, and G. Zwicknagel, J. Phys. A **36**, 6165 (2003).

[24] B. Jakob, P.-G. Reinhard, C. Toepffer, and G. Zwicknagel, Phys. Rev. E **76**, 036406 (2007).

[25] B. Militzer and D. M. Ceperley, Phys. Rev. Lett. **85**, 1890 (2000).

[26] D. M. Ceperley and E. Manousakis, J. Chem. Phys. **115**, 10111 (2001).

[27] B. Militzer, Phys. Rev. B **79**, 155105 (2009).

[28] C. Pierleoni and D. Ceperley, in *Computer Simulations in Condensed Matter Systems: From Materials to Chemical Biology*, Lecture Notes in Physics, Vol. 1, edited by M. Ferrario, G. Ciccotti, and K. Binder (Springer, 2006).

[29] K. T. Delaney, C. Pierleoni, and D. M. Ceperley, Phys. Rev. Lett. **97**, 235702 (2006).

[30] M. A. Morales, C. Pierleoni, and D. M. Ceperley, Phys. Rev. E **81**, 021202 (2010).

[31] J. A. Schouten, N. J. Trappeniers, and L. C. van den Bergh, Rev. Sci. Instrum. **54**, 1209 (1983).

[32] H.-k. Mao and R. J. Hemley, Rev. Mod. Phys. **66**, 671 (1994).

[33] P. Loubeyre, R. LeToullec, D. Hausermann, M. Hanfland, R. J. Hemley, H. K. Mao, and L. W. Finger, Nature **383**, 702 (1996).

[34] M. I. Eremets and I. A. Troyan, Nat. Mater. **10**, 927 (2011).

[35] S. Deemyad and I. F. Silvera, Phys. Rev. Lett. **100**, 155701 (2008).

[36] M. I. Eremets and I. A. Trojan, JETP Lett. **89**, 174 (2009).

[37] N. Subramanian, A. F. Goncharov, V. V. Struzhkin, M. Somayazulu, and R. J. Hemley, Proc. Natl. Acad. Sci. USA **108**, 6014 (2011).

[38] D. Santamaría-Pérez, G. D. Mukherjee, B. Schwager, and R. Boehler, Phys. Rev. B **81**, 214101 (2010).

[39] Y. B. Zel'dovich and Y. P. Raizer, *Physics of Shock Waves and High-Temperature Hydrodynamic Phenomena* (Courier Dover Publications, 2002).

[40] W. J. Nellis, A. C. Mitchell, M. van Thiel, G. J. Devine, R. J. Trainor, and N. Brown, J. Chem. Phys. **79**, 1480 (1983).

[41] W. J. Nellis, A. C. Mitchell, P. C. McCandless, D. J. Erskine, and S. T. Weir, Phys. Rev. Lett. **68**, 2937 (1992).

[42] W. J. Nellis, S. T. Weir, and A. C. Mitchell, Phys. Rev. B **59**, 3434 (1999).

[43] P. M. Celliers, G. W. Collins, L. B. DaSilva, D. M. Gold, R. Cauble, R. J. Wallace, M. E. Foord, and B. A. Hammel, Phys. Rev. Lett. **84**, 5564 (2000).

[44] M. D. Knudson, D. L. Hanson, J. E. Bailey, C. A. Hall, J. R. Asay, and C. Deeney, Phys. Rev. B **69**, 144209 (2004).

[45] G. V. Boriskov, A. I. Bykov, R. I. Il'Kaev, V. D. Selemir, G. V. Simakov, R. F. Trunin, V. D. Urlin, A. N. Shuikin, and W. J. Nellis, Phys. Rev. B **71**, 092104 (2005).

[46] J. Eggert, S. Brygoo, P. Loubeyre, R. S. McWilliams, P. M. Celliers, D. G. Hicks, T. R. Boehly, R. Jeanloz, and G. W. Collins, Phys. Rev. Lett. **100**, 124503 (2008).

[47] D. G. Hicks, T. R. Boehly, P. M. Celliers, J. H. Eggert, S. J. Moon, D. D. Meyerhofer, and G. W. Collins, Phys. Rev. B **79**, 014112 (2009).

[48] T. J. Lenosky, J. D. Kress, and L. A. Collins, Phys. Rev. B **56**, 5164 (1997).

[49] H. Kitamura and S. Ichimaru, J. Phys. Soc. Jap. **67**, 950 (1998).

[50] T. J. Lenosky, S. R. Bickham, J. D. Kress, and L. A. Collins, Phys. Rev. B **61**, 1 (2000).

[51] G. Galli, R. Q. Hood, A. U. Hazi, and F. Gygi, Phys. Rev. B **61**, 909 (2000).

[52] D. Beule, W. Ebeling, A. Förster, H. Juranek, R. Redmer, and G. Röpke, Phys. Rev. E **63**, 060202 (2001).

[53] M. P. Desjarlais, Phys. Rev. B **68**, 064204 (2003).

[54] S. A. Bonev, B. Militzer, and G. Galli, Phys. Rev. B **69**, 014101 (2004).

[55] V. Bezkrovniy, M. Schlanges, D. Kremp, and W. D. Kraeft, Phys. Rev. E **69**, 061204 (2004).

[56] V. Bezkrovniy, V. S. Filinov, D. Kremp, M. Bonitz, M. Schlanges, W. D. Kraeft, P. R. Levashov, and V. E. Fortov, Phys. Rev. E **70**, 057401 (2004).

[57] M. Schlanges, V. Bezkrovniy, J. Vorberger, D. Kremp, and W. D. Kraeft, Contrib. Plasma Phys. **45**, 405 (2005).

[58] K. K. M. Lee, L. R. Benedetti, R. Jeanloz, P. M. Celliers, J. H. Eggert, D. G. Hicks, S. J. Moon, A. Mackinnon, L. B. D. Silva, D. K. Bradley, W. Unites, G. W. Collins, E. Henry, M. Koenig, A. Benuzzi-Mounaix, J. Pasley, and D. Neely, J. Chem. Phys. **125**, 014701 (2006).

[59] W. J. Nellis, N. C. Holmes, A. C. Mitchell, R. J. Trainor, G. K. Governo, M. Ross, and D. A. Young, Phys. Rev. Lett. **53**, 1248 (1984).

[60] B. Militzer, D. M. Ceperley, J. D. Kress, J. D. Johnson, L. A. Collins, and S. Mazevet, Phys. Rev. Lett. **87**, 275502 (2001).

[61] A. Kietzmann, B. Holst, R. Redmer, M. P. Desjarlais, and T. R. Mattsson, Phys. Rev. Lett. **98**, 190602 (2007).

[62] M. D. Knudson, D. L. Hanson, J. E. Bailey, C. A. Hall, and J. R. Asay, Phys. Rev. Lett. **90**, 035505 (2003).

[63] W. J. Nellis, Rep. Prog. Phys. **69**, 1479 (2006).

[64] V. Diatschenko, C. W. Chu, D. H. Liebenberg, D. A. Young, M. Ross, and R. L. Mills, Phys. Rev. B **32**, 381 (1985).

[65] F. Datchi, P. Loubeyre, and R. Le Toullec, Phys. Rev. B **61**, 6535 (2000).

[66] E. Gregoryanz, A. F. Goncharov, K. Matsuishi, H.-k. Mao, and R. J. Hemley, Phys. Rev. Lett. **90**, 175701 (2003).

[67] S. A. Bonev, E. Schwegler, T. Ogitsu, and G. Galli, Nature **431**, 669 (2004).

[68] M. A. Morales, C. Pierleoni, E. Schwegler, and D. M. Ceperley, Proc. Natl. Acad. Sci. USA **107**, 12799 (2010).

[69] L. Caillabet, S. Mazevet, and P. Loubeyre, Phys. Rev. B **83**, 094101 (2011).

[70] C. J. Pickard and R. J. Needs, Nature Phys. **3**, 473 (2007).

[71] J. M. McMahon and D. M. Ceperley, Phys. Rev. Lett. **106**, 165302 (2011).

[72] V. V. Kechin, J. Phys.: Condens. Matter **7**, 531 (1995).

[73] R. K. Crawford and W. B. Daniels, J. Chem. Phys. **55**, 5651 (1971).

[74] R. L. Mills, D. H. Liebenberg, and J. C. Bronson, Phys. Rev. B **21**, 5137 (1980).

[75] P. Loubeyre, J. M. Besson, J. P. Pinceaux, and J. P. Hansen, Phys. Rev. Lett. **49**, 1172 (1982).

[76] W. L. Vos, M. G. E. van Hinsberg, and J. A. Schouten, Phys. Rev. B **42**, 6106 (1990).

[77] D. A. Young, A. K. McMahan, and M. Ross, Phys. Rev. B **24**, 5119 (1981).

[78] D. Lévesque, J.-J. Weis, and M. L. Klein, Phys. Rev. Lett. **51**, 670 (1983).

[79] P. Loubeyre and J.-P. Hansen, Phys. Rev. B **31**, 634 (1985).

[80] M. Ross and D. A. Young, Phys. Lett. A **118**, 463 (1986).

[81] L. Koči, R. Ahuja, A. B. Belonoshko, and B. Johansson, J. Phys.: Condens. Matter **19**, 016206 (2007).

[82] H. K. Mao, R. J. Hemley, Y. Wu, A. P. Jephcoat, L. W. Finger, C. S. Zha, and W. A. Bassett, Phys. Rev. Lett. **60**, 2649 (1988).

[83] P. Loubeyre, R. LeToullec, J. P. Pinceaux, H. K. Mao, J. Hu, and R. J. Hemley, Phys. Rev. Lett. **71**, 2272 (1993).

[84] W. B. Streett, Astrophys. J. **186**, 1107 (1973).

[85] L. C. van den Bergh, J. Schouten, and N. Trappeniers, Physica A **141**, 524 (1987).

[86] J. Schouten, L. van den Bergh, and N. Trappeniers, Chem. Phys. Lett. **114**, 401 (1985).

[87] J. Schouten and L. V. D. Bergh, Fluid Phase Equilib. **32**, 1 (1986).

[88] P. Loubeyre, R. Le Toullec, and J. P. Pinceaux, Phys. Rev. B **36**, 3723 (1987).

[89] P. Loubeyre, R. Le Toullec, and J. P. Pinceaux, J. Phys.: Condens. Matter **3**, 3183 (1991).

[90] L. C. van den Bergh and J. A. Schouten, J. Chem. Phys. **89**, 2336 (1988).

[91] W. L. Vos, A. de Kuijper, J. L. Barrat, and J. A. Schouten, J. Phys.: Condens. Matter **3**, 1613 (1991).

[92] H. Juranek, N. Nettelmann, S. Kuhlbrodt, V. Schwarz, B. Holst, and R. Redmer, Contrib. Plasma Phys. **45**, 432 (2005).

[93] P. P. Edwards, M. T. J. Lodge, F. Hensel, and R. Redmer, Phil. Trans. R. Soc. A **368**, 941 (2010).

[94] R. Redmer, B. Holst, and F. Hensel, eds., *Metal-to-Nonmetal Transitions*, Springer Series in Material Sciences, Vol. 132 (Springer, 2010).

[95] E. Wigner and H. B. Huntington, J. Chem. Phys. **3**, 764 (1935).

[96] N. F. Mott, Proc. Phys. Soc. A **62**, 416 (1949).

[97] N. F. Mott, Rev. Mod. Phys. **40**, 677 (1968).

[98] L. Landau and J. Zeldovich, Acta Physicochim. URSS **18**, 194 (1943).

[99] M. Robnik and W. Kundt, A&A **120**, 227 (1983).

[100] W. Ebeling and W. Richert, Phys. Lett. A **108**, 80 (1985).

[101] M. S. Marley and W. B. Hubbard, Icarus **73**, 536 (1988).

[102] M. Schlanges, M. Bonitz, and A. Tschttschjan, Contrib. Plasma Phys. **35**, 109 (1995).

[103] H. Reinholz, R. Redmer, and S. Nagel, Phys. Rev. E **52**, 5368 (1995).

[104] W. R. Magro, D. M. Ceperley, C. Pierleoni, and B. Bernu, Phys. Rev. Lett. **76**, 1240 (1996).

[105] D. Beule, W. Ebeling, A. Förster, H. Juranek, S. Nagel, R. Redmer, and G. Röpke, Phys. Rev. B **59**, 14177 (1999).

[106] W. J. Nellis, S. T. Weir, and A. C. Mitchell, Science **273**, 936 (1996).

[107] S. T. Weir, A. C. Mitchell, and W. J. Nellis, Phys. Rev. Lett. **76**, 1860 (1996).

[108] V. E. Fortov, R. I. Ilkaev, V. A. Arinin, V. V. Burtzev, V. A. Golubev, I. L. Iosilevskiy, V. V. Khrustalev, A. L. Mikhailov, M. A. Mochalov, V. Y. Ternovoi, and M. V. Zhernokletov, Phys. Rev. Lett. **99**, 185001 (2007).

[109] F. Lin, M. A. Morales, K. T. Delaney, C. Pierleoni, R. M. Martin, and D. M. Ceperley, Phys. Rev. Lett. **103**, 256401 (2009).

[110] I. Tamblyn and S. A. Bonev, Phys. Rev. Lett. **104**, 065702 (2010).

[111] S. Scandolo, Proc. Natl. Acad. Sci. USA **100**, 3051 (2003).

[112] J. Vorberger, I. Tamblyn, B. Militzer, and S. A. Bonev, Phys. Rev. B **75**, 024206 (2007).

[113] W. Lorenzen, B. Holst, and R. Redmer, Phys. Rev. B **82**, 195107 (2010).

[114] E. Liberatore, M. A. Morales, D. M. Ceperley, and C. Pierleoni, Mol. Phys. **109**, 3029 (2011).

[115] V. Labet, P. Gonzalez-Morelos, R. Hoffmann, and N. W. Ashcroft, J. Chem. Phys. **136**, 074501 (2012); V. Labet, R. Hoffmann, and N. W. Ashcroft, J. Chem. Phys. **136**, 074502 (2012); V. Labet, R. Hoffmann, and N. W. Ashcroft, J. Chem. Phys. **136**, 074503 (2012); V. Labet, R. Hoffmann, and N. W. Ashcroft, J. Chem. Phys. **136**, 074504 (2012).

[116] W. J. Nellis, A. L. Ruoff, and I. F. Silvera, ArXiv e-prints , 1201.0407 (2012).

[117] P. M. Kowalski, S. Mazevet, D. Saumon, and M. Challacombe, Phys. Rev. B **76**, 075112 (2007).

[118] L. Stixrude and R. Jeanloz, Proc. Natl. Acad. Sci. USA **32**, 11071 (2008).

[119] S. A. Khairallah and B. Militzer, Phys. Rev. Lett. **101**, 106407 (2008).

[120] P. M. Celliers, P. Loubeyre, J. H. Eggert, S. Brygoo, R. S. McWilliams, D. G. Hicks, T. R. Boehly, R. Jeanloz, and G. W. Collins, Phys. Rev. Lett. **104**, 184503 (2010).

[121] A. Förster, T. Kahlbaum, and W. Ebeling, Laser Part. Beams **10**, 253 (1992).

[122] C. Winisdoerffer and G. Chabrier, Phys. Rev. E **71**, 026402 (2005).

[123] V. Ternovoi, S. Kvitov, A. Pyalling, A. Filimonov, and V. Fortov, JETP Lett. **79**, 6 (2004).

[124] Y. J. Gu, Q. F. Chen, L. C. Cai, Z. Y. Chen, J. Zheng, and F. Q. Jing, J. Chem. Phys. **130**, 184506 (2009).

[125] H. Chacham, S. P. Reis, and B. Koiller, J. Chem. Phys. **109**, 4047 (1998).

[126] D. J. Stevenson, Phys. Rev. B **12**, 3999 (1975).

[127] D. J. Stevenson and E. E. Salpeter, Astrophys. J. Suppl. Ser. **35**, 221 (1977).

[128] D. J. Stevenson and E. E. Salpeter, Astrophys. J. Suppl. Ser. **35**, 239 (1977).

[129] D. M. Straus, N. W. Ashcroft, and H. Beck, Phys. Rev. B **15**, 1914 (1977).

[130] J. E. Klepeis, K. J. Schafer, T. W. Barbee, and M. Ross, Science **254**, 986 (1991).

[131] O. Pfaffenzeller, D. Hohl, and P. Ballone, Phys. Rev. Lett. **74**, 2599 (1995).

[132] F. H. Ree, J. Phys. Chem. **87**, 2846 (1983).

[133] D. J. Stevenson, Annu. Rev. Earth Planet. Sci. **10**, 257 (1982).

[134] N. Nettelmann, B. Holst, A. Kietzmann, M. French, R. Redmer, and D. Blaschke, Astrophys. J. **683**, 1217 (2008).

[135] N. Nettelmann, *Matter under extreme conditions: modelling giant planets*, Dissertation, Universität Rostock (2009).

[136] T. Guillot, Science **286**, 72 (1999).

[137] J. J. Fortney and N. Nettelmann, Space Sci. Rev. **152**, 423 (2010).

[138] T. Guillot, Planet. Space Sci. **47**, 1183 (1999).

[139] U. von Zahn, D. M. Hunten, and G. Lehmacher, J. Geophys. Res. **103**, 0148 (1998).

[140] J. N. Bahcall, M. H. Pinsonneault, and G. J. Wasserburg, Rev. Mod. Phys. **67**, 781 (1995).

[141] J. J. Fortney and W. B. Hubbard, Icarus **164**, 228 (2003).

[142] J. J. Fortney and W. B. Hubbard, Astrophys. J. **608**, 1039 (2004).

[143] A. P. Boss, Astrophys. J. **599**, 577 (2003).

[144] Y. Alibert, C. Mordasini, W. Benz, and C. Winisdoerffer, A&A **434**, 343 (2005).

[145] W. Lorenzen, B. Holst, and R. Redmer, Phys. Rev. Lett. **102**, 115701 (2009).

[146] W. Lorenzen, B. Holst, and R. Redmer, Phys. Rev. B **84**, 235109 (2011).

[147] R. O. Jones and O. Gunnarsson, Rev. Mod. Phys. **61**, 689 (1989).

[148] E. Engel and R. M. Dreizler, *Density Functional Theory: An Advanced Course* (Springer, 2011).

[149] M. P. Allen and D. J. Tildesley, *Computer Simulation of Liquids* (Oxford Science Publications, 1987).

[150] D. C. Rapaport, *The Art of Molecular Dynamics Simulation* (Cambridge University Press, 1996).

[151] D. Frenkel and B. Smit, *Understanding Molecular Simulation: from algorithms to applications* (Academic Press, 2002).

[152] C. J. Horowitz and K. Kadau, Phys. Rev. Lett. **102**, 191102 (2009).

[153] J. E. Jones, Proc. R. Soc. Lond. A **106**, 463 (1924).

[154] S. A. Adelman and J. D. Doll, J. Chem. Phys. **64**, 2375 (1976).

[155] H. C. Andersen, J. Chem. Phys. **72**, 2384 (1980).

[156] H. J. C. Berendsen, J. P. M. Postma, W. F. van Gunsteren, A. DiNola, and J. R. Haak, J. Chem. Phys. **81**, 3684 (1984).

[157] S. Nosé, J. Chem. Phys. **81**, 511 (1984).

[158] W. G. Hoover, Phys. Rev. A **31**, 1695 (1985).

[159] G. Bussi, D. Donadio, and M. Parrinello, J. Chem. Phys. **126**, 014101 (2007).

[160] P. Hohenberg and W. Kohn, Phys. Rev. **136**, B864 (1964).

[161] W. Kohn and L. J. Sham, Phys. Rev. **140**, A1133 (1965).

[162] P. Haas, F. Tran, and P. Blaha, Phys. Rev. B **79**, 085104 (2009).

[163] J. P. Perdew and A. Zunger, Phys. Rev. B **23**, 5048 (1981).

[164] J. P. Perdew and Y. Wang, Phys. Rev. B **45**, 13244 (1992).

[165] J. P. Perdew, K. Burke, and M. Ernzerhof, Phys. Rev. Lett. **77**, 3865 (1996).

[166] J. Heyd, G. E. Scuseria, and M. Ernzerhof, J. Chem. Phys. **118**, 8207 (2003).

[167] J. Heyd, G. E. Scuseria, and M. Ernzerhof, J. Chem. Phys. **124**, 219906 (2006).

[168] M. E. Casida, "sites.google.com/site/markcasida/dft," (2012).

[169] S. Kurth, J. P. Perdew, and P. Blaha, Int. J. Quantum Chem. **75**, 889 (1999).

[170] J. Heyd and G. E. Scuseria, J. Chem. Phys. **121**, 1187 (2004).

[171] K. Hummer, J. Harl, and G. Kresse, Phys. Rev. B **80**, 115205 (2009).

[172] P. Haas, F. Tran, P. Blaha, L. S. Pedroza, A. J. R. da Silva, M. M. Odashima, and K. Capelle, Phys. Rev. B **81**, 125136 (2010).

[173] P. Söderlind and A. Gonis, Phys. Rev. B **82**, 033102 (2010).

[174] D. R. Hamann, Phys. Rev. B **55**, R10157 (1997).

[175] V. N. Staroverov, G. E. Scuseria, J. Tao, and J. P. Perdew, J. Chem. Phys. **119**, 12129 (2003).

[176] J. Heyd and G. E. Scuseria, J. Chem. Phys. **120**, 7274 (2004).

[177] S. V. Faleev, M. van Schilfgaarde, T. Kotani, F. m. c. Léonard, and M. P. Desjarlais, Phys. Rev. B **74**, 033101 (2006).

[178] Y. Zhao and D. G. Truhlar, J. Chem. Phys. **130**, 074103 (2009).

[179] D. R. Hamann, M. Schlüter, and C. Chiang, Phys. Rev. Lett. **43**, 1494 (1979).

[180] G. B. Bachelet, D. R. Hamann, and M. Schlüter, Phys. Rev. B **26**, 4199 (1982).

[181] D. Vanderbilt, Phys. Rev. B **41**, 7892 (1990).

[182] G. Kresse and D. Joubert, Phys. Rev. B **59**, 1758 (1999).

[183] P. E. Blöchl, Phys. Rev. B **50**, 17953 (1994).

[184] A. Baldereschi, Phys. Rev. B **7**, 5212 (1973).

[185] H. J. Monkhorst and J. D. Pack, Phys. Rev. B **13**, 5188 (1976).

[186] R. P. Feynman, Phys. Rev. **56**, 340 (1939).

[187] G. Kresse and J. Hafner, Phys. Rev. B **47**, 558 (1993).

[188] G. Kresse and J. Hafner, Phys. Rev. B **49**, 14251 (1994).

[189] G. Kresse and J. Furthmüller, Phys. Rev. B **54**, 11169 (1996).

[190] J. Hafner, J. Comput. Chem. **29**, 2044 (2008).

[191] R. Kubo, J. Phys. Soc. Jap. **12**, 570 (1957).

[192] R. Kubo, M. Yokota, and S. Nakajima, J. Phys. Soc. Jap. **12**, 1203 (1957).

[193] D. A. Greenwood, Proc. Phys. Soc. **71**, 585 (1958).

[194] M. P. Desjarlais, J. D. Kress, and L. A. Collins, Phys. Rev. E **66**, 025401(R) (2002).

[195] S. Mazevet, M. Torrent, V. Recoules, and F. Jollet, High Energy Density Phys. **6**, 84 (2010).

[196] B. Holst, M. French, and R. Redmer, Phys. Rev. B **83**, 235120 (2011).

[197] M. Pozzo, M. P. Desjarlais, and D. Alfè, Phys. Rev. B **84**, 054203 (2011).

[198] S. Mazevet, M. P. Desjarlais, L. A. Collins, J. D. Kress, and N. H. Magee, Phys. Rev. E **71**, 016409 (2005).

[199] M. French, T. R. Mattsson, and R. Redmer, Phys. Rev. B **82**, 174108 (2010).

[200] M. French, S. Hamel, and R. Redmer, Phys. Rev. Lett. **107**, 185901 (2011).

[201] M. French, A. Becker, W. Lorenzen, N. Nettelmann, M. Bethkenhagen, J. Wicht, and R. Redmer, Astrophys. J. Suppl. Ser. **202**, 5 (2012).

[202] M. A. Morales, E. Schwegler, D. Ceperley, C. Pierleoni, S. Hamel, and K. Caspersen, Proc. Natl. Acad. Sci. USA **106**, 1324 (2009).

[203] E. Marceca, G. Schäfer, and F. Hensel, J. Chem. Thermodyn. **28**, 647 (1996).

[204] D. M. Wood and A. Zunger, J. Phys. A **18**, 1343 (1985).

[205] A. Becker, Private communication.

[206] N. Nettelmann, A. Becker, B. Holst, and R. Redmer, Astrophys. J. **750**, 52 (2012).

[207] R. Püstow, N. Nettelmann, W. Lorenzen, and R. Redmer, Icarus (2012), in preparation.

[208] M. Bethkenhagen, *Ab-initio Berechnungen von Ammoniak unter hohem Druck*, Diplomarbeit, University of Rostock (2011).

[209] M. D. Knudson and M. P. Desjarlais, Phys. Rev. Lett. **103**, 225501 (2009).

[210] P. Loubeyre, Phys. Rev. Lett. **58**, 1857 (1987).

[211] A. Einstein, Ann. Phys. (Leipzig) **322**, 549 (1905).

[212] R. Kubo, Rep. Prog. Phys. **29**, 255 (1966).

[213] S. G. Brush, H. L. Sahlin, and E. Teller, J. Chem. Phys. **45**, 2102 (1966).

[214] P. Peebles, Astrophys. J. **140**, 328 (1964).

[215] W. Lorenzen, *Wasserstoff-Helium-Mischungen unter hohem Druck: Zustandsgleichung und Mischungslücke*, Diplomarbeit, University of Rostock (2008).

[216] R. Püstow, *Die innere Struktur und Evolution von Saturn*, Diplomarbeit, University of Rostock (2010).

[217] S. Stanley and G. Glatzmaier, Space Sci. Rev. **152**, 617 (2010).

[218] J. Wicht and A. Tilgner, Space Sci. Rev. **152**, 501 (2010).

[219] S. Stanley and J. Bloxham, Nature **428**, 151 (2004).

[220] S. Stanley and J. Bloxham, Icarus **184**, 556 (2006).

[221] R. Redmer, T. R. Mattsson, N. Nettelmann, and M. French, Icarus **211**, 798 (2011).

[222] U. R. Christensen and J. Wicht, Icarus **196**, 16 (2008).

[223] I. Iosilevskiy, V. Gryaznov, E. Yakub, C. Ronchi, and V. Fotov, Contrib. Plasma Phys. **43**, 316 (2003).

[224] F. Hensel and W. W. Warren Jr., *Fluid Metals: The Liquid-Vapor Transition of Metals* (Princeton University Press, 1999).

[225] S. Hamel, M. A. Morales, and E. Schwegler, Phys. Rev. B **84**, 165110 (2011).

[226] K. Wünsch, J. Vorberger, G. Gregori, and D. O. Gericke, Europhys. Lett. **94**, 25001 (2011).

[227] R. D. Johnson III, ed., *NIST Standard Reference Database Number 101* (NIST Computational Chemistry Comparison and Benchmark Database, Release 15b, August 2011).